Title

The Legacy of the AKARI Infrared Space Telescope: Polycyclic Aromatic Hydrocarbon Dust Emission as a Star Formation Rate Indicator

Author

Kim, Helen Kyung

Publication Date

2023

Peer reviewed|Thesis/dissertation

UNIVERSITY OF CALIFORNIA

Los Angeles

The Legacy of the *AKARI* Infrared Space Telescope: Polycyclic Aromatic Hydrocarbon Dust Emission as a Star Formation Rate Indicator

A dissertation submitted in partial satisfaction
of the requirements for the degree
Doctor of Philosophy in Astronomy and Astrophysics

by

Helen Kyung Kim

2023

ABSTRACT OF THE DISSERTATION

The Legacy of the *AKARI* Infrared Space Telescope:
Polycyclic Aromatic Hydrocarbon Dust Emission
as a Star Formation Rate Indicator

by

Helen Kyung Kim
Doctor of Philosophy in Astronomy and Astrophysics
University of California, Los Angeles, 2023
Professor Matthew A. Malkan, Chair

Polycyclic aromatic hydrocarbon (PAH) dust emission has been proposed as an effective extinction-independent star formation rate (SFR) indicator in the mid-infrared (MIR), but is sensitive to conditions in the interstellar medium. This thesis is based on MIR photometric data from the *AKARI*/Infrared Camera (IRC), which provides a representative and unbiased sample for studying the effects of metallicity, starburst intensity, and active galactic nuclei (AGN) on PAH dust emission. Our observations include follow-up, rest-frame optical spectra of 443 galaxies within the *AKARI* North Ecliptic Pole survey that have IRC detections from 7—24 μm. We use optical emission line diagnostics to measure gas-phase metallicity, to classify the source of ionizing photons, to measure dust extinction, and to infer star formation rate (SFR) based on Hα and [O II]$\lambda\lambda 3726, 3729$ emission line luminosities. We show that the PAH 6.2 μm and PAH 7.7 μm luminosities ($L(PAH\ 6.2\ \mu m)$ and $L(PAH\ 7.7\ \mu m)$, respectively) derived using multi-wavelength model fits are consistent with those derived from slitless spectroscopy within 0.2 dex. We find that $L(PAH\ 6.2\ \mu m)$

and $L(PAH\ 7.7\ \mu m)$ correlate linearly with the 24 μm-dust corrected Hα luminosity only for normal, main-sequence galaxies. Assuming multi-linear fits, we quantify the additional dependencies on gas-phase metallicity and starburst intensity, which we use to correct our PAH SFR calibrations at $0 < z < 1.2$. By integrating 8 and 12 μm luminosity functions, we derive the cosmic star formation rate density (SFRD) per comoving volume in redshift bins at $z \sim 0.15$, 0.25, 0.38, 0.5, 0.78, and 1. The PAH SFRD is consistent with that of the far-infrared and reaches an order of magnitude higher than that of UV observations at $z \sim 1$. In addition, starburst galaxies contribute a significant fraction of the total SFRD at $z \sim 1$ compared to main-sequence galaxies. We discuss the radio properties of our mid-infrared-selected galaxies for sources with *GMRT* observations and compare the radio SFR to the PAH SFR. Finally, in dust-obscured AGN, we demonstrate photometric detection of 9.7 μm silicate absorption at $z \sim 0.2$ and $z \sim 0.45$ with stacking of *AKARI*/IRC spectral energy distributions.

The dissertation of Helen Kyung Kim is approved.

Edward L. Wright

Jean L. Turner

Alice E. Shapley

Matthew A. Malkan, Committee Chair

University of California, Los Angeles

2023

Dedicated with love to my mother and father, and to Luke

TABLE OF CONTENTS

LIST OF FIGURES

LIST OF TABLES

ACKNOWLEDGMENTS

I would like to express my gratitude for all of the support that I have received over the years. First, I would like to thank my advisor, Matt Malkan, for his patience, flexibility, and inspiring enthusiasm while guiding my research. I would also like to thank my committee members, Alice Shapley, Jean Turner, and Ned Wright, for their helpful comments and insight. It has been a huge privilege and honor to learn from you all.

I could not have completed this work without the support of my family. I am grateful to my parents, Yong and Jung Kim, for their love and sacrifice that has enabled me to achieve my lifelong dream of studying what lies beyond this "pale blue dot"; to Sonia Streng, for being the best big sister I could ask for; to Paul Streng, for all the encouragement; to Kira Twombly, Christine Wiitala, and Phyllis Wiitala, for their wonderful company and for welcoming me into their family with open arms.

I would like to thank my friends, with a special thanks to Gurleen Bal, Ivy Chen, Bao-Minh Hoang, Kelly Huang, Harsha Lokavarapu, Emily Martin, Pasha Reshetikhin, Cole Stephens, Lorae Tamura, and Marcus Tamura for all the fun times and for helping me take much-needed breaks. I give a special, posthumous thank you to my high school English teacher and mentor, Michael Glaser, whose compassion and gentle wit live on in my memory.

I extend a heartfelt thank you to my partner, Luke Twombly, who has been by my side for the past eight years and has been my source of joy, never failing to make me laugh no matter how difficult life got (including through a pandemic).

Some of the data presented herein were obtained at the W. M. Keck Observatory, which is operated as a scientific partnership among the California Institute of Technology, the University of California and the National Aeronautics and Space Administration. The Observatory was made possible by the generous financial support of the W. M. Keck Foundation.

This research has made use of the Keck Observatory Archive (KOA), which is operated by the W. M. Keck Observatory and the NASA Exoplanet Science Institute (NExScI), under

contract with the National Aeronautics and Space Administration.

I wish to recognize and acknowledge the very significant cultural role and reverence that the summit of Maunakea has always had within the indigenous Hawaiian community. We are most fortunate to have the opportunity to conduct observations from this mountain.

VITA

2014 B.A. (Physics) and B.A. (Astrophysics), University of California, Berkeley.

2015 Eugene V. Cota-Robles Fellowship, University of California, Los Angeles.

2017 M.S. (Astronomy), University of California, Los Angeles.

PUBLICATIONS

Kim, H. K., Malkan, M. A., Oi, N., Burgarella, D., Buat, V., Takagi, T., & Matsuhara, H. "DEIMOS Spectroscopy of Star-Forming Galaxies in the *AKARI* North Ecliptic Pole-Deep Field." 2018, in The Cosmic Wheel and the Legacy of the *AKARI* Archive: From Galaxies and Stars to Planets and Life, 371K.

Seo, H., Jeong, W.-S., Kim, M., Kim, S. J., Ko, J., Pyo, J., Kim, M. G., Pearson, C., Barrufet, L., Campos Varillas, M. d. C., Matsuhara, H., Malkan, M., **Kim, H. K.**, Takagi, T., Miyaji, T., Diaz Tello, J., Goto, T., & Oi, N. "Properties of the SCUBA-2 850 μm Sources in the *AKARI* NEP-Deep Field." 2018, JKAS, 51, 49

Hicks, E. K., Mueller Sanchez, F., Malkan, M., & **Kim, H.** "The KONA Survey: What Drives Black Hole Growth in Local Seyfert Galaxies?" 2019, in American Astronomical Society Meeting Abstracts, Vol. 233, American Astronomical Society Meeting Abstracts #233, 434.01

Goto, T., Oi, N., Utsumi, Y., Momose, R., Matsuhara, H., Hashimoto, T., Toba, Y., Ohyama, Y., Takagi, T., Chiang, C.-Y., Kim, S. J., Kilerci Eser, E., Malkan, M., **Kim, H.**, Miyaji, T., Im, M., Nakagawa, T., Jeong, W.-S., Pearson, C., Barrufet, L., Sedgwick, C., Burgarella, D., Buat, V., & Ikeda, H. "Infrared luminosity functions based on 18 mid-infrared bands: revealing cosmic star formation history with *AKARI* and Hyper Suprime-Cam." 2019, PASJ, 71, 30

Kim, H. K., Malkan, M., Oi, N., Takagi, T., Burgarella, D., Buat, V., Salim, S., Pearson, C., & Matsuhara, H. "DEIMOS and MOSFIRE spectroscopy of star-forming galaxies in the *AKARI* NEP-Deep field." 2020, IAUS, 341, 279K.

Toba, Y., Goto, T., Oi, N., Wang, T.-W., Kim, S. J., Ho, S. C. C., Burgarella, D., Hashimoto, T., Hsieh, B.-C., Huang, T.-C., Hwang, H. S., Ikeda, H., **Kim, H. K.**, Kim, S., Lee, D., Malkan, M. A., Matsuhara, H., Miyaji, T., Momose, R., Ohyama, Y., Oyabu, S., Pearson, C., Santos, D. J. D., Shim, H., Takagi, T., Ueda, Y., Utsumi, Y., & Wada, T. "Search for Optically Dark Infrared Galaxies without Counterparts of Subaru Hyper Suprime-Cam in the *AKARI* North Ecliptic Pole Wide Survey Field." 2020, ApJ, 899, 35

Kim, S. J., Oi, N., Goto, T., Ikeda, H., Ho, S. C. C., Shim, H., Toba, Y., Hwang, H. S., Hashimoto, T., Barrufet, L., Malkan, M., **Kim, H. K.**, Huang, T.-C., Matsuhara, H., Miyaji, T., Pearson, C., Serjeant, S., Santos, D. J. D., Kim, E., Pollo, A., Jeong, W.-S., Wang, T.-W., Momose, R., & Takagi, T. "Identification of *AKARI* infrared sources by the Deep HSC Optical Survey: construction of a new band-merged catalogue in the North Ecliptic Pole Wide field." 2021, MNRAS, 500, 4078

CHAPTER 1

Introduction

The cosmic infrared background suggests at least half the luminous energy generated by stars has been reprocessed into the infrared (IR) by dust (Figure 1.1, Stecker et al., 2016), and that dust-obscured star formation was more important at higher redshifts than today (Buat et al., 2005). Luminous infrared galaxies (LIRGs: 10^{11} $L_\odot \leq$ L(8-1000 μm) $\leq 10^{12}$ $L_\odot$) and ultra-luminous infrared galaxies (ULIRGs: L(8-1000 μm) $\geq 10^{12}$ $L_\odot$) contribute ~70% of the cosmic infrared luminosity density at $z \sim 1$ (Le Floc'h et al., 2005). However, the individual dusty galaxies producing this IR light are not well understood, partly due to the requirement of deep wide-field mid-infrared (MIR) surveys to find them, and the difficulty of studying their dust spectra.

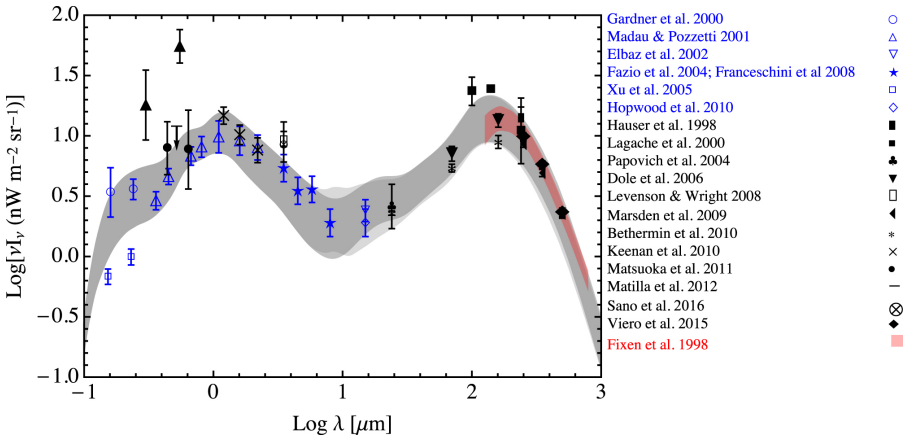

Figure 1.1 From Stecker et al. (2016): Summary of Extragalactic Background Light measurements across the electromagnetic spectrum. Note that the long-wavelength peak from thermal dust grain emission is comparable to the short-wavlength peak from starlight.

The only mission to overcome those limitations was the *AKARI* survey within the North

Ecliptic Pole (NEP) region (Matsuhara et al., 2006), which mapped the NEP Deep and Wide fields (0.5 square degrees and 5.4 square degrees, respectively) from 2006-2011. The rich multi-wavelength coverage of the NEP region makes the *AKARI* infrared telescope uniquely suited to studying the properties of a representative sample which includes dust-obscured galaxies and active galactic nuclei (AGN), across the electromagnetic spectrum. In particular, the NEP-Deep region has been intensively surveyed from the X-ray and ultraviolet (UV) to the submillimeter and radio regime, allowing us to construct complete spectral energy distributions (SEDs). Figure 1.2 from Matsuhara et al. (2017) shows the sky coverage of the NEP-Deep and Wide fields, with highlighted regions indicating coverage from additional telescopes, including: *Chandra*, *GALEX*, *CFHT*/MegaCam, *CFHT*/Wide-field InfraRed Camera (WIRCam), *Subaru*/Suprime-Cam (S-Cam), *Herschel*/Photodetector Array Camera and Spectrometer (PACS), and *Herschel*/Spectral and Photometric Imaging Receiver (SPIRE).

A large portion of the *AKARI* mission was devoted to obtaining deep, nine-filter photometry using the Infrared Camera (IRC), which effectively provides very low-resolution spectra from 2 to 24 μm. Over 6,000 faint galaxy mid-infrared (MIR) "spectra" have been observed in the NEP region – a one-and-a-half order-of-magnitude increase over all other MIR samples (e.g., *Spitzer*/IRS and *ISO*/SWS) combined. The continuous MIR coverage fills in the wavelength gaps from *Spitzer*, as illustrated by the normalized filter transmission curves shown in Figure 1.3. The top panel shows *Spitzer*/Infrared Array Camera (IRAC) channels 1 through 4 (abbreviated as "I1," etc.) with effective wavelengths at 3.6, 4.5, 5.8, and 8 μm, and the 24 μm *Spitzer*/Multi-band Imaging Photometer (MIPS) channel 1 filter (abbreviated as "M1"); the bottom panel shows the *AKARI*/IRC filters.

In star-forming galaxies, the mid-infrared spectrum is dominated by emission features from the stochastic heating of polycyclic aromatic hydrocarbon (PAH) dust grains, mainly via absorption of UV radiation from massive stars (Peeters et al., 2004). Figure 1.4 shows a template of PAH dust emission averaged over local star-forming galaxies observed with

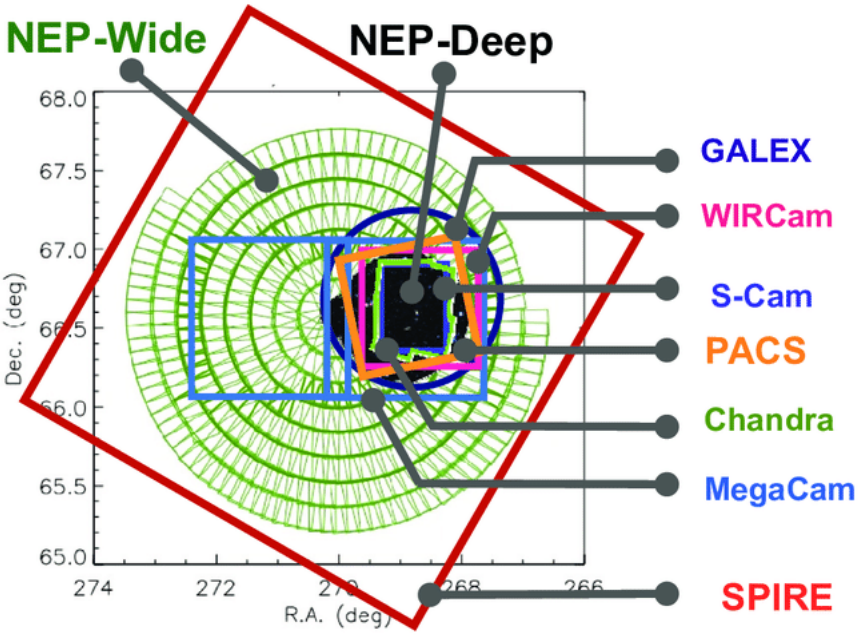

Figure 1.2 From Matsuhara et al. (2017): Multi-wavelength sky coverage of the *AKARI* North Ecliptic Pole (NEP) Deep and Wide-Field surveys. The most complete multiwavelength coverage is centered on the NEP-Deep region just to the west of the NEP. The image of the NEP-Deep field is made from three near-infrared colors with *AKARI*/IRC photometry at 2, 3, and 4 μm (Oi et al., 2014).

Spitzer/IRS spectroscopy (Smith et al., 2007). The emission features centered at 6.2 μm and 7.7 μm are attributed to C-C stretching modes, while those centered at 8.6 and 11.3 μm are attributed to C-H bending modes Bakes et al. (2001). The wavelength coverage of the *AKARI*/IRC is optimally suited for studying the strongest PAH emission feature, the 7.7 μm PAH blend composed of emission features at 7.42, 7.60, and 7.85 μm. The 7.7 μm blend has been proposed as an extinction-independent star formation rate (SFR) indicator (Peeters et al., 2004) and has been empirically calibrated against other SFR tracers, such as the dust-corrected Hα luminosity (e.g., Shipley et al., 2016). However, the PAH luminosity/equivalent width is found to be deficient in metal-poor galaxies, starburst galaxies (i.e., galaxies with high specific star formation rate (sSFR) relative to the star-forming main sequence), and AGN.

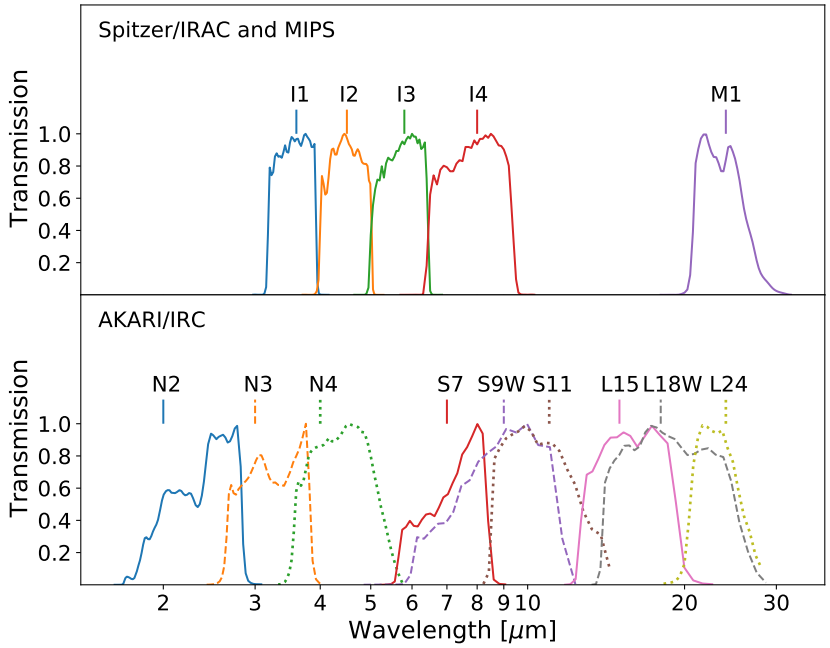

Figure 1.3 Filter transmission curves for *Spitzer*/IRAC and MIPS (top panel) and *AKARI*/IRC (bottom panel).

In addition to showing suppressed PAH luminosity, dust-obscured AGN exhibit strong silicate absorption features at 9.7 and 18 μm that affect the equivalent widths of the surrounding PAH features, particularly at 7.7, 8.6, and 11.3 μm (Spoon et al., 2007; Imanishi et al., 2007; Smith et al., 2007). For example, silicate absorption at 9.7 μm causes dust-obscured AGN to have lower 12.7 μm/11.3 μm and 11.3 μm/6.2 μm equivalent widths, in contrast to star-forming galaxies which have constant ratios (García-Bernete et al., 2022). The spectral classification from Spoon et al. (2007), which categorizes galaxies based on their 9.7 μm silicate strength and PAH 6.2 μm equivalent width, demonstrates the diversity observed in mid-infrared-selected spectra.

This thesis is organized as follows. In Chapter 2, we present the details of the spectroscopic and multi-wavelength photometric data of the *AKARI* NEP survey. We derive SFR calibrations based on correlations between PAH luminosity and dust-corrected Hα and

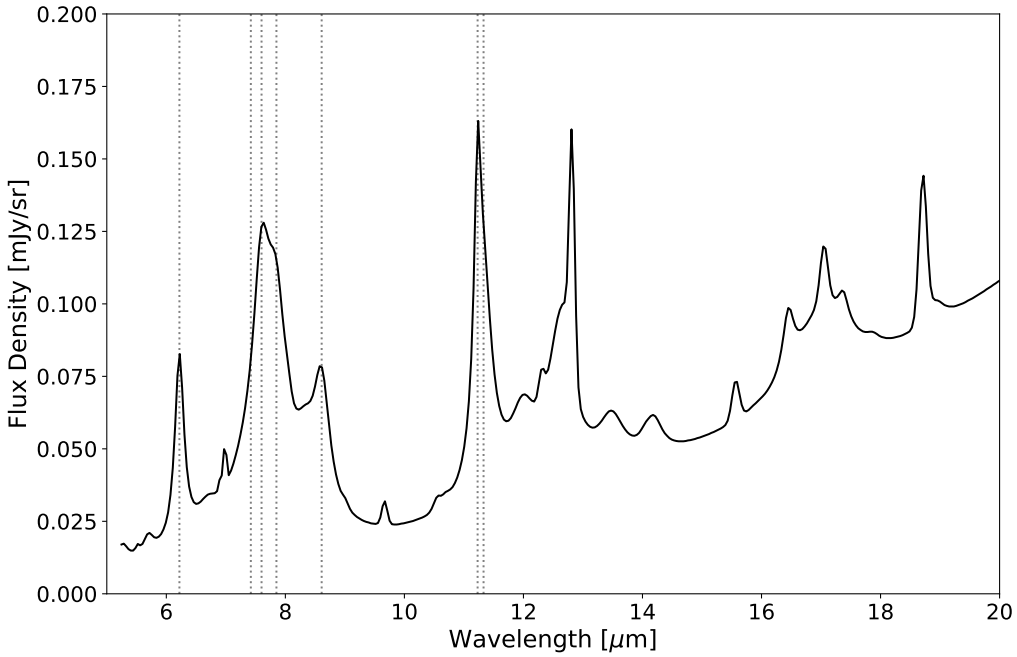

Figure 1.4 Mid-infrared template spectrum of PAH dust emission given by Smith et al. (2007). The template was produced from averaged *Spitzer*/IRS spectra weighted by total infrared luminosity. The vertical dotted lines indicate the PAH emission features at 6.22, 7.42, 7.60, 7.85, 8.61, 11.23, and 11.33 μm.

[O II]$\lambda\lambda 3726, 3729$ luminosities. In Chapter 3, we compare our PAH SFR measurements to the radio SFR by selecting sources with 610 MHz detections from the *Giant Metrewave Radio Telescope* (*GMRT*). In Chapter 4, we discuss how *AKARI*/IRC photometry may be used to detect the presence of 9.7 μm silicate absorption in dust-obscured AGN at $z \sim 0.2$ and $z \sim 0.45$. In Chapter 5, we provide a summary of the main conclusions. Throughout this work, we assume a flat cosmology with Ω_Λ=0.7, Ω_M=0.3, and H_0=70 km/s/Mpc. All magnitudes are given in the AB system.

CHAPTER 2

Calibration of the PAH Star Formation Rate from Mid-Infrared Photometry

2.1 Introduction

The star formation rate (SFR) is one of the key parameters that describes a galaxy's growth and evolution, tracing the conversion of baryonic matter in the interstellar medium (ISM) into stellar radiation. The calibration of various SFR indicators across the electromagnetic spectrum has been extensively studied for the past three decades (Kennicutt & Evans, 2012; Calzetti, 2013). The Balmer recombination lines, most notably Hα λ6563, and the rest-frame UV continuum emission from massive stars have been established as standard indicators at z=0 and $z\gtrsim$1, respectively. However, the SFRs derived from rest-frame optical/UV lines are prone to large uncertainties in the presence of interstellar dust, which absorbs stellar photons and re-radiates in the infrared.

The brightness of the cosmic infrared background suggests at least half the luminous energy generated by stars has been reprocessed into the IR by dust (Lagache & Dole, 2006), and that dust-obscured star formation was more important at higher redshifts than today (Buat et al., 2007). At $z\sim$1, infrared luminous galaxies ($L(8-1000\ \mu m) \geq 10^{11}\ L_{\odot}$) contribute $\sim$70% of the cosmic infrared luminosity density (Le Floc'h et al., 2005), but the individual dusty galaxies producing this IR light are not well understood, partly due to the requirement of deep wide-field mid-IR surveys to find them, and then the extreme difficulty of studying their dust spectra. The only mission to overcome those limitations was the *AKARI*

space telescope with its Infrared Camera (IRC), which devoted a substantial fraction of its entire several-year lifetime to intensively mapping the 0.5 deg^2 area of North Ecliptic Pole (NEP) Deep field (orange scalloped circle in Figure 1 of Takeuchi et al., 2007; Murata et al., 2013). *AKARI*-NEP's>6000 faint galaxy mid-IR 9-point spectra are a 1.5 order-of-magnitude increase over all other samples (e.g. *Spitzer*/IRS) combined. The NEP-Deep field is in a prime location that has been observed very intensively at all other wavelengths from the X-ray and UV to radio wavelengths.

The luminosities of the 3.3, 6.2, 7.7, 8.6, and 11.3 μm PAH emission features have been proposed as extinction-independent SFR indicators (Peeters et al., 2004; Brandl et al., 2006; Houck et al., 2007). The wavelength coverage from the IRC-derived spectral energy distributions (SEDs) is uniquely suited to study the strongest of these: the PAH 7.7 μm blend composed of emission features at 7.42, 7.60, and 7.85 μm, which can contribute $\sim$ 45% of the total PAH luminosity in star-forming galaxies (Shipley et al., 2013). However, studies of ultra-luminous infrared galaxies (ULIRGs: L(8-1000 μm) $\geq 10^{12}$ L$_\odot$) at $z < 0.9$ targeted by *Spitzer*/IRS have diverse mid-infrared spectra, with the majority of ULIRGs having depressed PAH 6.2 and 7.7 μm equivalent widths, which is likely due to UV photons from buried AGN or compact star formation destroying small dust grains (Spoon et al., 2007; Imanishi et al., 2007; Desai et al., 2007). But on the other hand, at $z \sim 1$, ULIRGs have been observed with "enhanced" peak PAH 7.7 μm luminosities per total infrared luminosity relative to local ULIRGs (Takagi et al., 2010).

The strength of PAH emission is also believed to depend on the gas-phase metallicity of the interstellar medium (ISM). Engelbracht et al. (2005) found decreased 8 μm-to-24 μm flux density ratios in local star-forming galaxies with 12+log(O/H) $\lesssim$ 8.2, presumably due to decreased PAH contribution to the 8 μm bandpass. Draine et al. (2007) determined that the PAH index, defined as the fraction of the total dust mass in PAH grains with fewer than 10^3 carbon atoms (q_{PAH}), is lower for galaxies with 12+log(O/H) $\leq$ 8.1 within the Spitzer Nearby Galaxy Survey (SINGS). Some physical interpretations for reduced PAH strength

include: UV dissociation of PAH molecules due to less dust shielding, increased destruction within shock-heated gas, and decreased efficiency in PAH production from carbon stars and planetary nebulae (Draine et al., 2007).

In this chapter, we present SFR calibrations based on PAH luminosity, corrected for metallicity and starburst intensity. In Section 2.2, we describe our spectroscopic and photometric observations, data reduction processes, emission line measurements, galaxy classification, and SED fitting procedure. In section 2.3, we present our methodology for measuring PAH luminosities. We confirm their validity by direct comparison with mid-infrared spectra of the same galaxies. In section 2.4, we discuss the effects of starburst intensity, metallicity, and AGN strength on PAH luminosity; we derive SFR prediction equations as a function of PAH luminosity calibrated against dust-corrected Hα and [O II]$\lambda\lambda 3726, 3729$ line luminosities. In Section 2.5, we apply our SFR equations to estimate the cosmic star formation rate density (SFRD) from $0 \lesssim z \lesssim 1.2$ and compare our results to UV and FIR-based calibrations. In Section 2.6 we discuss our PAH SFR results in the context of other studies, and how our calibrations may be used to analyze future *JWST* observations. In an Appendix we compare our PAH luminosities with the total infrared luminosity, another proposed measure of the total star formation rate.

2.2 Supporting Follow-up Observations from Ground-based Telescopes

2.2.1 Keck II/DEIMOS spectroscopic sample

From 2014-2016, we observed six slitmasks with Keck II/DEep Imaging Multi-Object Spectrograph (DEIMOS; Faber et al., 2003) targeting the *AKARI* NEP-Deep field. When selecting targets for each slit, we prioritized mid-infrared *AKARI*/IRC sources with detected flux measurements at 9 and 18 μm, and assigned secondary priorities to high-redshift galaxies

(photometric redshift $z_{phot} \sim 1$; Oi et al., 2014) and optical counterparts of *Chandra* X-ray sources (Krumpe et al., 2015). The spectrograph was configured with the 600ZD grating and GG495 order blocking filter (central wavelength $\lambda_c = 7500$ Å) for the two slitmasks observed on August 24, 2014, and the 900ZD grating and GG455 order blocking filter ($\lambda_c = 6800$ Å) for the remaining four slitmasks observed in 2015-2016. A typical slitmask contained ~ 80 slits that were $1''$ in width. The spectral range covered approximately 4850 Å $\lesssim \lambda \lesssim$ 10050 Å, depending on the location of the slit. The spectral resolution was $R \sim 2000$, which corresponds to full-width at half-maximum (FWHM) $\Delta\lambda \sim 3.75$ Å at the central wavelength $\lambda_c = 7500$ Å, as confirmed by the observed widths of night-sky lines. Prior to observing each night, we acquired one set of Ne, Ar, Kr, and Xe arc lamp spectra and three flat field exposures of the detectors illuminated by an internal incandescent lamp. In addition, we observed standard star Feige 15 (RA $01^h49^m09.5^s$, Dec $+13°33'11.4''$) in long-slit mode for flux calibration. We reduced the raw data from 2014-2016 using the UCB DEEP2 spec2d reduction pipeline (Cooper et al., 2012), which processed the flatfields and calibration arcs, fit a polynomial wavelength solution to the pixel locations of arc lines, subtracted night-sky emission, and extracted one- and two-dimensional spectra. The extended flux along the slit was included, but most spectra were unresolved in the spatial direction.

The *AKARI* NEP collaboration observed eight DEIMOS slitmasks in July 2011, with the focus of targeting galaxy cluster candidates with *AKARI*/IRC MIR detections in the NEP-Deep field (PI: Tomotsugu Goto; Shogaki et al., 2018). 553 targets were selected based on *Subaru*/Suprime-Cam (Imai et al., 2007; Wada et al., 2008) R-band and Z-band brightness cuts such that $Z < 23$ mag and $R > 21.5$ mag. Slitmasks contained $\sim 50 - 80$ slits of $1''$ width. The instrument configuration consisted of the 600ZD grating and GG455 order blocking filter, yielding a spectral resolution of $R \sim 2000$. A set of calibration images consisting of a Ne, Ar, Kr, Xe arc lamp image and five flat field lamp images was acquired for each slitmask. Bright spectrophotometric standard stars BD+33°2642 and Feige 110 were observed for 90 seconds each in long-slit mode. Weather conditions were clear on both

nights, with 0.6″ seeing. The data were reduced using the spec2d pipeline described above (Shogaki et al., 2018).

We then flux-calibrated the one-dimensional object spectra from 2011-2016 using standard IRAF routines as follows. The raw frames were overscan-trimmed and bias-subtracted using the mscred.ccdproc routine. A normalized flat field was created using mscred.flatcombine, noao.twodspec.longslit.response, and mscred.mscjoin, and the standard star spectra were flat-fielded with mscred.ccdproc. A wavelength-calibrated standard star image was produced using noao.twodspec.longslit.identify, reidentify, fitcoords, and transform on the arc images to determine the wavelength solution and noao.imred.kpnoslit.doslit on the standard star. Then, the sensitivity function was derived using noao.twodspec.longslit.standard, sensfunc, and calibrate on the standard star. Lastly, the sensitivity function was input into the routine noao.onedspec.calibrate to apply extinction corrections and flux calibrations to the reduced one-dimensional object spectra.

To estimate the photometric accuracy of the flux-calibrated spectra, we calculated the average flux density of the spectra within the *CFHT*/MegaCam r-band filter (5690-6930 Å):

$$f_\nu\ [erg/s/cm^2/Hz] = \frac{1}{c}\frac{\int FT\lambda\, d\lambda}{\int T\lambda\, d\lambda}, \tag{2.1}$$

where F is the galaxy spectrum in erg/s/cm^2/Å, T is the filter response function, λ is the wavelength in Å, and c is the speed of light in Å/s. We compared our measurements to observed photometric *CFHT* r-band flux densities and applied a typical offset correction $\sim 0.1 - 0.25$ dex to account for slit losses.

The sample contains 68 Hα and 259 [O II] emission line candidates with at least four MIR detections/upper limits in the 7-24 μm filters. The ranges in redshift, stellar mass, and TIR luminosity of the combined unique 296 sources are $0.05 < z < 1.36$, 2.1×10^8 $M_\odot < M_* < 9.3 \times 10^{11}$ $M_\odot$, and 1.1×10^9 $L_\odot < L(TIR) < 2.2 \times 10^{12}$ $L_\odot$. Table 1 summarizes the newly reduced and calibrated multi-slit spectroscopy from this work.

Table 1. Summary of observations using the Keck I and Keck II telescopes

Instrument	UT Date	RA (J200) (hh:mm:ss)	Dec (J200) (dd:mm:ss)	PA (deg)	FWHM ($''$)	t_{exp} (min)	N_t
DEIMOS	2008-08-01	17:57:21.3	+66:28:45.7	0.00	0.5	51.0	81
DEIMOS	2008-08-01	17:56:24.6	+66:32:26.1	-10.00	0.6	51.0	80
DEIMOS	2008-08-01	17:55:08.4	+66:42:34.5	-20.00	0.8	51.0	81
DEIMOS	2008-08-01	17:56:26.7	+66:45:40.0	-30.00	0.9	60.0	82
DEIMOS	2008-08-01	17:54:34.3	+66:29:37.4	-35.00	0.7	80.0	79
DEIMOS	2011-07-03	17:53:51.9	+66:44:55.6	359.82	0.6	120.0	66
DEIMOS	2011-07-03	17:55:49.7	+66:45:30.1	359.82	0.6	120.0	61
DEIMOS	2011-07-03	17:56:28.2	+66:41:00.1	359.83	0.6	120.0	55
DEIMOS	2011-07-04	17:57:01.8	+66:30:00.1	359.82	0.6	90.0	65
DEIMOS	2011-07-04	17:56:12.8	+66:30:05.8	359.80	0.6	90.0	64
DEIMOS	2011-07-04	17:54:54.9	+66:29:39.9	359.80	0.6	90.0	65
DEIMOS	2011-07-04	17:53:44.2	+66:27:54.6	359.82	0.6	90.0	83
DEIMOS	2011-07-04	17:57:08.4	+66:43:24.0	37.85	0.6	105.0	66
DEIMOS	2014-08-24	17:55:15.7	+66:38:36.3	130.07	0.6	120.0	83
DEIMOS	2014-08-24	17:54:37.8	+66:29:14.9	160.17	0.6	120.0	83
DEIMOS	2015-09-14	17:52:59.5	+66:30:37.7	145.04	0.8	120.0	78
DEIMOS	2015-09-15	17:55:01.9	+66:43:32.3	156.56	0.9	120.0	88
DEIMOS	2016-09-09	17:55:39.0	+66:29:59.1	150.03	0.9	80.0	77
DEIMOS	2016-09-10	17:53:26.0	+66:41:40.9	94.02	0.9	80.0	78
MOSFIRE	2017-08-02	17:55:46.3	+66:37:26.1	300.03	1.2	61.6	22
MOSFIRE	2017-08-02	17:55:35.4	+66:37:20.6	20.00	0.4	87.5	26
MOSFIRE	2017-08-03	17:53:43.9	+66:27:12.0	340.22	0.5	69.6	23
MOSFIRE	2017-08-03	17:52:39.6	+66:34:16.1	15.00	0.5	63.6	25
MOSFIRE	2017-08-03	17:55:40.8	+66:36:59.8	335.00	0.5	45.7	23

Note. — The exposure time only includes reduced frames. N_t is the number of targeted science objects (excluding alignment stars).

2.2.2 Keck I/MOSFIRE sample

In 2017, we targeted higher redshift galaxies in the *AKARI* NEP-Deep field, with the Multi-Object Spectrometer For Infra-Red Exploration (MOSFIRE; McLean et al., 2012) on the Keck I telescope. Based on photometric redshifts provided by the *AKARI*-NEP team (Oi et al., 2014), we observed four slitmasks in the J-band (1.153–1.352 μm) and one slitmask in the Y-band (0.972–1.125 μm) to target Hα/[NII] in *AKARI*/IRC sources at $0.7 < z < 1.1$ and $0.5 < z < 0.8$, respectively. Each mask had $\sim$ 25 slits with slit width of $0.7''$, and resolution of $R \sim 3300$. Weather conditions were clear and dry on August 2nd and mostly clear with some high clouds on August 3rd. Calibration images consisted of Ne, Ar arc lamps (1.5 sec each) and internal flat fields (11 sec each). Slitmasks were observed in Multiple Correlated Double Sampling (MCDS) mode with 16 reads, and a dither position offset of $\pm 1.5''$ was used. Standard stars FS 139 (RA $16^h33^m52.9^s$, Dec $+54°28'23''$) and HD 162208 were observed in long-slit mode.

We used the standard MOSFIRE Data Reduction Pipeline (DRP) to reduce the spectroscopic data. The pipeline creates a pixel flatfield, performs slit edge tracing, calibrates the wavelength scale, performs background subtraction, rectifies the slits, and extracts the 1D spectra. We flux-calibrated the 1D spectra by using the standard star. First we smoothed the standard star spectrum and interpolated over telluric absorption lines. Then we modeled the star as a blackbody based on its effective temperature, and normalized the curve to the star's Ks-band magnitude from the Two Micron All Sky Survey (2MASS), factoring in the filter response function. The factor to convert from counts/second to erg/s/cm^2/Å is then proportional to the ratio of the normalized blackbody function to the calibration star spectrum. We accounted for slit losses by comparing each galaxy's average flux density to *CFHT*/WIRCAM J-band photometry.

Our MOSFIRE sample contains 14 Hα and 9 [O II] emission-line candidates with at least four MIR detections/upper limits in the 7–24 μm filters. The ranges in redshift, stellar

mass, and TIR luminosity of the combined unique 15 sources are $0.54 < z < 1.04$, 8.5×10^9 $M_\odot < M_* < 1.1 \times 10^{11}$ $M_\odot$, and 5.5×10^{10} $L_\odot < L(TIR) < 8.6 \times 10^{11}$ $L_\odot$.

2.2.3 Takagi et al. (2010) sample

In addition to our 2011-2016 Keck II/DEIMOS observations, we obtained reduced DEIMOS spectra and emission line flux measurements from observations in semester 2008A through the *AKARI*-NEP collaboration (PI: Toshinobu Takagi). Targets included 242 *AKARI*-NEP mid-IR-selected sources with *Subaru*/Suprime-Cam R-band magnitude $\lesssim$ 24 mag. Five slitmasks were observed using the 600ZD grating and GG495 order blocking filter. Standard stars HZ 44 and Feige 110 were observed with a long slit (1.5″ slit width) using the same grating and filter setup as the targets. Data were reduced using the spec2d pipeline, and then flux-calibrated with standard IRAF routines. [O II]$\lambda\lambda 3726, 3729$, H$\beta$, [O III]$\lambda 5007$, H$\alpha$, and [N II]$\lambda 6584$ emission lines were fit using Gaussian models with the IDL/MPFIT routine. Double Gaussians were used to fit the resolved [O II] doublet, Hβ emission with underlying absorption, and Hα with broad and narrow line components in AGN. The continuum was modeled with a linear fit. Hα and [N II]$\lambda\lambda 6548, 6584$ were fit simultaneously with three Gaussians. We will publish a full table of coordinates, spectroscopic redshifts, and emission line fluxes in Kim et al., in prep. The Takagi et al. sample contains 48 Hα and 126 [O II] emission line candidates with at least four MIR detections in the 7–24 μm filters. The ranges in redshift, stellar mass, and TIR luminosity of the combined unique 152 sources are $0.09 < z < 1.35$, 9.5×10^8 $M_\odot < M_* < 3.1 \times 10^{11}$ $M_\odot$, and 8.3×10^8 $L_\odot < L(TIR) < 3.1 \times 10^{12}$ $L_\odot$.

2.2.4 Shim et al. (2013) sample

We also include spectroscopic redshifts and emission line fluxes from the Shim et al. (2013) sample, which consists of spectroscopy of hundreds of low-redshift galaxies and AGN ($z \lesssim$

0.4) in the *AKARI* NEP-Wide field. This provides rest-frame UV/optical emission line detections from *MMT*/Hectospec and *WIYN*/HYDRA multi-object spectrographs. The authors primarily selected targets with MIR detections at 11 μm and 15 μm. Secondary target selection criteria are summarized in their Table 1, and include AGN candidates, *Herschel* FIR sources, and PAH-luminous galaxies. The Shim et al. sample contains 498 Hα and 571 [O II] emission line galaxieses with at least four MIR detections/upper limits in the 7–24 μm filters and secure redshifts (i.e., quality flag of 4). The ranges in redshift, stellar mass, and TIR luminosity of the combined unique 711 sources are $0.03 < z < 1.29$, 1.9×10^8 $M_\odot < M_* < 9.9 \times 10^{11}$ $M_\odot$, and 4.3×10^8 $L_\odot < L(TIR) < 3.2 \times 10^{12}$ $L_\odot$.

2.2.5 Oi et al. (2017) sample

We supplement our high-redshift MOSFIRE data with near-infrared Hα detections from Oi et al. (2017), who studied the mass-metallicity relation in luminous infrared galaxies at $z \sim 0.9$. Their sample consists of *Subaru*/FMOS Hα/[N II] multi-object spectroscopy in the J-long band (1.11–1.35 μm), of *AKARI* mid-infrared sources in the NEP-Deep field. Target galaxies were selected to have detections at 11 μm, 15 μm, and/or 18 μm, and estimated photometric redshifts $z_{phot} \sim 1$. Hα/[N II] fluxes are given for 28 secure Hα emitters and Hα fluxes are given for 36 "non-secure" Hα detections (i.e., objects where a single emission line was observed and assumed to be Hα.) Some of the non-secure Hα objects have since been re-observed in optical wavelengths by *AKARI* NEP collaborators using *MMT*/Hectospec, *WIYN*/Hydra, *Keck II*/DEIMOS, and *GTC*/OSIRIS, allowing us to confirm that 10/36 are indeed Hα detections based on the detection of other strong emission lines at shorter wavelengths (e.g., [OII], Hγ, Hβ, [OIII]). In addition, we find that the emission line from object 61016583, assumed by the Oi et al. to be Hα, is [O III]λ5007 at $z = 1.357$. For reference, we list the updated secure Hα objects in Table 5 in the Appendix. Our SFR calibration sample includes 37 FMOS objects with Hα detections and at least four MIR detections/upper limits in the 7–24 μm filters. The ranges in redshift, stellar mass, and

TIR luminosity are $0.70 < z < 1.03$, $2.1 \times 10^9\ M_\odot < M_* < 1.5 \times 10^{11}\ M_\odot$, and $8.1 \times 10^{10}\ L_\odot < L(TIR) < 1.5 \times 10^{12}\ L_\odot$.

2.2.6 Validation sample: Ohyama et al. (2018) SPICY galaxies

The *AKARI*/IRC slitless SpectroscoPIC surveY (SPICY) obtained infrared spectra of all sources with 9 μm flux density brighter than 0.3 mJy in 14 NEP regions of $10' \times 10'$. The primary goal was to study PAH emission in galaxies at $z \lesssim 0.5$ (Ohyama et al., 2018) within the NEP-Deep and Wide fields. Low-resolution spectra ($R \sim 50$) were acquired with the short-wavelength MIR camera on the IRC, which covers a wavelength range of $5 - 13$ μm. Ohyama et al. identified 48 galaxies with detectable PAH 6.2, 7.7, and 8.6 μm features. All 48 galaxies have *AKARI*/IRC photometry, with 83% having detections in the N2, N3, N4, S7, S9W, S11, L15, and L18W filters ($\sim 2 - 18$ μm). Of the 48 PAH galaxies in the sample, 41 galaxies have optical spectroscopic detections and 33 galaxies have detected Hα emission from *Keck II*/DEIMOS (this work) or *MMT*/Hectospec (PI: Ho Seong Hwang). Figure 2.1 illustrates typical SPICY spectra of star-forming galaxies from Ohyama et al. (2018). We use these 41 galaxies as our validation sample, to test the consistency and accuracy of our photometrically-derived PAH luminosity measurements. The ranges in redshift, stellar mass, and TIR luminosity of the 41 sources are $0.06 < z < 0.49$, $2 \times 10^9\ M_\odot < M_* < 2 \times 10^{11}\ M_\odot$, and $2.1 \times 10^9\ L_\odot < L(TIR) < 3.9 \times 10^{11}\ L_\odot$.

2.2.7 Emission line measurements

Figure 2.2 shows examples of the quality of our DEIMOS and MOSFIRE spectra. The top panel shows a MOSFIRE galaxy detected in the J-band that has red- and blue-shifted lines in Hα and [N II] due to rotational kinematics. The second panel is an example of a typical star-forming galaxy observed with DEIMOS with Hα, [N II], and [S II] emission lines. The third panel shows a Seyfert galaxy with double-peaked emission in Hβ and [O III]. The

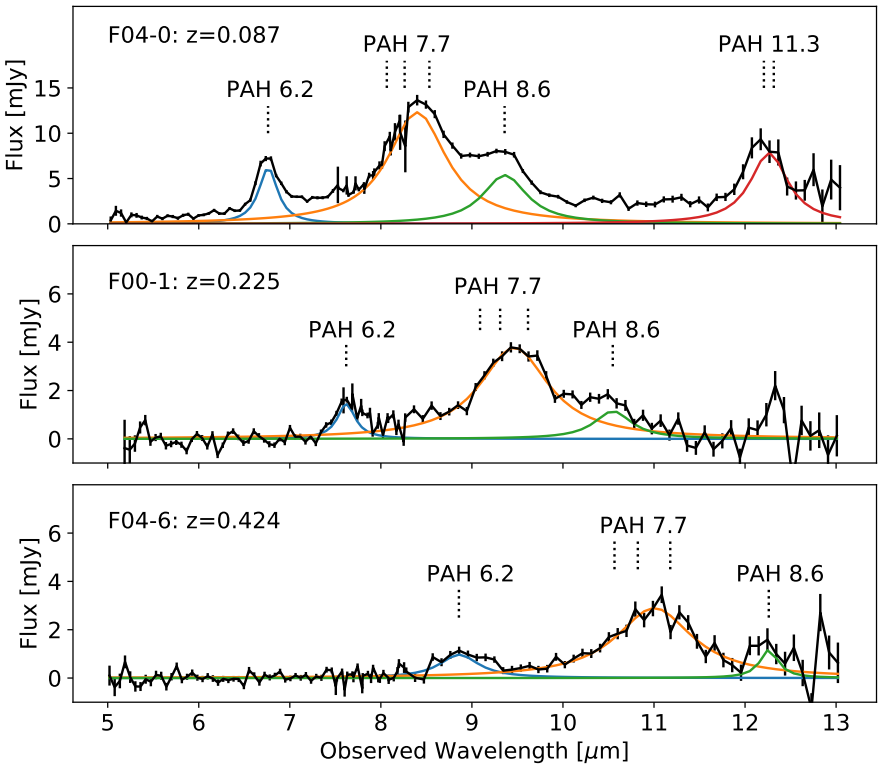

Figure 2.1 Examples of *AKARI* SPICY spectra of star-forming galaxies from Ohyama et al. (2018) with PAH emission detections. Underlying curves represent the authors' Lorentzian fits to the PAH 6.2, 7.7, 8.6, and 11.3 μm emission features.

signal-to-noise is also high enough to resolve the doublet in Hγ (not shown). The fourth panel shows broad blue wings in [O III] emission, suggestive of outflows from an AGN.

We used the Specpro software (Masters & Capak, 2011) to visually inspect each spectrum and to determine an initial redshift guess based on a template of emission and absorption lines. This initial redshift served as the seed for our python routine that used non-linear least-squares fitting. We used Gaussian fits to measure redshifts, emission line fluxes, and equivalent widths for [O II]$\lambda\lambda$3726,3729, Hγ, Hβ, [O III]$\lambda\lambda$4959,5007, Hα, [N II]$\lambda\lambda$6549,6585, and [S II]$\lambda\lambda$6716,6731. In general, a linear local continuum was added. For Hγ and Hβ, the continuum was modeled with a Voigt profile in order to account for underlying stellar absorption.

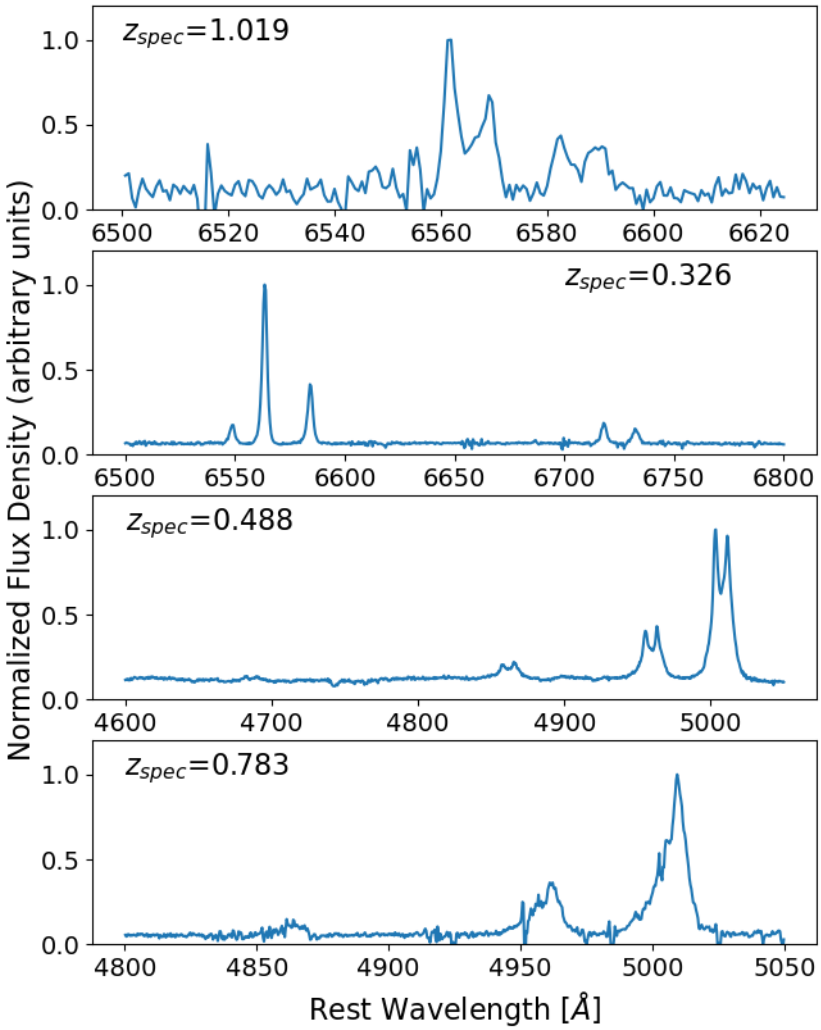

Figure 2.2 Example observations illustrating the quality and variety of our high resolution spectra. The galaxy in the top panel was observed with Keck/MOSFIRE J-band, and the bottom three were observed with Keck/DEIMOS.

For multi-component Gaussian fits, the following constraints were used in order to limit the number of free parameters. When resolved, the [O II]$\lambda\lambda$3726,3729 doublet was fit with a double Gaussian, with the central wavelength and width of [O II]λ3729 fixed relative to [O II]λ3726. The [O III]$\lambda\lambda$4959,5007 lines were fit with a double Gaussian such that the width of [O III]λ4959 was fixed to that of the stronger line λ5007, the central wavelength was fixed relative to the expected separation, and the amplitude was fixed to the theoretical

value of [O III]λ5007/2.98 (Osterbrock, 1989). For the Hα, [N II]$\lambda\lambda$6549,6585 complex, a triple Gaussian was used; the amplitude of [N II]λ6550 was fixed to be [N II]λ6585/3.071 (Osterbrock, 1989), the central wavelengths of [N II] were fixed relative to Hα, and the width of [N II]λ6549 was fixed to be that of λ6585. For Seyfert galaxies where a broad Hα component was detected (FWHM $\gtrsim$ 1000 km/s), an additional underlying Gaussian was added.

2.2.7.1 Metallicity Measurements

We estimate the oxygen abundance of the ionized interstellar medium [1], 12+log(O/H), by using the N2 (log [N II]λ6584/Hα), O3N2 (log ([O III]λ5007/Hβ)/([N II]λ6584/Hα)), and O32 (log ([O III]λ5007/[O II]$\lambda\lambda$3726,3729) indicators. For the N2 and O3N2 indicators, we use the calibrations by Pettini & Pagel (2004), given by:

$$12 + \log(\mathrm{O/H})_{N2} = 8.9 + 0.57 \times \mathrm{N2} \tag{2.2}$$

$$12 + \log(\mathrm{O/H})_{O3N2} = 8.73 - 0.32 \times \mathrm{O3N2} \tag{2.3}$$

where the 1-σ calibration uncertainties are 0.18 dex and 0.14 dex for N2 and O3N2, respectively. When using the N2 indicator, we limit measurements to objects with N2 < -0.3 to avoid saturation in nitrogen. For the O32 indicator, we use the calibration given by Jones et al. (2015):

$$12+\log(\mathrm{O/H})_{O32} = 8.3439 - 0.4640 \times \mathrm{O32} \tag{2.4}$$

which has an uncertainty of 0.11 dex. For reference, solar metallicity is such that 12+log(O/H) = 8.69 (Asplund et al., 2009).

Table 2 lists the total number of Hα and [O II] detections with at least four photometric detections (including upper limits from 7-24 μm and empirical metallicity measurements

[1] We use the terms "oxygen abundance" and "metallicity" interchangeably in this work.

Table 2. Number of Hα and [O II] detections from combined observations.

Instrument	N(Hα)	N([O II])
Keck/DEIMOS	72	196
Keck/MOSFIRE	9	7
MMT/Hectospec, WIYN/Hydra[(a)]	334	422
Subaru/FMOS[(b)]	22	–
	437	625

Note. — All galaxies have at least four photometric detections (including upper limits) from 7-24 μm and empirical metallicity measurements using the emission line ratios [N II]/Hα (for Hα and [N II]-measured sources) and/or O32 (for [O II] sources). References: (a) Shim et al. (2013), (b) Oi et al. (2017).

using either the N2 index (for Hα and [N II]-observed sources) and/or O32 index (for [O II] sources).

2.2.8 AGN selection

To avoid contamination from AGN in our SFR calculations, and to study the impact that the presence of an AGN has on PAH dust luminosity, we classify our sources. We identify AGN candidates using a combination of spectroscopic diagnostics, mid-infrared colors, and X-ray cross-matching. An object is considered to be an AGN if it meets at least one of the four following criteria:

1. the spectrum has broad permitted emission lines (i.e., FWHM $\gtrsim$ 1000 km/s) consistent with a Type 1 Seyfert galaxy;

2. the object is a Type 2 Seyfert galaxy or LINER identified with the "BPT" line ratio diagram such that log([OIII]/Hβ)>0.61/(log([NII]/Hα)-0.02-0.1833$\times z$) + 1.2+0.03$\times z$ (Kewley et al. (2013), Equation 1);

3. for MIR-selected AGN, the *AKARI*/IRC colors are such that N2-N4>0 and S7-S11>0 [AB magnitude] (Lee et al., 2007; Shim et al., 2013); and/or

4. the object has a Chandra X-ray counterpart within 2.5" (Krumpe et al., 2015).

The left panel of Figure 2.3 shows the usual BPT-[NII] emission line ratio diagram for our sources. Based on this diagram, there are 215 star-forming galaxies ("BPT-SF") and 154 AGN candidates ("BPT-AGN"). Based on the MIR colors, there are 779 star-forming galaxies ("MIR-SF") and 157 AGN candidates ("MIR-AGN"). BPT-SF galaxies are 99% consistent with their mid-infrared color classifications; 160 BPT-SF galaxies are also MIR-SF galaxies, while only two BPT-SF galaxies are classified as MIR-AGN. However, the likelihood that a BPT-AGN is classified as a MIR-SF galaxy is high: 121 BPT-AGN are classified as MIR-SF galaxies and 8 are classified as MIR-AGN. This is probably because MIR color selection is stricter, tending to exclude low-luminosity AGN, and many Seyfert 2's which the BPT diagram reveals. Both panels are color-coded by their AGN fraction as determined through SED fitting (Section 2.3.1).

2.3 IRC Measurement of the PAH luminosity

2.3.1 Spectral energy distribution modeling

We matched our Hα detections with their multi-wavelength photometric counterparts, using a matching radius of the full width at half maximum of the telescope point spread function. When available, we merged photometry from the following telescopes: Chandra (Krumpe et al., 2015), *GALEX* FUV and NUV (Burgarella et al., 2019), *CFHT*/MegaCam u*, g', r', i', z' (Oi et al., 2014; Hwang et al., 2007), Subaru/Hyper-Suprime Cam g/r/i/z/Y (Oi et al., 2021), *CFHT*/WIRCAM J and K_S (Oi et al., 2014), *KPNO*/FLAMINGOS J and H (Jeon et al., 2014), *AKARI*/IRC N2, N3, N4, S7, S9W, S11, L15, L18W, L24 (Kim et al., 2012; Murata et al., 2013), *Spitzer*/IRAC1 (3.6 μm) and IRAC2 (4.5 μm) (Nayyeri et al.,

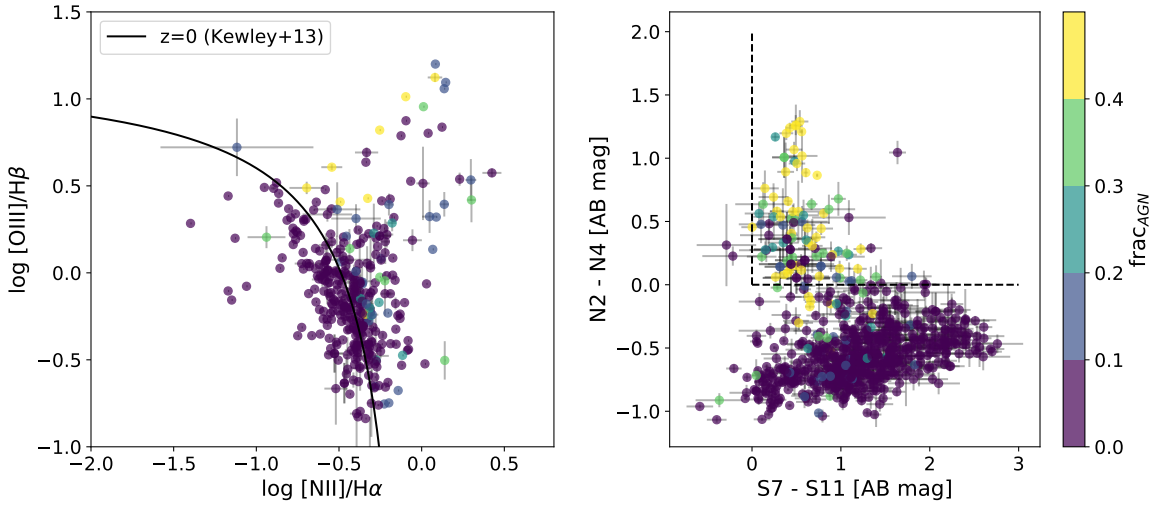

Figure 2.3 Left: BPT-NII diagram based on the redshift-dependent Kewley et al. (2013) equation. The line that separates star formation from AGN at z=0 is shown for reference. Right: Mid-infrared classification with *AKARI* colors for objects with S/N>3 detections in each filter. AGN candidates are found in the region where N2-N4>0 and S7-S11>0 (dashed lines). Both panels are color-coded by their mid-infrared AGN fraction determined from CIGALE SED fits.

2018), *WISE* 12 μm and *WISE* 22 μm (Wright et al., 2010; Jarrett et al., 2011; Cutri et al., 2021), *Herschel*/PACS green (100 μm) and PACS red (160 μm) (Pearson et al., 2019), and *Herschel*/SPIRE 250 μm, 350 μm, 500 μm bands (Pearson et al., 2017). We note that some of these datasets do not cover the entire *AKARI* NEP-Wide field, but our multiwavelength coverage of the NEP-Deep field is reasonably complete.

We modeled spectral energy distributions (SEDs) with the CIGALE software (Code Investigating GALaxy Emission), which is based on the assumption of energy balance between stellar radiation absorbed by dust in the UV/optical and dust emission output in the mid to far-infrared (Boquien et al., 2019). This implicitly requires that our view of the extinction is similar to what observers along most other lines-of-sight to the galaxy would also measure. CIGALE uses Bayesian analysis that combines stellar population models, AGN and ISM

templates[2], and various libraries to determine the best parameters across all possible spectra. We assumed an exponentially decaying star formation history, Chabrier (2003) IMF, Calzetti et al. (2000) dust attenuation model, Draine et al. (2014) dust emission template, and Fritz et al. (2006) AGN emission model. The dust emission model characterizes PAH emission strength based on the q_{PAH} parameter, which is defined as the fraction of the total dust mass in PAH grains with fewer than 10^3 carbon atoms. For reference, the Milky Way dust has $q_{PAH} \approx 4.6\%$ (Draine & Li, 2007).

We define the AGN fraction, $frac_{AGN}$, as the ratio of the AGN luminosity to the total luminosity integrated between 5–10 μm. For star-forming galaxies, we assume $frac_{AGN} = 0$. Otherwise, for AGN candidates and unclassified objects (i.e., objects with incomplete spectroscopic/photometric data), we allowed $frac_{AGN}$ to vary. Figure 2.3 is color-coded by the AGN fraction. The median AGN fraction for BPT-AGN candidates is 0.05 with interquartile range of 0.01–0.13, compared to a median of 0.33 for MIR-AGN candidates with interquartile range of 0.12–0.48. This discrepancy demonstrates the efficacy of the BPT diagram to select weaker AGN than the *AKARI* color-color diagram.

We used a 32-core processor through Amazon Web Services (AWS) cloud computing to run our models at a rate of ∼30,000 models/second. For the final sample, we limit objects to those with $0.5 <$ reduced $\chi^2 < 10$. Table 2 summarizes our input SED parameters. In Figure 2.4, we illustrate the multi-wavelength coverage of our photometric data (purple circles) and show some diverse examples of CIGALE best-fit SEDs which have a range of PAH strengths in the mid-infrared. The light blue region from 2-24 μm highlights the observed wavelength range of the *AKARI*/IRC, and the dotted vertical line indicates the observed wavelength for the PAH 7.7 μm blend. The model spectrum (solid black line) represents the sum over the attenuated stellar emission, dust emission, and AGN emission components. Although we include the contribution from nebular emission when modeling SEDs, we omit it in the

[2]We note that CIGALE includes the option to include user-input nebular emission line fluxes (e.g., Hα, [N II]), which would further constrain the metallicity and q_{PAH} parameters. However, we do not include emission line fluxes in this work, but recommend this option for future studies.

figure for simplicity.

The total infrared luminosity, $L(TIR)$, has been extensively used in the literature as a SFR indicator, and is known to correlate with PAH luminosity (Takagi et al., 2010). We calculate $L(TIR)$ for individual objects by shifting the best-fit SED to the rest frame and integrating from 8–1000 μm. In the Appendix, we test the dependence of FIR photometry on the integrated $L(TIR)$ and find that $L(TIR)$ measurements with and without FIR data are consistent with a root-mean-square (RMS) dispersion of 0.096 dex (Figure 2.21). Therefore, we estimate that our $L(TIR)$ measurements are accurate to within $\sim$20%.

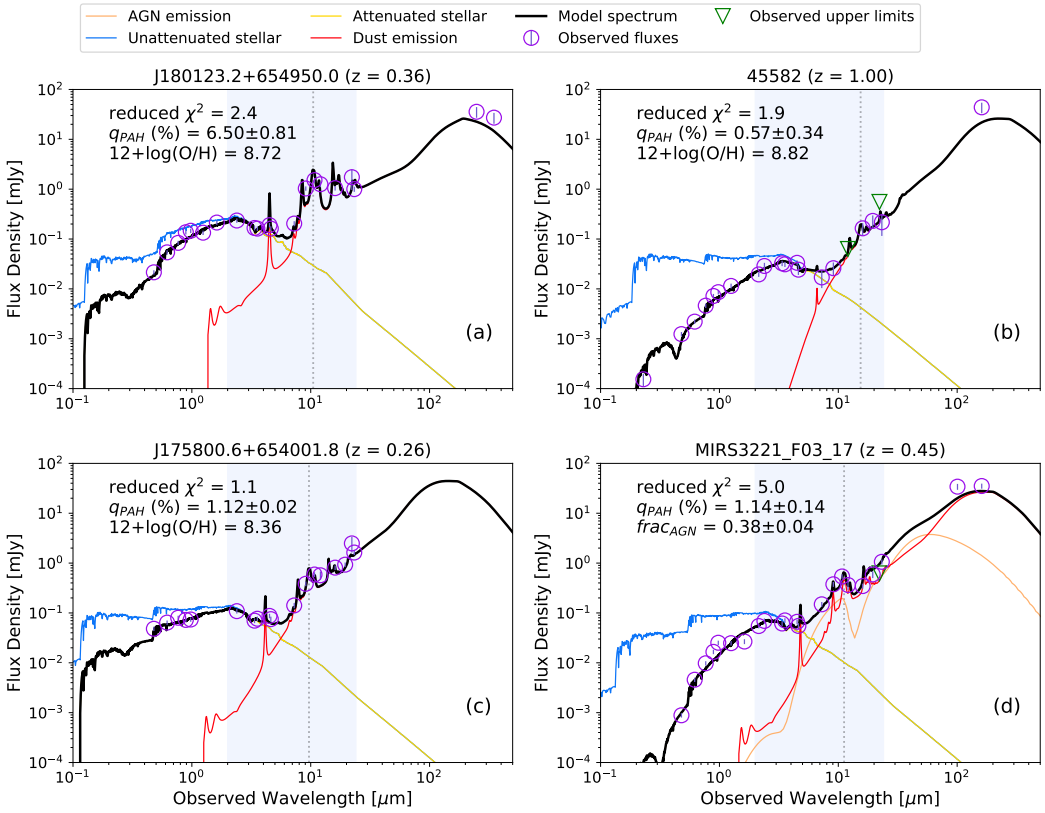

Figure 2.4 Examples of typical CIGALE SED fits, including: (a) star forming "main-sequence' galaxy with solar metallicity and strong PAH emission; (b) metal-rich starburst galaxy (R_{SB}=11) with weak PAH emission; (c) metal-poor starburst galaxy (R_{SB}=18) with weak PAH emission; (d) Type-II BPT-AGN with weak PAH emission.

Table 2. Input parameters for CIGALE SED fitting

Parameter	Description	Value
	Star Formation History: $SFR(t) \propto e^{-t/\tau}$	
τ (Myr)	e-folding time of main stellar population	100, 300, 1000, 2000, 3000, 5000, 10000, 15000, 30000
age (Myr)	age of main stellar population	3, 8, 20, 50, 125, 300, 800, 2000, 5000, 13000
	Stellar Populations	
IMF	Initial Mass Function	Chabrier (2003)
Z	Metallicity	0.02 (solar)
Separation age (Myr)	separation age between young and old stellar populations	10
	Nebular Emission	
$\log(U)$	ionization parameter	-2.0
f_{esc}	fraction of Lyman continuum photons escaping the galaxy	0.0
f_{dust}	fraction of Lyman continuum photons absorbed by dust	0.0
	Dust Attenuation: Calzetti et al. (2000)	
E(B-V)$_{lines}$	color excess of nebular line emission	0.0-1.6 in steps of 0.2
f	ratio of E(B-V)$_{continuum}$ to E(B-V)$_{lines}$	0.44
UV extinction bump wavelength	central wavelength of UV bump in nm	217.5
UV bump width	FWHM of UV bump in nm	35.0
	Dust Emission: Draine et al. (2014)	
q_{PAH} (%)	mass fraction of PAH	0.47, 1.12, 2.50, 3.90, 4.58, 5.26, 5.95, 6.63, 7.32
U_{min}	minimum radiation field	1.0, 5.0
α	power-law slope $dU/dM \propto U^{\alpha}$	2.0
γ	fraction illuminated from U_{min} to U_{max}	0.2
	AGN Emission: Fritz et al. (2006)	
r ratio	ratio of the maximum to minimum radii of the dust torus	60.0
$\tau_{9.7}$	optical depth at 9.7 μm	1.0, 6.0
opening angle	opening angle of dust torus	100.0°
ψ	angle between equatorial axis and line of sight	0.001°, 89.990°
$frac_{AGN}$	AGN fraction	0.0, 0.05, 0.1, 0.15, 0.2, 0.25, 0.3, 0.35, 0.4, 0.45, 0.5

2.3.2 Calibration sample characteristics

Figure 2.5 shows the specific star formation rate (sSFR) as a function of redshift of all galaxy candidates with Hα and/or [O II] detections. The sSFR, the mass-normalized star formation rate, is given by Kennicutt (1998) as

$$sSFR\ [yr^{-1}] = [1.72 \times 10^{-10} \times (L(TIR)/L_{\odot})]/[(M_{*}/M_{\odot})/0.61], \tag{2.5}$$

where $L(TIR)$ is the total IR luminosity of the best-fit SED integrated from rest-frame 8–1000 μm and ($M_{*}/M_{\odot}$)/0.61 is the stellar mass converted from Chabrier (2003) to Kennicutt (1983) IMF. "Main-sequence" galaxies are defined as objects with $13 \times t_{cosmic}^{-2.2} \leq$ sSFR [1/Gyr] $\leq 52 \times t_{cosmic}^{-2.2}$, where t_{cosmic} is the cosmic time elapsed since the Big Bang in Gyr (Elbaz et al., 2011). "Starburst" galaxies and "quenched" galaxies lie above and below this region, respectively. To classify starburst galaxies, we adopt the R_{SB} starburst parameter from Elbaz et al. (2011), which describes the "starburst excess" relative to main-sequence star formation and is defined as the ratio of the sSFR to the main-sequence sSFR. With their definition, starburst galaxies have $R_{SB} \gtrsim 2$ (blue star symbols), main-sequence galaxies have $0.5 \lesssim R_{SB} \lesssim 2$ (black triangle symbols), and quenched galaxies have $R_{SB} \lesssim 0.5$ (red circle symbols).

Our final PAH-derived SFR calibration sample consists of main-sequence and starburst galaxies with Hα and/or [O II] emission lines and metallicities measured using the N2, O3N2, and/or O32 line ratio indices. The sample includes 319 galaxies with Hα detections and 332 galaxies with [O II] detections. There are a total of 443 unique sources. We summarize the main properties of this sample in Figure 2.6. The redshift, stellar mass, and total IR luminosity range from $0.048 < z < 1.025$, $10^{8.7}$ $M_{\odot} < M_{*} < 10^{11.2}$ $M_{\odot}$, and $10^{8.7}$ $L_{\odot} <$ L(TIR) $< 10^{12}$ $L_{\odot}$, respectively.

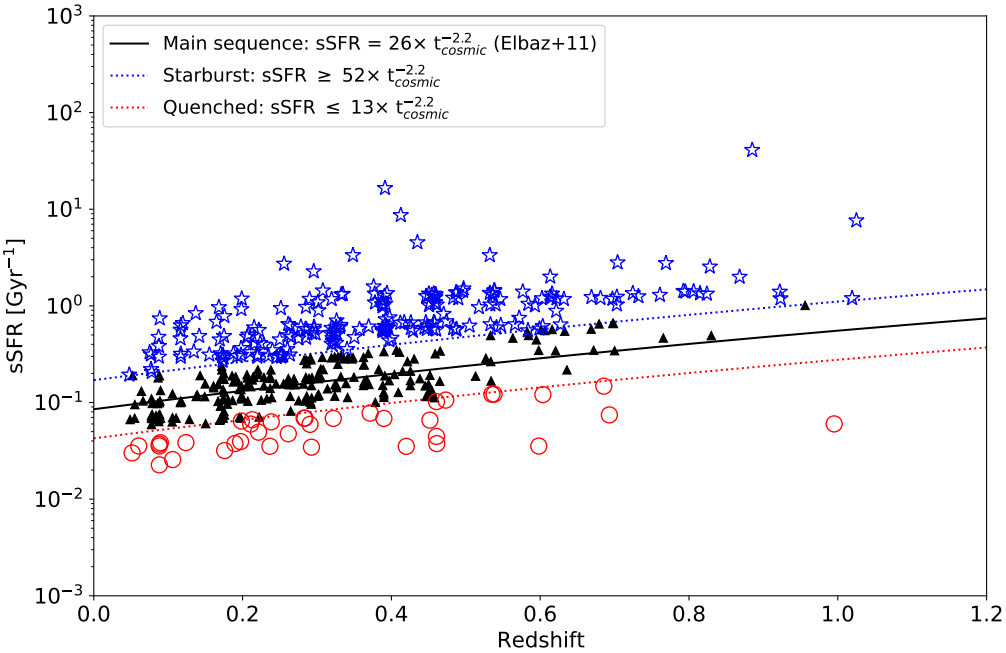

Figure 2.5 Specific star formation rate as a function of redshift for galaxies with Hα and/or [O II] detections in the calibration sample.

2.3.3 Extinction-corrected Hα and [O II] Luminosity

We calculate dust-corrected Hα luminosities using three methods: the 24 μm rest-frame monochromatic luminosity ($\lambda L_\lambda(24\ \mu\mathrm{m})$) correction, the Balmer decrement (Hα/Hβ), and the color excess E(B-V) derived with CIGALE. The 24 μm correction to Hα defined by Kennicutt (1998) is given as:

$$L(H\alpha)_{24\ \mu m} = L(H\alpha)_{obs} + 0.02 \times \lambda L_\lambda(24\ \mu m)\ [\mathrm{erg/s}] \tag{2.6}$$

where $L(H\alpha)_{obs}$ is the observed Hα luminosity and luminosities are in erg/s. We calculate $\lambda L_\lambda(24\ \mu\mathrm{m})$ as the rest-frame luminosity density of the best-fit SED in the *Spitzer*/MIPS 24 μm filter multiplied by the effective wavelength. The intrinsic Hα luminosity is given by:

$$L(H\alpha) = L(H\alpha)_{obs} \times 10^{0.4A(H\alpha)} \tag{2.7}$$

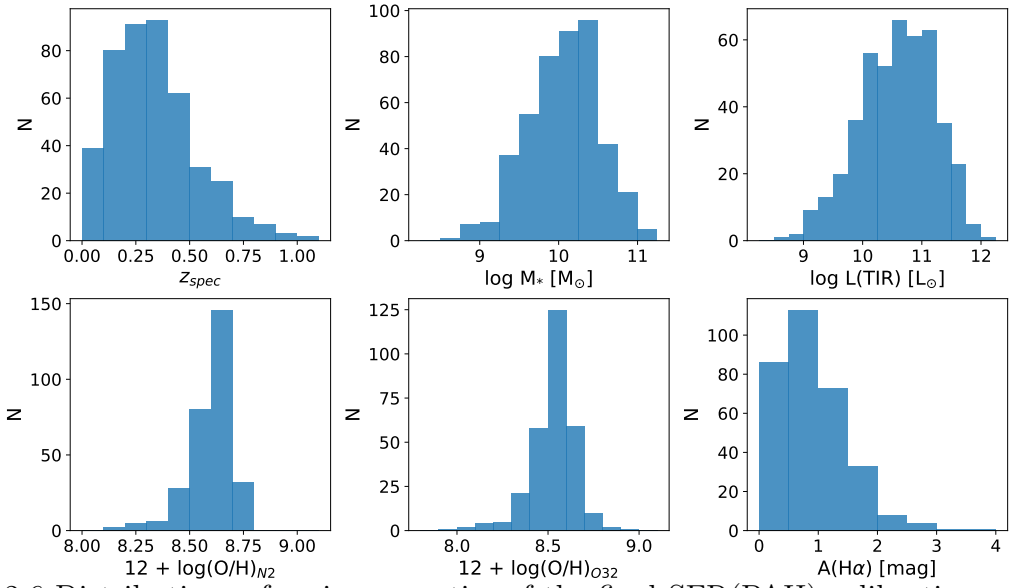

Figure 2.6 Distributions of main properties of the final SFR(PAH) calibration sample with Hα and/or [O II] emission line detections. From left to right: spectroscopic redshift, stellar mass, total infrared luminosity, metallicity based on N2 index, metallicity based on O32 index, and attenuation in Hα based on SED fitting.

where $A(H\alpha)$ is the attenuation in Hα in magnitudes. For star-forming galaxies with Hα and Hβ flux measurements, $A(H\alpha)$ is given by the Balmer decrement (BD):

$$A(H\alpha)_{BD}\ [\mathrm{mag}] = 3.33 \times 1.97 \times \log\left(\frac{(F(H\alpha)/F(H\beta))_{obs}}{2.86}\right) \tag{2.8}$$

where (F(Hα)/F(Hβ))$_{obs}$ is the observed flux ratio, and we assume the Calzetti et al. (2000) attenuation law and an intrinsic flux ratio of 2.86 (Case B recombination and T=10^4 K; Osterbrock (1989)). The SED-derived $A(H\alpha)$ is given by:

$$A(H\alpha)_{CIGALE}\ [\mathrm{mag}] = 2.45 \times E(B-V)_{lines} \tag{2.9}$$

where E(B-V)$_{lines}$ is the color excess of the nebular lines' light, and we assume a standard Milky Way extinction curve.

Figure 2.7 shows a comparison of intrinsic Hα luminosities for the galaxies in the calibration sample with Hα and Hβ flux measurements. Heavily dust-reddened objects with $A(H\alpha) > 3$ mag as calculated via the Balmer decrement are shown in red squares. In these objects, the dust-corrected Hα luminosity deviates significantly from those derived via the 24 μm luminosity and predicted CIGALE extinction, as shown in panels (a) and (b). However, as shown by panel (c), the corrections given by the 24 μm and CIGALE methods produce similar intrinsic Hα luminosities, which is most likely due to their shared dependence on MIR photometry. The scatter between the Balmer decrement correction and 24 μm luminosity correction has been observed in other studies (e.g., Boselli et al., 2015, Shipley et al., 2016). They attribute the discrepancy as being due to uncertainty in the underlying stellar absorption correction for objects with weak Hβ emission.

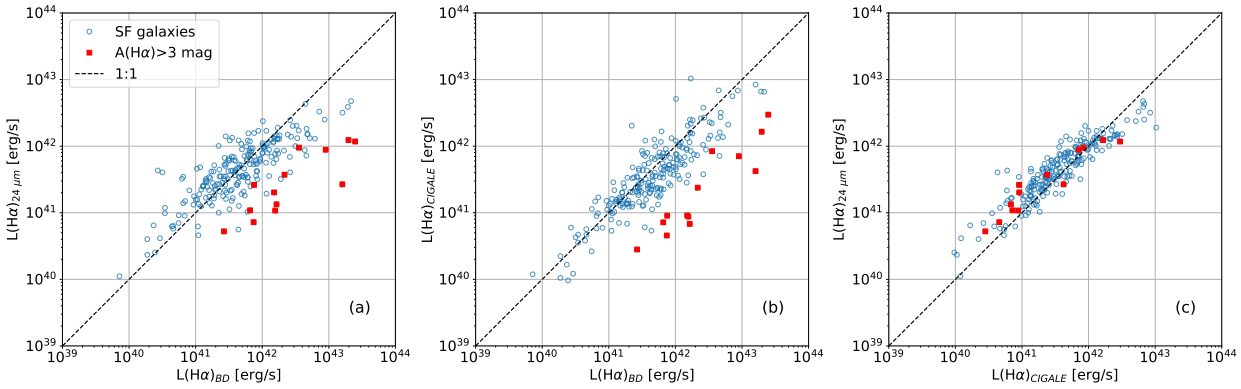

Figure 2.7 Intercomparison of corrected Hα luminosities derived from our three different de-reddening methods.

To correct the [O II] luminosity for dust extinction, we adopt the calibration given in Kennicutt (1998):

$$L([OII])_{24\ \mu m} = L([OII])_{obs} + 0.029 \times \lambda L_{\lambda}(24\ \mu m), \tag{2.10}$$

where the luminosities are in erg/s. The [O II] SFR is then given by Kennicutt (1998) as:

$$SFR\ [M_{\odot}/yr] = 8.1 \times 10^{-42} L([OII])_{24\ \mu m}\ [erg/s] \tag{2.11}$$

assuming a Salpeter IMF. We discuss limitations of using the [O II] luminosity to measure SFR in the Appendix.

2.3.4 Measurement of PAH luminosity

We input the rest-frame, best-fit SEDs from CIGALE into PAHFIT (Smith et al., 2007; Smith & Draine, 2012) in order to model the dust emission and continuum from 5-35 μm, and to extract the PAH luminosities. The input best-fit SEDs include the attenuated stellar emission, nebular emission, and dust emission (i.e., modeled AGN emission is removed for AGN candidates). Then, we resample the model spectrum into the *Spitzer*/IRS wavelength grid. PAHFIT uses *Spitzer*/IRS templates to model the MIR continuum with a summation of blackbodies and the PAH dust blends with Drude profiles. Because it does not take AGN emission into account, we only consider SED components from the total attenuated stellar light, nebular emission, and dust emission. For the PAH features, we fixed the central wavelengths and FWHM to their standard values and allowed the amplitudes to vary. Figure 2.8 shows a typical PAHFIT result for a star-forming galaxy. The integrated intensity of the Drude profile is equal to

$$I^{(r)} = \frac{\pi c}{2} \frac{b_r \gamma_r}{\lambda_r}, \tag{2.12}$$

where λ_r is the central wavelength of the PAH feature, γ_r is the fractional FWHM, and b_r is the central amplitude (Smith et al., 2007). For example, the luminosities for the PAH 6.2 μm and 7.7 μm emission features are given by:

$$L(\text{PAH 6.2 } \mu m)\ [erg/s] = 10^7 \times 4\pi d_L^2 \frac{\pi c}{2} \times \left(\frac{0.030\ b_{6.22\mu m}}{6.22\ \mu m} \right) \tag{2.13}$$

$$L(\text{PAH 7.7 } \mu m)\ [erg/s] = 10^7 \times 4\pi d_L^2 \frac{\pi c}{2} \times \left(\frac{0.126\ b_{7.42\mu m}}{7.42\ \mu m} + \frac{0.044\ b_{7.60\mu m}}{7.60\ \mu m} + \frac{0.053\ b_{7.85\mu m}}{7.85\ \mu m} \right) \tag{2.14}$$

with amplitudes b_r in units of W/m^2/Hz, luminosity distance d_L in meters, and c in μm/s.

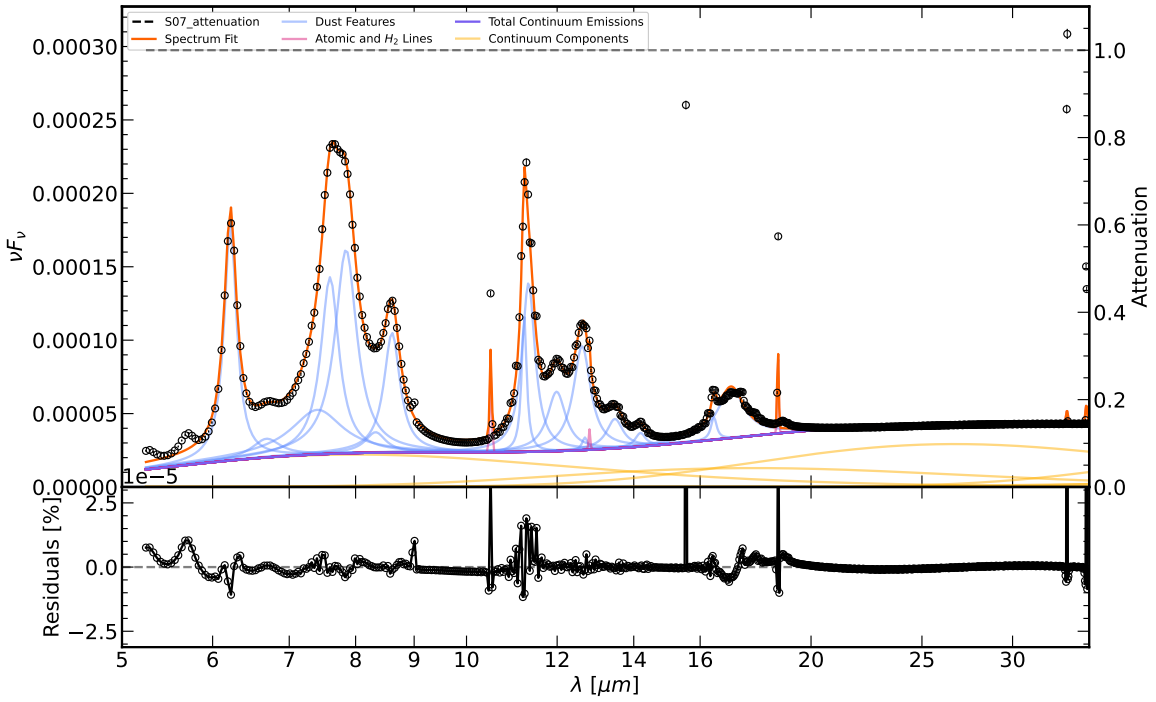

Figure 2.8 Example of a typical PAHfit result for a main-sequence galaxy at z=0.36 (ID: J180123.2+654950.0; The SED is shown in Figure 2.4(a)), fit to the model SED (circle points). The solid red line shows the best-fit result. Drude profile fits to the PAH dust emission features are shown in blue. The solid purple line underlying the emission represents the continuum, which is the summation of the individual blackbody components shown in yellow.

2.3.4.1 Validation of PAH luminosity measurements

Figure 2.9 compares our PAH luminosity measurements for the 6.2 μm and 7.7 μm features to those by Ohyama et al. (2018) in their SPICY spectra of the same galaxies. The figure demon-

strates the validity of our method for measuring $L(PAH\ 6.2\ \mu m)$ and $L(PAH\ 7.7\ \mu m)$, with systematic offsets of only ~ 0.1 dex and ~ 0.2 dex, respectively. The small root-mean-square (RMS) dispersions, $\sigma_{L(PAH\ 6.2\ \mu m)} = 0.19$ and $\sigma_{L(PAH\ 7.7\ \mu m)} = 0.14$, represent the approximate errors in our PAH luminosity measurements. Our measurements of $L(PAH\ 7.7\ \mu m)$ have a larger systematic offset from Ohyama et al.'s measurements compared to those of $L(PAH\ 6.2\ \mu m)$, which is likely due to the difficulty in constraining the underlying continuum beneath the wide 7.7 μm blend in noisy spectra. Their method uses a single broad Lorentzian to fit the 7.7 μm blend from low resolution spectra, which may overestimate the flux somewhat.

In addition to the PAH luminosity, we also calculated the peak luminosity at 7.7 μm, $\nu L\nu(7.7\mu\mathrm{m})$, which is sometimes used as a proxy for the PAH luminosity in the literature because it can be estimated photometrically (e.g., Takagi et al., 2010). The relation for the peak luminosity is:

$$\nu L_\nu(7.7\mu m) = F_\nu(7.7\mu m) \times 4\pi d_L^2 \nu(7.7\mu m), \tag{2.15}$$

where $F_\nu(7.7\mu m)$ is the best-fit spectrum from PAHFIT evaluated at 7.7 μm (i.e., the sum of the blackbody continuua and Drude profiles at 7.7 μm) and $\nu(7.7\mu m)$ is the frequency at 7.7 μm in Hz.

2.4 Analysis

2.4.1 Effects of starburst intensity, metallicity, and AGN fraction

To determine how well PAH luminosities predict SFR, we correlate the PAH 6.2 μm and 7.7 μm luminosities with the reddening-corrected Hα and [O II] luminosities. Figure 2.10 shows the PAH 6.2 μm and 7.7 μm luminosity as a function of observed (reddened) Hα and [O II] luminosity. The four panels show a positive correlation between PAH luminosity and observed Hα and [O II] luminosity, with considerable scatter due to reddening effects which

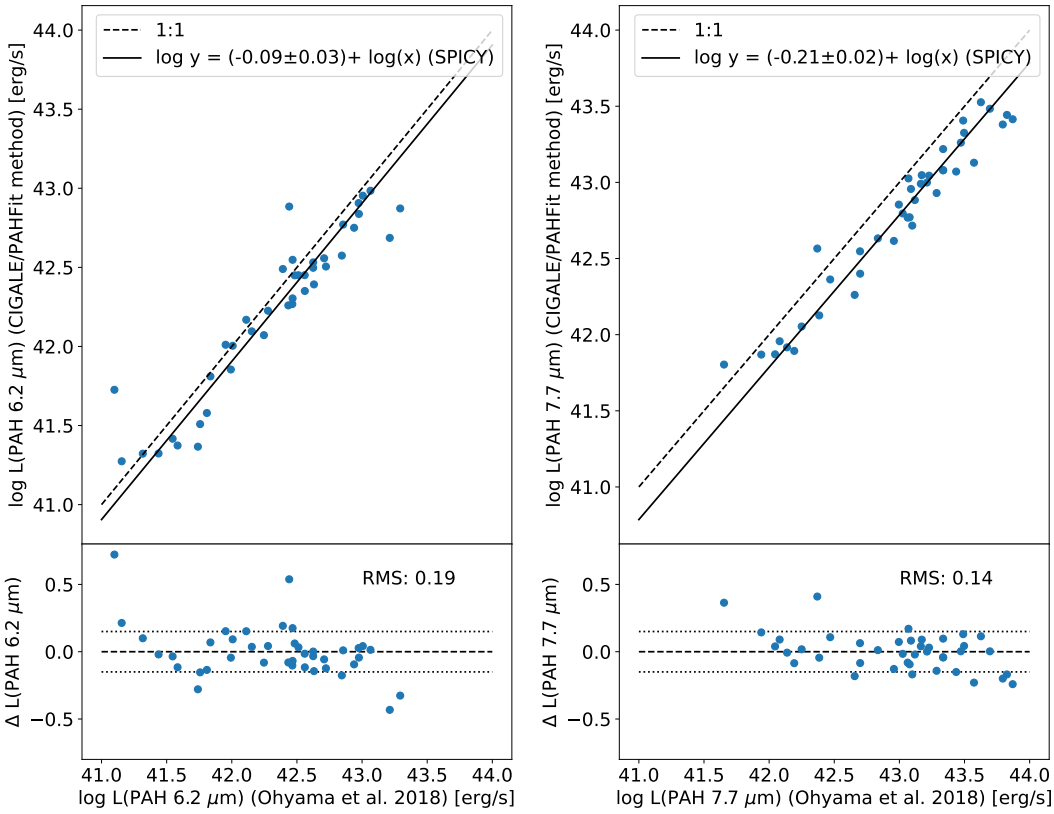

Figure 2.9 Top panel: Comparison between measured PAH luminosity from Ohyama et al. (2018) SPICY sample and inferred luminosity from our CIGALE and PAHFIT method for 6.2 μm (left) and 7.7 μm (right) blends. The solid line represents the least-squares linear fit to the data with slope fixed to unity. Bottom panel: Residuals as a function of the measured PAH luminosity with the dotted lines indicating the RMS dispersion.

have not yet been taken into account.

Figures 2.11 shows the PAH 7.7 μm luminosity as a function of the de-reddened Hα luminosity. We fit linear relations of the form $\log L(PAH\ 7.7\ \mu m) = c_0 + c_1 \times \log L(H\alpha)$ to the star-forming sample. Quenched galaxies (red square symbols) are shown for reference but are excluded from the fits. The three panels in Figure 2.11 show results for different methods of correcting the observed Hα luminosity as discussed in Section 2.3.3. Compared to Figure 2.10, the scatter between $L(PAH\ 7.7\ \mu m)$ and $L(H\alpha)_{24\ \mu m}$ is significantly reduced; the RMS

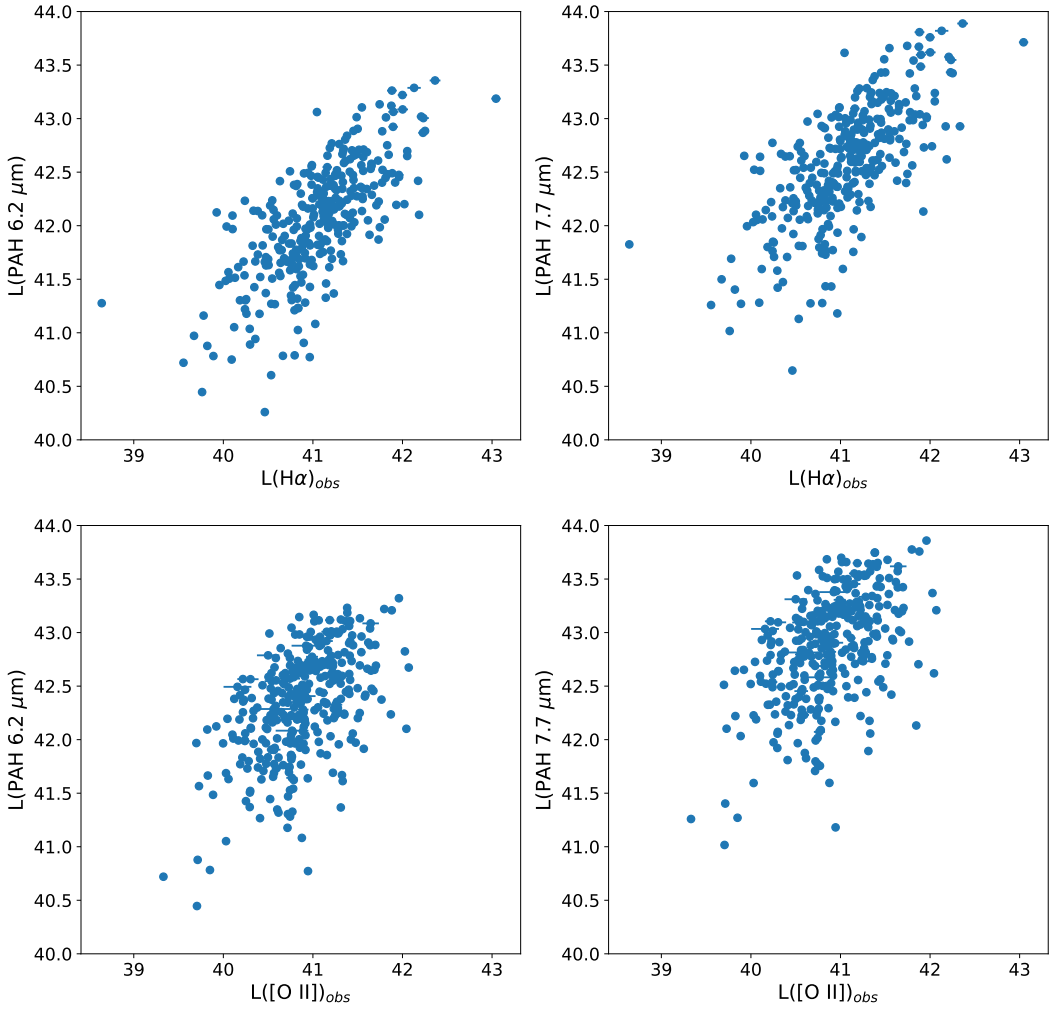

Figure 2.10 PAH 6.2 μm (left column) and 7.7 μm (right column) luminosities vs. observed Hα and [O II] luminosities.

dispersion of the fit is 0.31 dex. The dotted line in panel (a) represents the linear relation from Shipley et al. (2016) derived from *Spitzer*/IRS galaxies with solar metallicity at $z < 0.4$. For the majority of galaxies, $L(PAH\ 7.7\ \mu m)$ is linearly correlated with $L(H\alpha)_{24\ \mu m}$ (i.e., slope $\sim$ 1). However, we find that a small minority, 47/319 (15%), of the galaxies deviate from the fit by -0.4 dex, contributing to the uncertainty in the normalization and non-linear

slope. Panels (b) and (c) show that the correlations between $L(PAH\ 7.7\ \mu m)$ and $L(H\alpha)$ are non-linear with the Balmer decrement and SED fitting corrections, with the Balmer decrement method resulting in the most scatter.

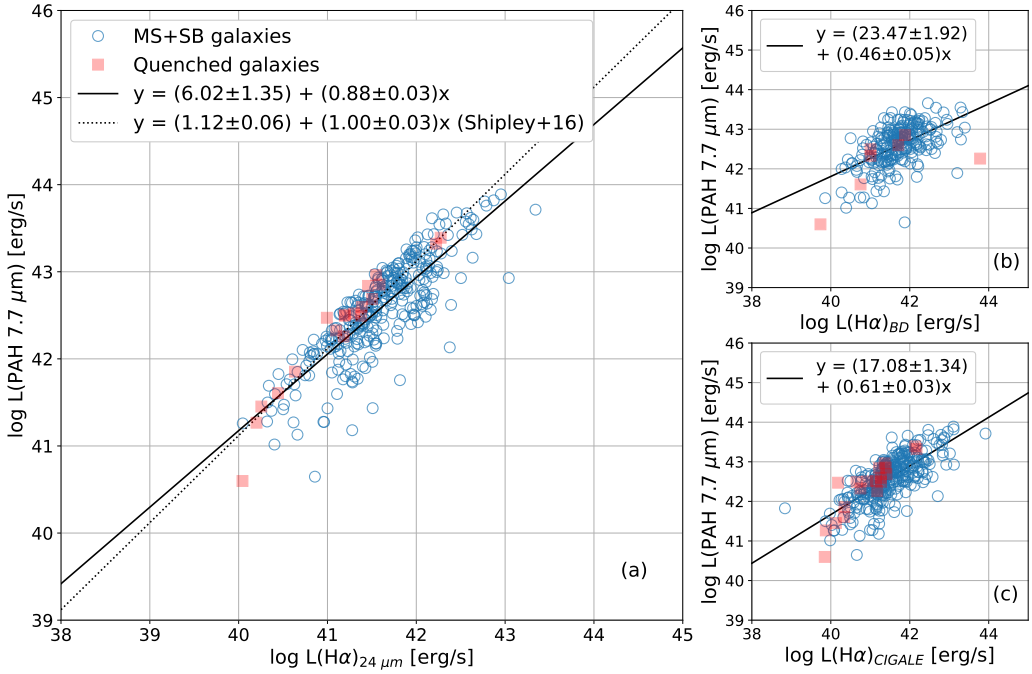

Figure 2.11 Comparison of PAH 7.7 μm luminosity vs. intrinsic Hα luminosity of main-sequence and starburst galaxies for different dust extinction correction methods: (a) rest-frame 24 μm luminosity correction from Kennicutt et al. (2009); (b) Balmer decrement; (c) SED fitting. The solid lines represent linear fits.

Figure 2.12 shows the correlations between the PAH 6.2 μm and 7.7 μm luminosities with the dust-corrected Hα luminosity for the star-forming sample, with main-sequence and starburst galaxies fit separately. For main sequence galaxies, the linear and unity slope fits for the PAH 7.7 μm luminosities are consistent with the relations found by Shipley et al. The linear relations for $L(PAH\ 6.2\ \mu m)$ in main-sequence galaxies are also consistent within $\sim$0.25 dex. The figure demonstrates that starburst galaxies have lower PAH luminosities for a given intrinsic Hα luminosity. If we assume unity slope in the linear fits, the trend for

starburst galaxies has a systematic offset of $\sim$0.35 dex relative to that of main-sequence galaxies for both PAH 6.2 μm and 7.7 μm features, suggesting that starburst galaxies are either PAH-deficient for fixed Hα luminosity or Hα-enhanced for fixed PAH luminosity.

The offset between starburst galaxies and main-sequence galaxies is also present in the correlation between PAH luminosity and dust-corrected [O II] luminosity, as shown in Figure 2.13. Starburst galaxies are systematically lower by a factor of 0.3 dex. We also find that linear fits to the main-sequence sample of the form $\log L(PAH) = c_0 + c_1 \times \log L([OII])$ result in a shallower slope compared to fits with respect to $L(H\alpha)$ such that $L(PAH) \propto L([OII])^{0.9}$.

We further examine the dependence of PAH luminosity on starburst intensity, metallicity, and AGN strength by plotting the log ratio of PAH luminosity to intrinsic Hα and [O II] luminosity as a function of PAH equivalent width (EW) in Figure 2.14. The equivalent width is calculated as the flux of the PAH emission feature (given by PAHFIT) divided by the flux density of total sum of the blackbody continuua evaluated at the central wavelength of the feature. We note that it is difficult to constrain the values for $EW(PAH\ 7.7\ \mu m)$ for individual galaxies because the calculation relies heavily on assumptions for the underlying continuum shape and blend of Drude profiles. However, the exact equivalent widths do not affect our overall interpretations. The top and middle rows of the figure show the correlations for star-forming galaxies, color-coded by starburst parameter and metallicity, respectively. The bottom row shows the correlations for AGN candidates, color-coded by AGN fraction. Objects with low PAH equivalent width (i.e., $EW(PAH\ 6.2\ \mu m) \lesssim 1\ \mu m$ or $EW(PAH\ 7.7\ \mu m) \lesssim 4 \mu m$) scatter downwards from the $L(PAH\ 6.2/7.7\ \mu m)$ and dust-corrected $L(H\alpha)/L([OII])$ fits. The figure demonstrates that galaxies with higher starburst intensity (R_{SB}) have lower $L(PAH\ 6.2\ \mu m)$ and $L(PAH\ 7.7\ \mu m)$ for a given $L(H\alpha)_{24\ \mu m}$ and that AGN with higher AGN fraction have lower $L(PAH\ 6.2\ \mu m)$ and $L(PAH\ 7.7\ \mu m)$ for a given $L([OII])_{24\ \mu m}$.

As the effects of metallicity are less obvious in Figure 2.14, we show $L(PAH\ 7.7\ \mu m)$ as a function of metallicity in Figure 2.15. The Spearman rank-order correlation coefficient

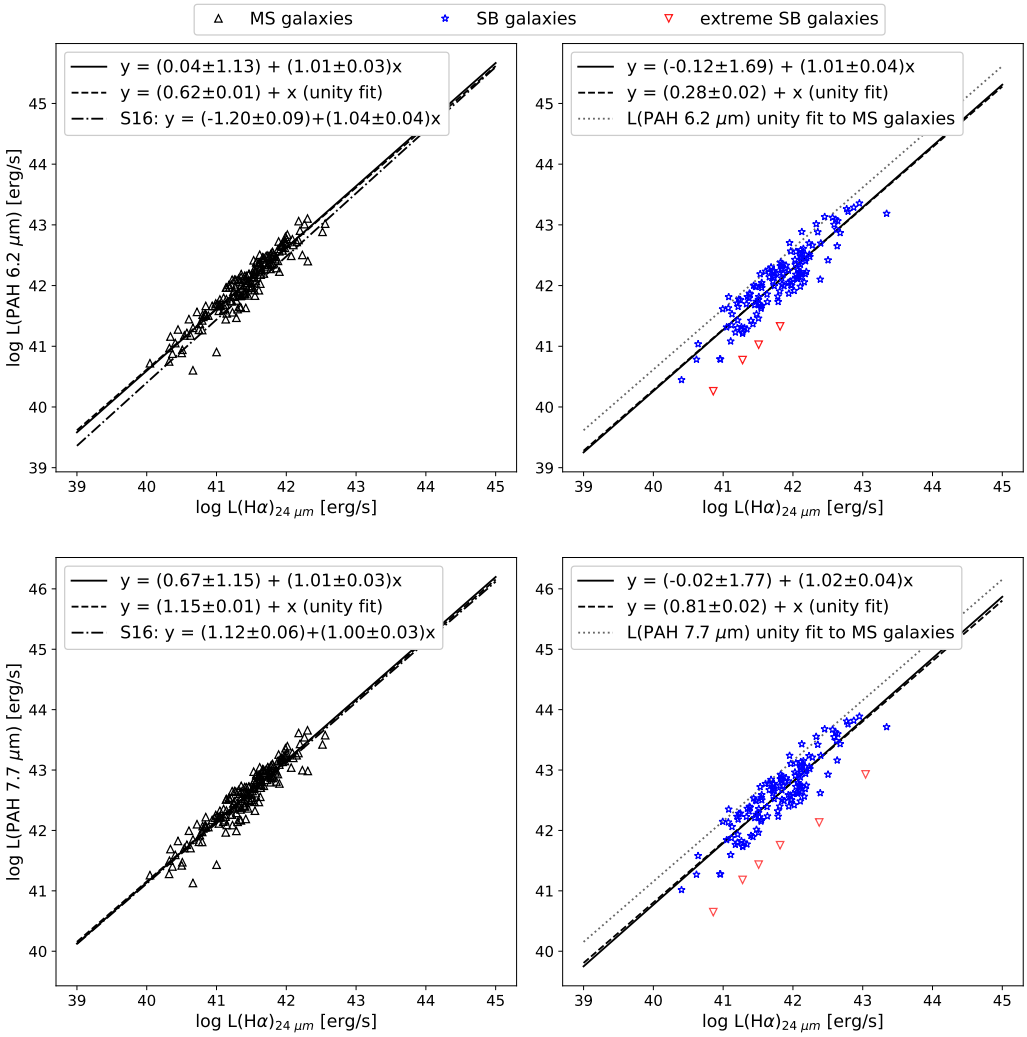

Figure 2.12 Relation between PAH 6.2 μm and 7.7 μm luminosities and intrinsic Hα luminosity for star-forming galaxies. Main-sequence galaxies (black triangles) are shown in the left column, and starburst galaxies (blue stars) are shown in the right column. Extreme starburst galaxies are shown as red triangles. The solid and dashed lines represent linear and fixed unity fits, respectively. The dash-dotted line represents the linear relation given by Shipley et al. (2016).

between $L(PAH\ 7.7\ \mu m)$ and 12+log(O/H)$_{N2}$ (left panel) is 0.23 with p-value of 3×10^{-6}, indicating weak monotonic correlation. The relation against the O3N2 indicator (right panel) is moderately correlated with a Spearman coefficient of 0.41 and 8×10^{-10} p-value.

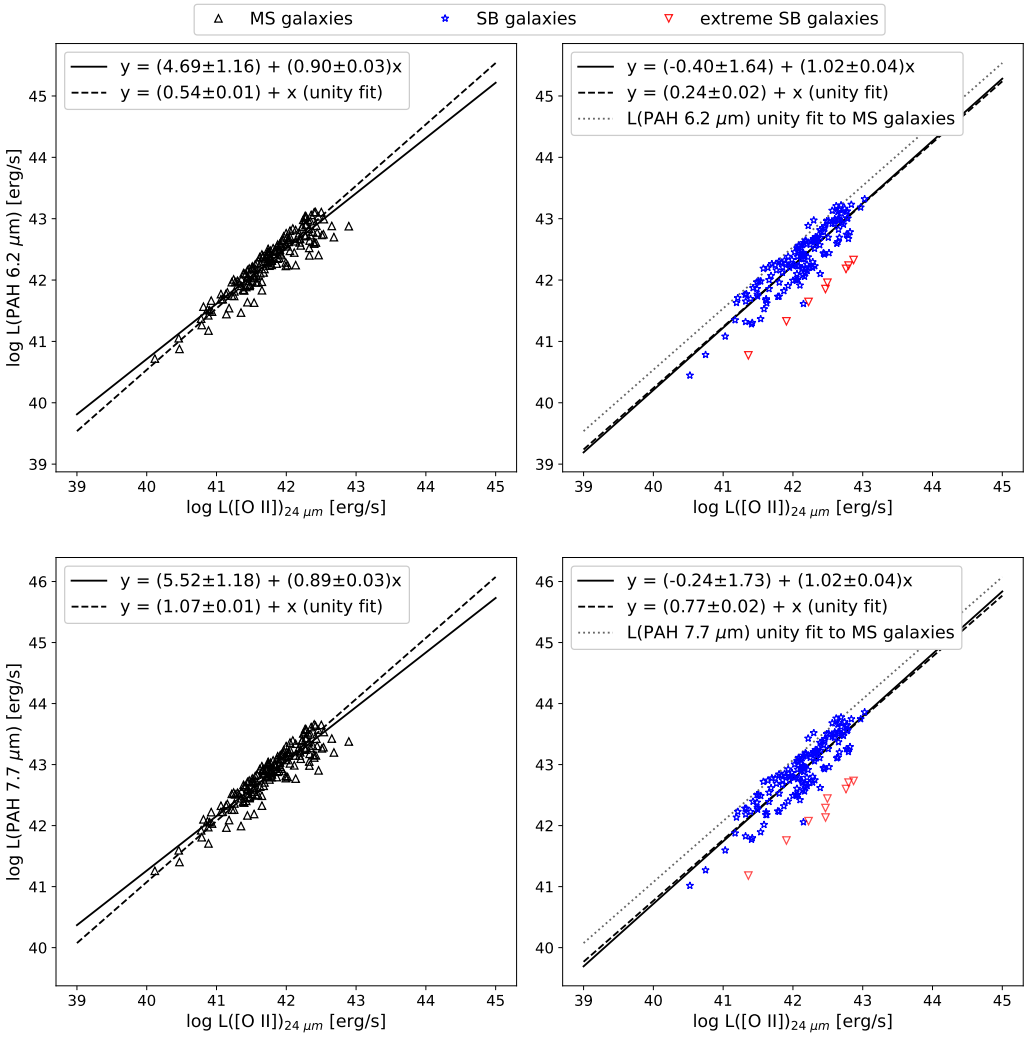

Figure 2.13 Relations between PAH 6.2 μm and 7.7 μm luminosities and intrinsic (dereddened) [O II] luminosities for star-forming galaxies. Symbols and lines are the same as for Figure 2.12.

In Figure 2.16, we compare the PAH contribution to the total IR luminosity in star-forming galaxies and AGN by showing the distributions of the total PAH luminosity, $L(PAH)$, to $L(TIR)$ for objects with at least one *Herschel* FIR detection. We define $L(PAH)$ as the sum of luminosities from PAH emission features at 6.2, 7.7, 8.6, 11.3, 12.6, and 17 μm. Star-forming galaxies are shown in the top panel and AGN are shown in the bottom panels,

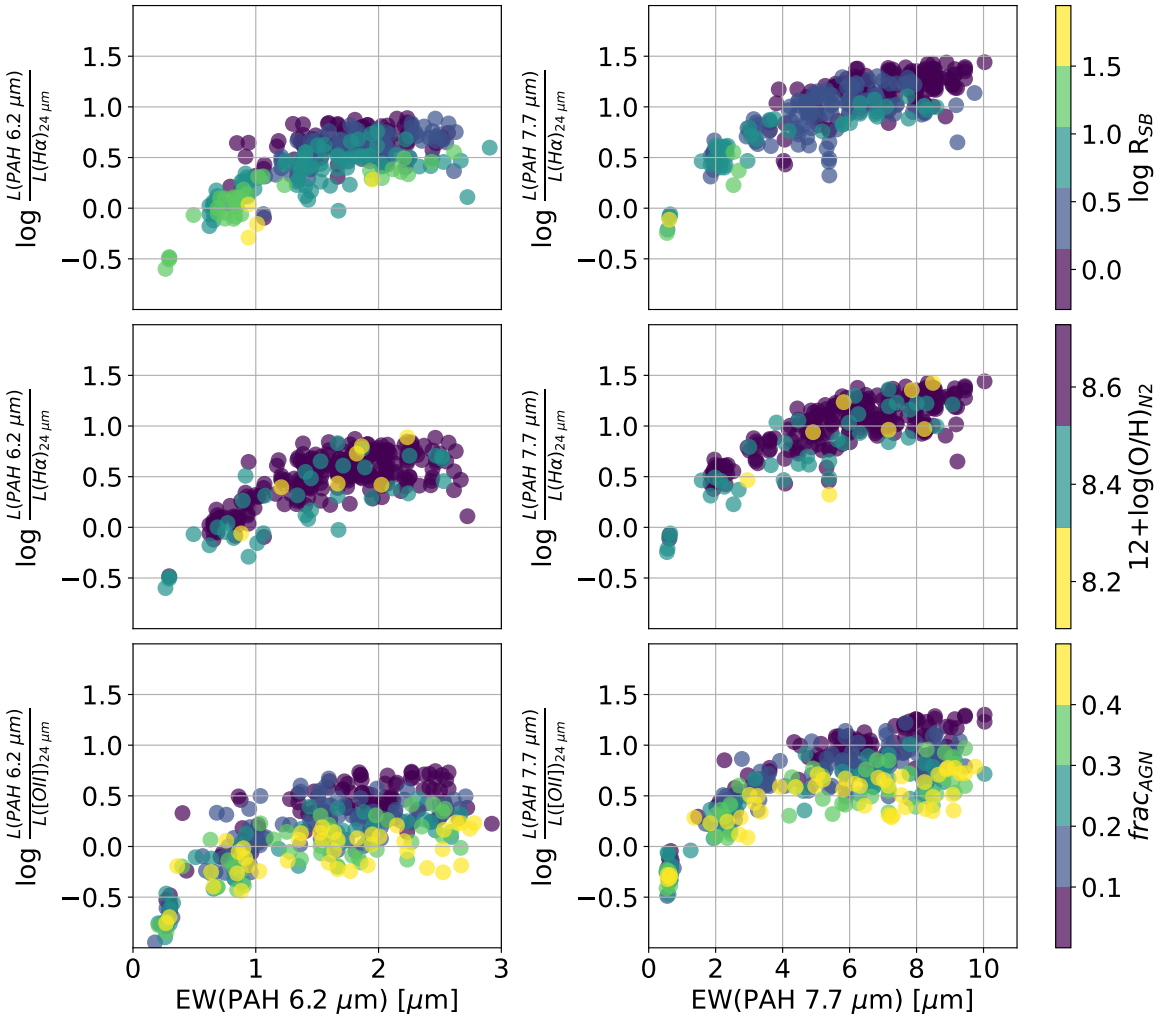

Figure 2.14 Effects of starburstiness (ratio of SFR to main sequence, shown with color bar on top row), gas metallicity (middle row), and AGN fraction (bottom row) on the correlation between PAH luminosity and intrinsic Hα and [O II] luminosity.

with the bottom-most panel separating out "weak" AGN (i.e., $frac_{AGN} < 0.1$) from stronger AGN (i.e., $frac_{AGN} > 0.1$). We find that $L(PAH\ 7.7\ \mu m)$ contributes a median $\sim 45\%$ of the total PAH luminosity, and that the total PAH luminosity in turn can contribute up to $\sim 20\%$ of $L(TIR)$. The median $L(PAH)/L(TIR)$ for star-forming galaxies (main-sequence

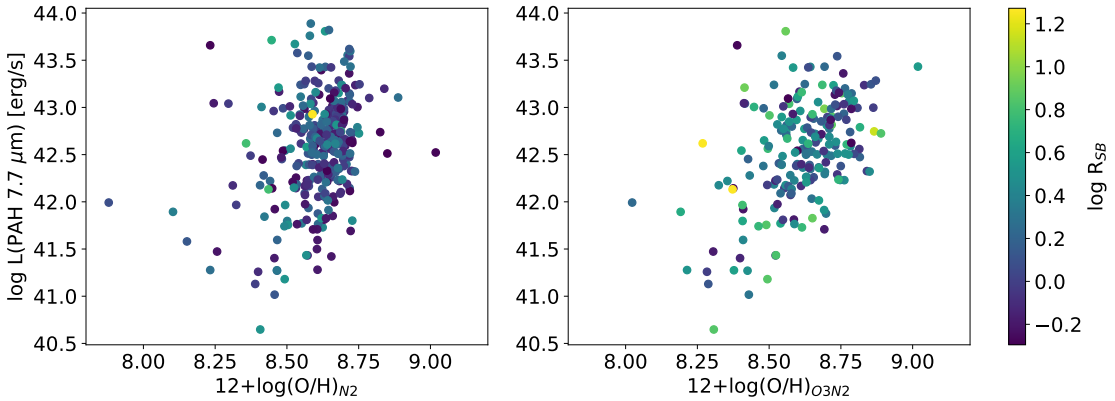

Figure 2.15 PAH 7.7 μm luminosity as a function of metallicity calculated using the N2 index (left) and O3N2 index (right).

and starburst galaxies) is 0.08 with an interquartile range of 0.05 to 0.14. The median in the AGN sample is lower at 0.06 with an interquartile range of 0.03 to 0.10. Objects that are more AGN-dominant with $frac_{AGN} > 0.1$ have lower $L(PAH)/L(TIR)$ with a median 0.04. Our results are consistent with those of Shipley et al. (2013). A simple interpretation is that up to half of the TIR luminosity in AGN may be produced by the AGN itself, rather than from star formation.

2.4.2 The PAH SFR calibration

Assuming that PAH luminosity corrections for metallicity and starburst intensity are both simply linear, we perform a multiple linear fit to the PAH luminosity with the dust-corrected Hα luminosity, R_{SB} parameter, and metallicity as independent variables in the form of: log L(PAH) = c_0 + c_1×R_{SB} + c_2×(12+log(O/H)$_{index}$ - 8.6) + c_3×[log $L(H\alpha)_{24\ \mu m}$ - 42] [erg/s], where the constant 8.6 is the median metallicity and 42 is the median logarithm of the

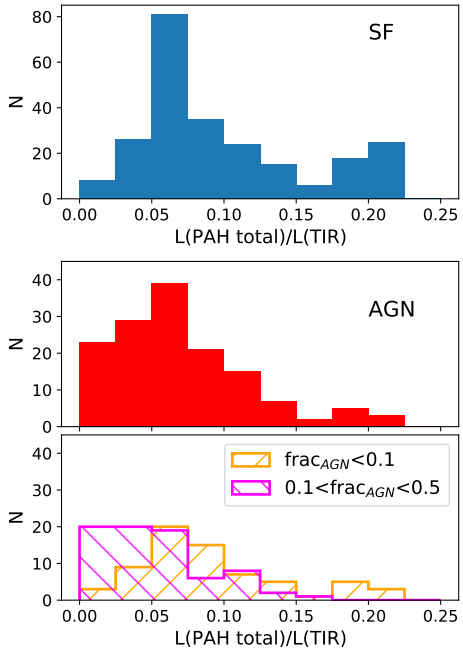

Figure 2.16 Distributions of the ratio of total PAH luminosity to the total infrared luminosity for star-forming galaxies (top panel) and AGN (middle panel). The bottom panel shows the histograms of PAH/TIR separately for the "strong" and "weak" AGN that were shown together in the middle panel.

intrinsic Hα luminosity. The relation with respect to the 7.7 μm PAH luminosity is:

$$\log L(PAH\ 7.7\ \mu m)\ [erg/s] = (43.01 \pm 0.02)$$
$$-(0.02 \pm 0.003)R_{SB} + (0.67 \pm 0.15)(12 + \log(O/H)_{N2} - 8.6)$$
$$+(0.93 \pm 0.03)[\log L(H\alpha)_{24\ \mu m} - 42]\ [erg/s] \quad (2.16)$$

where $0.5 \leq R_{SB} \leq 88.5$, $8.1 \leq 12+\log(\mathrm{O/H})_{N2} \leq 8.7$, $40.0 \leq \log L(H\alpha)_{24\ \mu m}\ [erg/s] \leq 43.3$. The redshift range is $0.05 \leq z \leq 1.03$. Table 3 lists the results of the linear fits for L(PAH 6.2 μm) and L(PAH 7.7 μm) for both metallicity indicators. We note that the maximum threshold of $R_{SB} = 88.5$ is a result of the outliers with upper limits on the PAH luminosity; only nine objects in the SFR calibration sample have $R_{SB} > 10$. The median value of R_{SB} is 1.94 with an interquartile range of 1.01–3.48.

To calculate the Hα SFR calibrations, we substitute the SFR equation given by Kennicutt et al. into the multi-linear fit results:

$$SFR\ [M_{\odot}/yr] = 7.9 \times 10^{-42} L(H\alpha)_{24\ \mu m}\ [erg/s] \tag{2.17}$$

where the normalization factor assumes Salpeter IMF. The form of the PAH SFR calibration is then: log SFR [$M_{\odot}$/yr]= $c_0 + c_1 \times R_{SB} + c_2 \times$(12+log(O/H)$_{index}$ - 8.6) + $c_3 \times$[log $L(PAH_n)$ - 42] [erg/s], where $L(PAH_n)$ refers to either 6.2 μm or 7.7 μm PAH luminosities. The coefficients for the SFR calibrations are provided in Table 3. The results show that the SFR is linear with respect to the PAH luminosity (i.e., $c_3 \sim 1$) when corrected for starburst intensity and metallicity. We additionally tested for dependence on redshift and total infrared luminosity by including them as parameters in the multi-linear fit. However, we found that there was *no* significant dependence on either parameter ; the coefficients for both parameters were close to zero with large uncertainties. The PAH SFR calibrations highlight three main results:

1. The PAH luminosity per intrinsic Hα luminosity is increasingly deficient (or the Hα luminosity per PAH luminosity is enhanced) as R_{SB} increases or metallicity decreases.

2. The PAH SFR calibration does not depend on the total infrared luminosity.

3. There is no apparent redshift evolution in the PAH SFR calibration from the local universe out to $z \sim 1.2$.

2.5 Star formation rate density from $0 < z < 1.2$

The largest source of uncertainty in UV-based cosmic star formation rate density (SFRD) measurements arises from correcting for dust attenuation (Burgarella et al., 2005; Kobayashi et al., 2013). For example, Salim et al. (2007) show that there is significant scatter between

Table 3. Multi-linear fit results for the PAH 6.2 μm and 7.7 μm luminosities and Hα star formation rates.

y	c_0	c_1	c_2	c_3	metallicity index
log L(PAH 6.2 μm)	42.65±0.03	-0.08±0.01	0.35±0.13	1.03±0.03	N2
log SFR(PAH 6.2 μm)	-40.59±0.03	0.08±0.01	-0.34±0.13	0.97±0.03	N2
log L(PAH 6.2 μm)	42.61±0.04	-0.07±0.01	0.28±0.13	1.07±0.04	O3N2
log SFR(PAH 6.2 μm)	-38.83±0.04	0.07±0.01	-0.26±0.12	0.93±0.04	O3N2
log L(PAH 7.7 μm)	43.01±0.02	-0.02±0.003	0.67±0.15	0.93±0.03	N2
log SFR(PAH 7.7 μm)	-45.41±0.02	0.02±0.003	-0.72±0.15	1.08±0.03	N2
log L(PAH 7.7 μm)	43.15±0.04	-0.08±0.01	0.29±0.13	1.08±0.04	O3N2
log SFR(PAH 7.7 μm)	-39.00±0.04	0.07±0.01	-0.27±0.13	0.92±0.04	O3N2

Note. — Luminosity equations are in the form of y [erg/s] = c_0 + $c_1\times R_{SB}$ + $c_2\times$(12+log(O/H)$_{index}$-8.6) + $c_3\times$(log $L(H\alpha)_{24\ \mu m}$ - 42) [erg/s]. SFR equations are in the form of y [$M_\odot$/yr]= c_0 + $c_1\times R_{SB}$ + $c_2\times$(12+log(O/H)$_{index}$-8.6) + $c_3\times$log L(PAH$_n$) [erg/s], where L(PAH$_n$) refers to either 6.2 μm or 7.7 μm PAH luminosities. The gas-phase metallicity 12+log(O/H) is calculated via the N2 or O3N2 index (Pettini & Pagel 2004).

A_{FUV} and the rest-frame FUV-NUV color for their sample of ∼50,000 local, optically-selected galaxies with *GALEX* photometry. The scatter is especially prominent for starburst galaxies, which can deviate from the trend found for normal star-forming galaxies by $\gtrsim$1 mag. SFRD indicators based on IR observations are particularly invaluable towards the epoch of peak cosmic star formation when much of this activity was heavily dust-obscured. Takeuchi et al. (2007) estimate that the FIR luminosity density is approximately 15 times higher than that of the FUV at $z \sim 1$. However, studies have shown the FIR SFR to be less certain for galaxies whose UV to optical emission is dominated by old stellar populations or AGN (Kennicutt, 1998).

We apply our extinction-independent PAH 7.7 μm SFR calibrations to estimate the star formation rate density to $z \sim 1.2$ for star-forming galaxies with metallicity detections. We use the rest-frame 8 μm and 12 μm luminosity functions (LF) from Goto et al. (2010), which were derived using *AKARI*/IRC sources in the NEP-Deep field. The luminosity functions

assume a double power law given by:

$$\Phi(L)dL/L^* = \Phi^* \left(\frac{L}{L^*}\right)^{1-\alpha} dL/L^*,\ (L < L^*) \tag{2.18}$$

$$\Phi(L)dL/L^* = \Phi^* \left(\frac{L}{L^*}\right)^{1-\beta} dL/L^*,\ (L > L^*) \tag{2.19}$$

where Φ^* is the normalization in Mpc^{-3} dex^{-1}, L^* is the characteristic luminosity or "knee" of the luminosity function in L$_\odot$, L is the monochromatic luminosity νL_ν(8 μm) or νL_ν(12 μm), and α and β are the slopes of the luminosity function at the low- and high-luminosity sides. We adopt the best-fit parameters given in Table 2 of Goto et al. (2010). The luminosity density is then given as the integral:

$$\Omega = \int_{0.1L^*}^{10L^*} L\Phi(L)\, dL \tag{2.20}$$

where we define the lower and upper limits to be within an order of magnitude of L^*. We calculate the 8 μm luminosity density in redshift bins of $0.38<z<0.58$ (*S11*) and $0.65<z<0.90$ (*L15*), and the 12 μm LF in bins of $0.15<z<0.35$ (*L15*), $0.38<z<0.62$ (*L18W*), and $0.84<z<1.16$ (*L24*), where the corresponding *AKARI*/IRC filters are given in parentheses. At $0<z<0.3$, we use the 8 μm luminosity density given by Huang et al. (2007) where $\Omega_{8\mu m}$=3.1×10^7 L$_\odot$ Mpc^{-3}.

We use linear fits with fixed unity slope to convert PAH luminosity to monochromatic luminosity at 8 and 12 μm, as shown in Figure 2.17. The correlations are given by:

$$\log L(PAH\ 7.7\ \mu m) = (-0.70 \pm 0.01) + \log \nu L_\nu(8\ \mu m) \tag{2.21}$$

$$\log L(PAH\ 7.7\ \mu m) = (-0.57 \pm 0.01) + \log \nu L_\nu(12\ \mu m) \tag{2.22}$$

where νL_ν(8 μm) and νL_ν(12 μm) are in erg/s. The scatter in the linear fits represented by the RMS dispersion in the residuals is approximately 0.13 and 0.18 dex for the 8 μm and 12

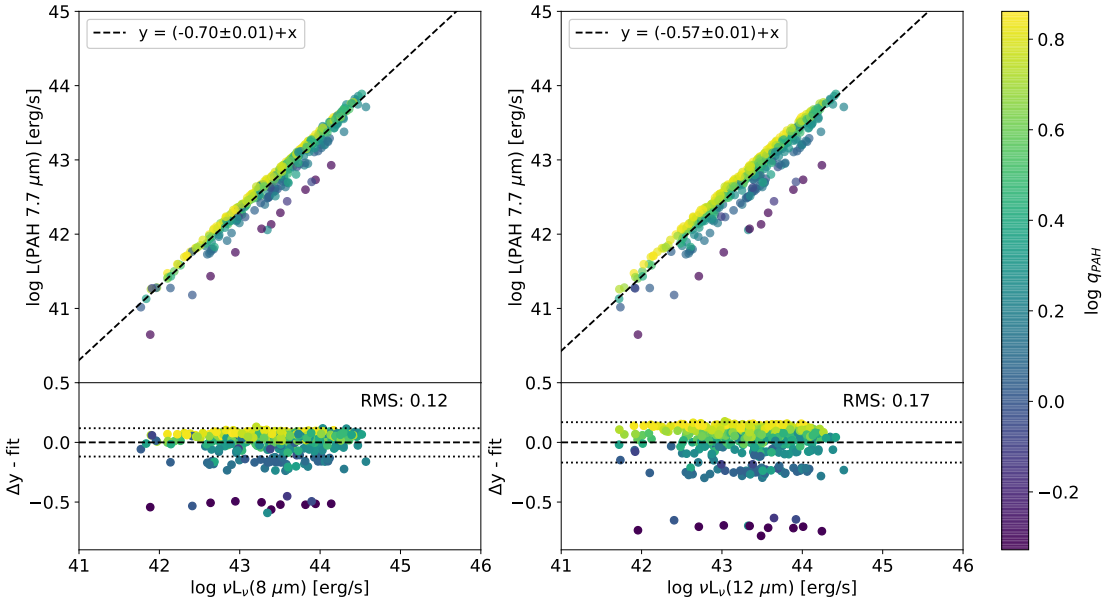

Figure 2.17 Top panels: Correlations between PAH 7.7 μm luminosity and monochromatic luminosity at 8 μm (left) and 12 μm (right) for star-forming galaxies. Dashed lines represent linear fits with fixed unity slope. Bottom panels: Residuals of the fit as a function of monochromatic luminosity with dotted lines indicating the RMS dispersion. Each galaxy is color-coded by the relative abundance of its small PAH dust grains, shown by the vertical scale on the right.

μm relations, respectively (bottom panels). The outliers with residuals $\lesssim -0.5$ are starburst galaxies with exceptionally high IR8 ($=L(TIR)/L(8\ \mu m) \gtrsim 20$) and represent only 7% of the overall starburst galaxy sample. However, as shown by the color bar, these PAH-weak outliers also have SEDs which CIGALE fitted with the minimum q_{PAH} value ($q_{PAH} \approx 0.47$), and therefore represent upper limits due to modeling constraints.

Then, we substitute equations 2.21 and 2.22 for $L(PAH\ 7.7\ \mu m)$ into our SFR calibrations to derive a function of SFR(IR8, 12+log(O/H), $\nu L_\nu(8\ \mu\text{m})$) or SFR($\text{R}_{SB}$, 12+log(O/H), $\nu L_\nu(12\ \mu\text{m})$). The SFRD ($\rho_{SFR}$) is calculated in each redshift bin as:

$$\rho_{SFR} = c_0 + c_1 \times \langle R_{SB} \rangle + c_2 \times \langle (12 + \log(\text{O/H}) - 8.6) \rangle + c_3 \times (c_4 + \Omega_{8\mu m}) \qquad (2.23)$$

Table 4. Number of star-forming galaxies integrated in each redshift bin to calculate the star formation rate density.

LF	redshift bin	N_{tot} (N_{MS}/N_{SB})			
		Hα N2	Hα O3N2	[O II] N2	[O II] O32
8 μm	$0.02<z<0.3$	203 (129/74)	131 (70/61)	120 (77/43)	98 (59/39)
8 μm	$0.28<z<0.47$	105 (51/54)	89 (38/51)	85 (46/39)	135 (66/69)
8 μm	$0.65<z<0.90$	10 (1/9)	3 (1/2)	1 (1/0)	17 (8/9)
12 μm	$0.15<z<0.35$	183 (106/77)	132 (67/65)	131 (80/51)	112 (67/45)
12 μm	$0.38<z<0.62$	30 (10/20)	29 (7/22)	23 (8/15)	120 (39/81)
12 μm	$0.84<z<1.16$	7 (1/6)	1 (0/1)	1 (0/1)	0

$$\rho_{SFR} = c_0 + c_1 \times \langle R_{SB} \rangle + c_2 \times \langle (12 + \log(\mathrm{O/H}) - 8.6) \rangle + c_3 \times (c_5 + \Omega_{12\mu m}) \tag{2.24}$$

in $\mathrm{M_\odot yr^{-1}Mpc^{-3}}$, where the constants $c_0, ..., c_3$ are given by the SFR calibrations in Table 3, c_4 and c_5 are the best-fit intercepts from equations 2.21 and 2.22, respectively. $\Omega_{8\mu m}$ and $\Omega_{12\mu m}$ are the luminosity densities in $\mathrm{L_\odot Mpc^{-3}}$ calculated from equation 2.20 based on $\nu L_\nu(8\ \mu m)$ and $\nu L_\nu(12\ \mu m)$ and converted to $\mathrm{L_\odot}$ units. The averages $\langle R_{SB} \rangle$ and $\langle 12+\log(\mathrm{O/H}) \rangle$ are averaged over each redshift bin. Table 4 shows the number of star-forming galaxies integrated in each bin for a given PAH 7.7 μm and optical emission line calibrator.

Figure 2.18 shows the redshift evolution of the PAH 7.7 μm-derived SFRD based on the Hα calibration and N2/O3N2 metallicity indicators. We calculate the SFRD for three samples in each redshift bin: (1) combined main-sequence and starburst galaxies (filled circles), (2) main-sequence galaxies only (triangle symbols), and (3) starburst galaxies only (star symbols). The redshifts plotted are the median redshifts per bin. The SFRDs derived from either the 8 μm and 12 μm LFs are consistent with each other within the uncertainties.

For reference, we plot the SFRD calculated from FUV and FIR observations from Burgarella et al. (2013) who use calibrations from Kennicutt (1998). We find that the PAH 7.7 μm star formation rate density includes significant contribution from dust-obscured star formation absorbed in the UV. At $z\sim1$, the PAH SFRD is an order of magnitude higher than

the FUV SFRD. Our results are consistent with the total (FUV+FIR) SFRD in Burgarella et al. (2013), and suggest that when corrected for metallicity and starburst intensity, the PAH 7.7 μm luminosity traces both the obscured and unobscured star formation in actively star-forming galaxies. In addition, the contribution from starburst galaxies to the SFRD becomes more significant at higher z relative to main-sequence galaxies. Our results are consistent with past attempts to estimate the SFR based on *Herschel*/PACS detections. The SFR calibration with the O3N2 index (bottom panel) predicts a higher SFRD than with the N2 index by a factor of 2.5 at $z \sim 0.15$ to a factor of 1.4 at $z \sim 0.75$.

We also show the redshift evolution for the PAH 7.7 μm-derived SFRD, based on the dereddened [O II] luminosity calibration and N2 (top panel) and O32 (bottom panel) metallicity indicators in Figure 2.19. Although more data are needed at $z \gtrsim 0.8$ to constrain the shape of the SFRD, the PAH SFRD derived from the L[O II] calibration is consistent with that of Hα.

2.6 Discussion and Conclusions

2.6.1 Comparison with previous studies

To our knowledge, this study is the first to derive PAH SFR calibrations from *AKARI*/IRC 2–24 μm photometry. We extend the relationship between PAH luminosity and SFR by exploring the dependence of the SFR calibration on metallicity and starburst intensity. Shipley et al. (2016) derived PAH SFR calibrations using a sample of *Spitzer*/IRS galaxies at z <0.4. We find that their linear fits to L(PAH) vs. L(Hα) are consistent with our results for main-sequence galaxies up to $z \sim 1.2$, but are not valid for starburst galaxies, which have systematically higher L(TIR)/L(8) ratios. This discrepancy is most likely because starburst galaxies were excluded from their sample due to having low S/N. Based on Figure 2.14, we estimate that Shipley et al.'s calibration sample is limited to main-sequence galaxies with EW(PAH 6.2 μm)$\gtrsim$1 μm and EW(PAH 7.7 μm)$\gtrsim$4 μm.

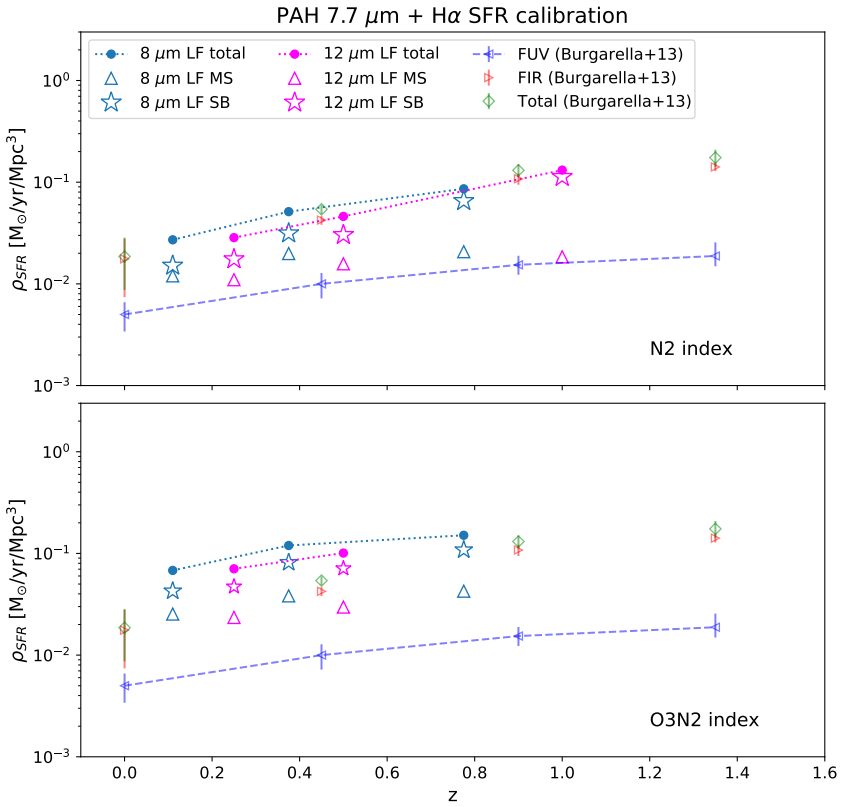

Figure 2.18 Star formation rate density as a function of redshift for the N2 (top) O3N2 (bottom) metallicity indicators, using the Hα and PAH 7.7 μm SFR calibration. Three dotted lines of different colors connect the estimates based on the 8 and 12μm and FUV luminosity functions.

Takagi et al. (2010) studied "PAH-luminous" starburst galaxies at $z \sim 0.5$ and $z \sim 1$ in the *AKARI* NEP-Deep survey that were selected using color cuts based on the 15 μm/9 μm and 11 μm/7 μm flux ratios. Applying the same color criteria to our star-forming galaxies in the NEP-Deep region, we identify 22 galaxies at $0.39<z<0.62$ ($\tilde{z}$=0.47) and 16 galaxies at $0.76<z<1.23$ ($\tilde{z}$=1.01). Figure 2.20 shows the correlation between the photometric monochromatic luminosity at 7.7 μm, $\nu L_{\nu,phot}(7.7\ \mu m)$ and $L(TIR)$, color-coded by R_{SB}. Galaxies shown by square symbols represent "PAH-selected galaxies" that satisfy Takagi et al.'s criteria. To calculate the photometric monochromatic luminosity, we scaled our peak

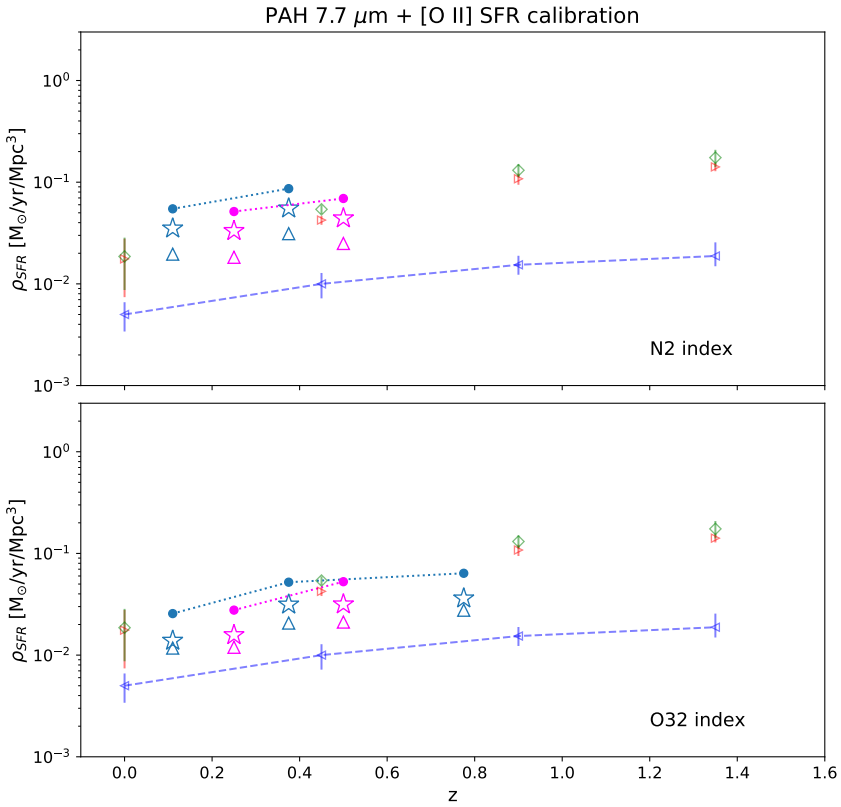

Figure 2.19 Star formation rate density as a function of redshift for the N2 (top) O32 (bottom) metallicity indicator using the [O II] and PAH 7.7 μm SFR calibration. Symbols and lines are the same as in the previous figure.

luminosity measurements by a factor of $10^{-0.24}$ (see Appendix). Most objects lie along the local relation for less luminous starbursts, suggesting that MIR-selected galaxies up to 10^{12} $L_{\odot}$ are "PAH-normal" rather than "PAH-enhanced" for a given TIR luminosity.

2.6.2 Applications with JWST

The *James Webb Space Telescope* Mid-Infrared Instrument (*JWST*/MIRI) has an observing wavelength range of 5–28 μm, which includes spectroscopy that resolves the PAH 6.2 μm and 7.7 μm features to $z \sim 2$. To apply our PAH SFR calibrations to *JWST* observations, follow-up spectroscopy in the near-IR such as with *Keck I*/MOSFIRE (Shivaei et al., 2017), would

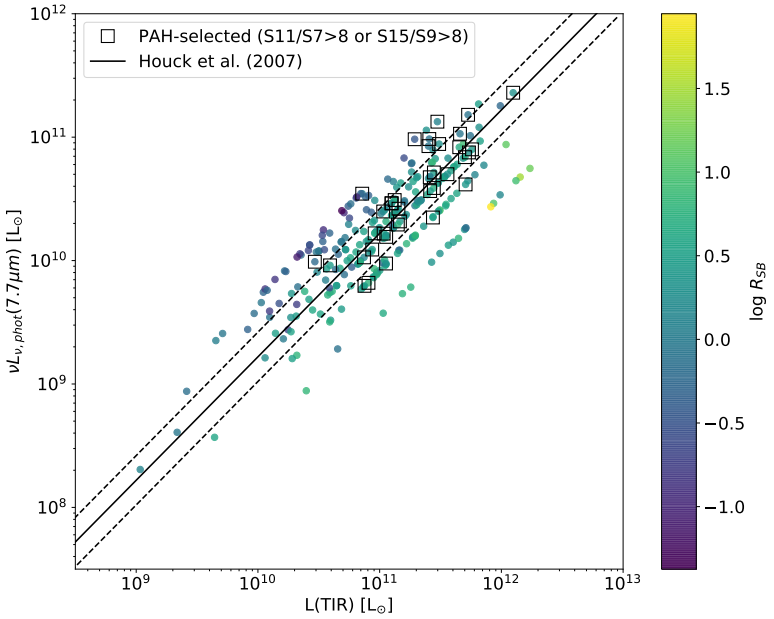

Figure 2.20 Peak photometric monochromatic PAH 7.7 μm luminosity as a function of total infrared luminosity for star-forming galaxies in the NEP-Deep region. The points in boxes meet the selection critera of "PAH enhancement" from Takagi et al. The solid line represents the relation found by Houck et al. (2007) for local starburst galaxies. Symbols are color-coded by starburst intensity.

also be useful to determine the gas metallicity. Far-infrared photometry would be needed to measure the total infrared luminosity and infer the starburst intensity/compactness of star formation, although extrapolations from multi-wavelength SED fitting may be used provided there are sufficient data in the observed optical to near-infrared wavelengths. In addition, joint observations with *Hubble Space Telescope* will be able to constrain the sSFR. PAH-based SFR calibrations that do not correct for metallicity or starburstiness would underestimate the true SFR in metal-poor and starburst galaxies.

Table 5. Updated additional secure Hα detections from *Subaru*/FMOS.

AKARI ID	RA (deg)	Dec (deg)	Redshift	F(Hα) [10^{-16} erg/s/cm^2]
61021137	269.24127	66.72676	0.949	0.34±0.13
61014814	269.13637	66.55578	1.030	0.22±0.11
61016430	269.00271	66.59490	1.003	1.45±0.27
61009352	268.98370	66.40349	0.902	0.82±0.14
61023314	268.83595	66.80321	0.925	0.78±0.23
61010363	268.77946	66.43416	0.902	0.58±0.12
61023651	268.71468	66.81580	0.715	0.68±0.09
61023133	268.64746	66.79599	0.714	0.55±0.12
61012206	268.34379	66.48484	1.026	0.63±0.22
61015448	268.91175	66.57122	1.003	1.02±0.23

2.7 Appendix

2.7.1 FMOS Hα detections

Table 5 lists the 10 additional Hα sources from Oi et al. (2017) that are newly identified as secure detections based on other emission line detections that confirm the spectroscopic redshift.

2.7.2 Measurement of total infrared luminosity

In this section, we describe our procedure for testing the dependence of our L(TIR) measurements on FIR photometry. We selected 82 star-forming galaxies from the NEP-Wide survey with one to five FIR flux density measurement(s) from *Herschel*/PACS and/or SPIRE. Then, using the same input parameters described in Table 2, we modeled SEDs using CIGALE twice – including and excluding the FIR data. Figure 2.21 shows the resulting comparison between L(TIR) when the FIR data are included and excluded. For 78% of galaxies, the L(TIR) measurements agree to within $\lesssim$ 12%. In a minority of galaxies, removing the FIR data results in significant under-estimation of the TIR luminosity. There was no correlation between the scatter and the number of FIR filter detections.

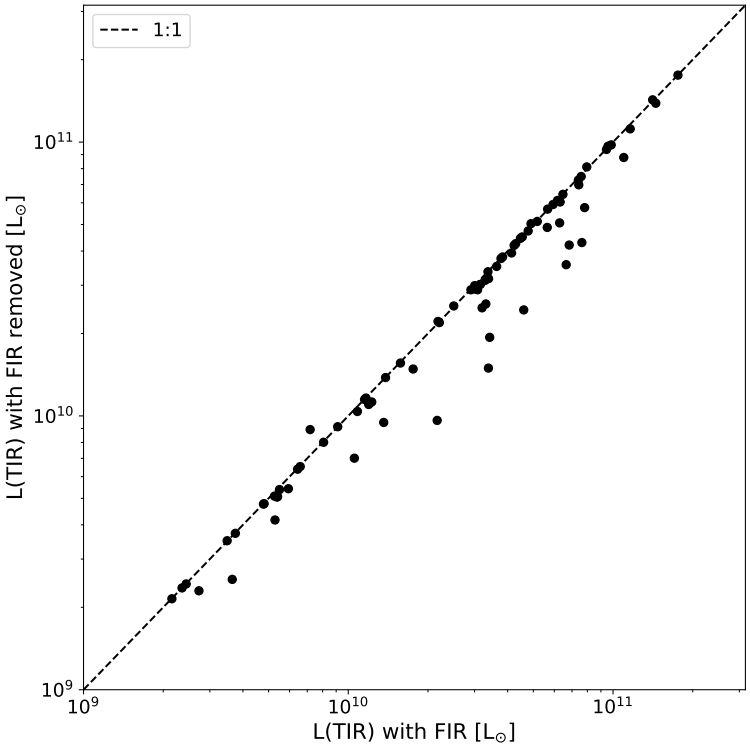

Figure 2.21 Comparison between L(TIR) measurements when including and removing *Herschel* FIR photometry in SED fitting. The dashed line represents a perfect 1:1 correlation, and has not been fitted to the data.

2.7.3 Measurement of peak PAH 7.7 μm luminosity

The PAH luminosity measurements presented in Ohyama et al. (2018) are determined by the integrated Lorentzian fits to the SPICY spectra. To compare their measurements to other works that rely on rest-frame SEDs, Ohyama et al. (2018) define the "photometric monochromatic luminosity," $\nu L_{\nu,photo}(7.7\ \mu m)$, and the "spectroscopic monochromatic luminosity," $\nu L_{\nu,spec}(7.7\ \mu m)$. Both the photometric and spectroscopic monochromatic luminosity include contributions from the underlying continuum and measure the peak PAH 7.7 μm luminosity. However, the photometric monochromatic luminosity at 7.7 μm is the peak PAH 7.7 μm luminosity based on broad-band SED fitting (Takagi et al., 2003), while the spectroscopic monochromatic luminosity is based on the SPICY spectra. According to the scaling relation in their Section 3.3.1, $\nu L_{\nu,photo}(7.7\ \mu m)$ is a factor of 0.6 dex higher

than their integrated PAH 7.7 μm luminosity due to the different luminosity definitions and continuum contribution. Based on our $L(PAH\ 7.7\ \mu m)$ measurements, $\nu L_{\nu,photo}(7.7\ \mu m)$ as measured by Ohyama et al. is ~ 0.7 dex higher than our integrated PAH 7.7 μm luminosities, which is consistent with the errors.

Figure 2.22 shows a comparison of our method for measuring the peak 7.7 μm luminosity vs. the monochromatic spectroscopic and photometric luminosities given by Ohyama et al. (2018) in 41 SPICY galaxies in our sample. We find that our peak $\nu L_{\nu}(7.7\ \mu m)$ measurements are consistent with Ohyama et al.'s spectroscopic monochromatic 7.7 μm luminosities within 13% (left panel). In contrast, there is a 0.24 dex offset between our peak $\nu L_{\nu}(7.7\ \mu m)$ measurements and the photometric monochromatic 7.7 μm luminosities (right panel), indicating that our values should be multiplied by a factor of $10^{-0.24}$ when comparing to photometric-based methods that rely on broad-band SED fitting.

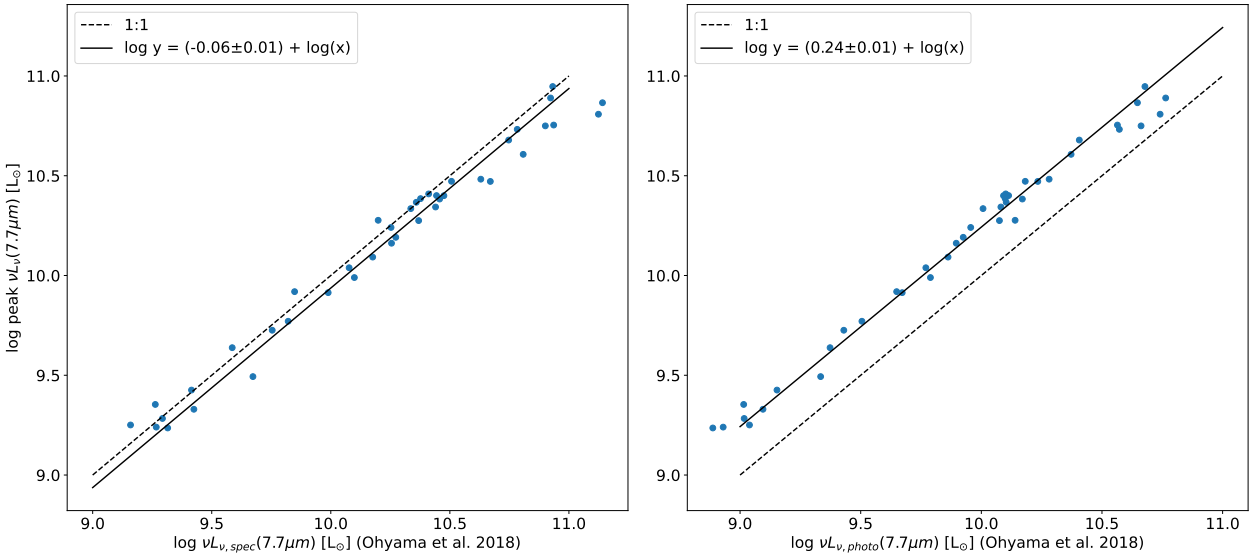

Figure 2.22 Comparison between our measured peak PAH 7.7 μm luminosity vs. spectroscopic monochromatic luminosity (left) and photometric monochromatic luminosity (right) by Ohyama et al. (2018) for SPICY galaxies. Linear fits are shown as solid lines. The dotted lines show exact agreement between the two luminosity estimates.

2.7.4 Comparison between [O II] and Hα SFR

Although the [O II] luminosity calibration from Kennicutt (1998) is commonly used as an alternative SFR diagnostic in galaxies where Hα is redshifted out of the visible range ($0.4 \lesssim z \lesssim 1.5$), the [O II] emission line is sensitive to reddening and metallicity, which can cause disagreement between SFR([O II]) and SFR(Hα) (Kewley et al., 2004). In light of these effects, we compare SFR([O II]) and SFR(Hα) in Figure 2.23, where we correct for reddening using the rest-frame 24 μm luminosity calibration given in Kennicutt (1998). For the majority of galaxies, the SFR calibrations are consistent with a 0.06 dex offset and dispersion of 20%.

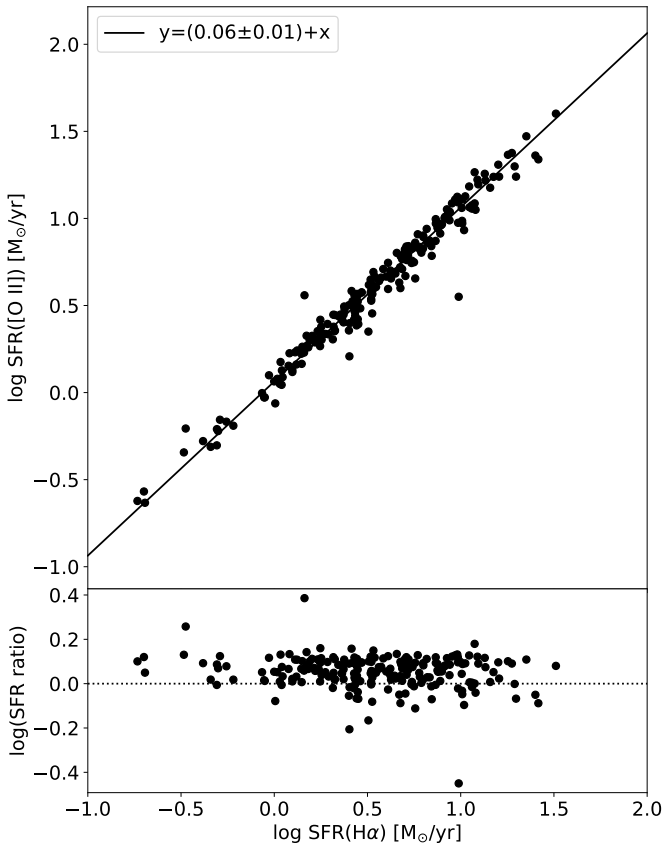

Figure 2.23 Comparison between [O II] and Hα SFR for calibration sample, dust-corrected assuming the monochromatic 24 μm luminosity correction given by Kennicutt (1998) equations. A linear fit to the data is shown by the solid line.

CHAPTER 3

The Far Infrared-Radio Correlation in Mid-Infrared-Selected Galaxies

3.1 Introduction

The far infrared-radio correlation (FIRRC) observed in star-forming galaxies establishes a fundamental connection between cool dust emission from re-radiated starlight in the far infrared and nonthermal radiation from cosmic rays emitted by supernovae that produce a synchrotron continuum ($f_\nu \propto \nu^{-0.8}$) in the radio (Helou et al., 1985; Helou & Bicay, 1993; Ivison et al., 2010). Since discovery of the FIRRC, the radio luminosity at 1.4 GHz has been proposed to be an extinction-independent SFR indicator and has been calibrated against UV, optical, and IR tracers from $0 \lesssim z \lesssim 2$ (Kennicutt et al., 2009; Boselli et al., 2015; Brown et al., 2017; Duncan et al., 2020). In this chapter, we compare star formation rate tracers based on rest-frame optical, mid-infrared, and radio emission within the *AKARI* NEP survey.

3.2 Observations and Measurements

In 2007 and 2009, the *AKARI* NEP Deep Field was observed by a two-beam mosaic with the Giant Meterwave Radio Telescope (GMRT) at 610 MHz, covering a region of 1.94 square degrees with median 5σ sensitivity of 28 μJy/beam (White et al., in prep.). We used a $3''$ search radius to select GMRT 610 MHz counterparts to *AKARI* mid-infrared sources with

secure spectroscopic redshifts. The *AKARI* spectroscopic catalog is described in Chapter 2 and includes observations from MMT/Hectospec (Shim et al., 2013), WIYN/Hydra (Shim et al., 2013), Keck/DEIMOS, and Subaru/FMOS (Oi et al., 2017). The sources for the multi-wavelength data and procedures for data reduction, flux calibration, and emission line measurements are also described in Chapter 2. We note that for measurements involving the Balmer decrement, we exclude the Shim et al. (2013) sample due to the large uncertainties in their flux calibration cited within their paper. We classify sources as star-forming galaxies or AGN candidates through the following methods, as described in Chapter 2: the BPT-[NII] diagram (Kewley et al., 2013); mid-infrared color selection, such that *AKARI*/IRC N2-N4 > 0 mag and S7-S11 > 0 mag; *Chandra* X-ray counterpart search; and/or broad permitted emission line detection (e.g., FWHM(Hα) $\gtrsim$ 1000 km/s).

For the multi-wavelength SED fits, we merged photometry from the following telescopes assuming a matching radius as the FWHM of each telescope's PSF: *GALEX* FUV and NUV (Burgarella et al., 2019), *CFHT*/MegaCam u*, g', r', i', z' (Oi et al., 2014; Hwang et al., 2007), Subaru/Hyper-Suprime Cam g/r/i/z/Y (Oi et al., 2021), *CFHT*/WIRCAM J and K_S (Oi et al., 2014), KPNO/FLAMINGOS J and H (Jeon et al., 2014), *AKARI*/IRC N2, N3, N4, S7, S9W, S11, L15, L18W, L24 (Kim et al., 2012; Murata et al., 2013), *Spitzer*/IRAC1 (3.6 μm) and IRAC2 (4.5 μm) (Nayyeri et al., 2018), *WISE* 12 μm and *WISE* 22 μm (Wright et al., 2010; Jarrett et al., 2011; Cutri et al., 2021), *Herschel*/PACS green (100 μm) and PACS red (160 μm) (Pearson et al., 2019), and *Herschel*/SPIRE 250 μm, 350 μm, 500 μm bands (Pearson et al., 2017).

We use the CIGALE software to model the SEDs (Boquien et al., 2019) with the same models and parameters as described in Chapter 2, but with an additional radio module. CIGALE models synchrotron emission by assuming the FIRRC of Helou et al. (1985), which is characterized by the radio-FIR correlation coefficient for star formation, $q_{IR,SF}$, and the slope of the synchrotron emission related to star formation, α_{SF}. The radio module includes two additional parameters to model radio-loud AGN: the "radio-loudness" parameter de-

Table 5. Radio module input parameters for CIGALE SED fits.

Parameter	Description	Value
$q_{IR,SF}$	radio-FIR coefficient (Helou et al., 1985)	2.3, 2.5, 2.7, 2.9
α_{SF}	power-law slope for star formation: $L_\nu \propto \nu^{-\alpha_{SF}}$	0.8
R_{AGN}	radio-loudness parameter for AGN	10
α_{AGN}	power-law slope for AGN emission: $L_\nu \propto \nu^{-\alpha_{AGN}}$	0.7

fined as $R_{AGN} = L_\nu(5\ GHz)/L_\nu(2500\ \text{Å})$, where $L_\nu(2500\ \text{Å})$ is the intrinsic accretion disk luminosity of the AGN measured at a viewing angle of 30°, and the power-law slope of the AGN radio emission, α_{AGN}, which is assumed to be isotropic. Table 5 summarizes our input radio parameters.

We define the AGN fraction, $frac_{AGN}$, as the ratio of the AGN-heated dust "torus" luminosity to the total luminosity integrated from rest-frame 8-1000 μm. For AGN candidates that were identified with at least one of the methods and 22 objects with unknown classification that could not be identified as either galaxies or AGN due to incomplete emission line/photometric detections, we allowed the AGN fraction to vary. Objects with unknown classification and $frac_{AGN} > 0.1$ are subsequently identified as AGN. Objects with unknown classification and $frac_{AGN} < 0.1$ are excluded from the sample to avoid potential contamination by weak or marginal AGN. The sample includes 101 galaxies and 66 AGN (including three AGN initially classified as unknown) with reduced $\chi^2 < 10$ in the best-fit SEDs. An example best-fit SED of a typical star-forming galaxy is shown in Figure 3.1.

We classify galaxies on the main sequence according to Elbaz et al. (2011), who define main-sequence galaxies as having a specific star formation rate such that $13 \times t_{cosmic}^{-2.2} \leq$ sSFR [1/Gyr] $\leq 52 \times t_{cosmic}^{-2.2}$, where t_{cosmic} is the cosmic time elapsed since the Big Bang in Gyr. Quenched galaxies and starburst galaxies are defined as galaxies that lie significantly below and above the main sequence, respectively. Our sample of star-forming galaxies consists of 91 main-sequence and starburst galaxies at $0.05 < z < 1.17$ with ranges in stellar mass and

total IR luminosity covering $10^{9.2} < M_*/\mathrm{M}_\odot < 10^{11.4}$ and $10^{9.4} < L(TIR)/\mathrm{L}_\odot < 10^{12.2}$.

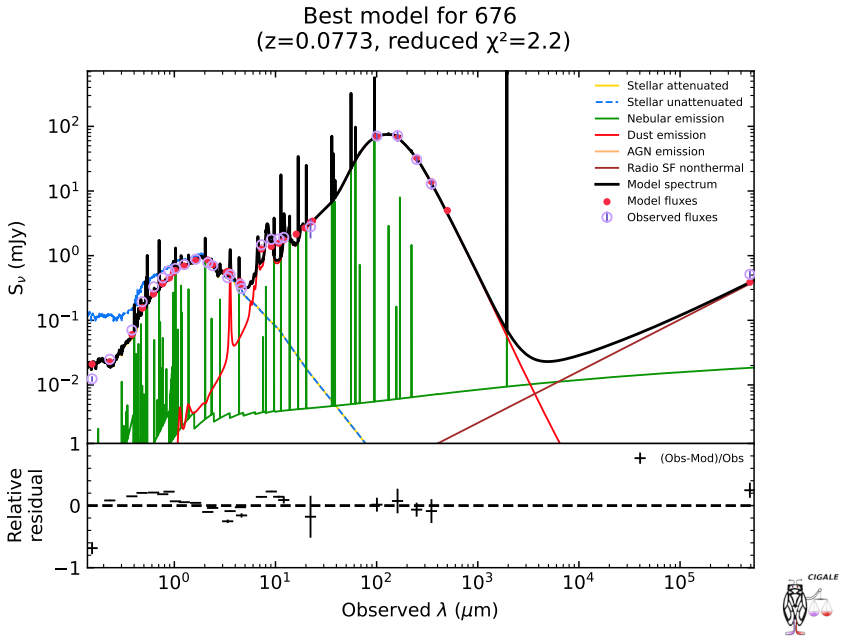

Figure 3.1 Example CIGALE best-fit SED of a typical star-forming galaxy with GMRT 610 MHz detection.

Assuming that the radio continuum follows a power law, we extrapolate the rest-frame luminosity density at 1.4 GHz based on the GRMT 610 MHz flux density as follows:

$$L_\nu(1.4\ GHz) = 4\pi D_L^2 (1+z)^{-(1-\alpha)} \left(\frac{1.4\ GHz}{0.61\ GHz}\right)^{-\alpha} F_\nu(610\ MHz) \tag{3.1}$$

where D_L is the luminosity distance z is the spectroscopic redshift, and we assume the canonical spectral index of $\alpha = 0.8$. To calculate the total IR luminosity, we integrate the CIGALE best-fit model from rest-frame 3-1100 μm to be consistent with Kennicutt et al. (2009).

3.3 The Far-Infrared Radio Correlation

In Figure 3.2 we show the radio to total infrared luminosity correlation for main-sequence and starburst galaxies in our sample. A linear fit to the log/log relation is given by:

$$log\ L_{\nu}(1.4\ GHz)\ [W/Hz] = (10.98 \pm 0.43) + (1.07 \pm 0.04) log\ L(3 - 1100\ \mu m)\ [L_{\odot}] \quad (3.2)$$

where $L_{\nu}(1.4\ GHz)$ is given by equation 3.1. Quenched galaxies and AGN are excluded from the linear fit but are shown for reference as unfilled black circle and red square symbols, respectively. Our derived correlation is roughly linear and consistent with the local relations within the uncertainties (e.g., Bell, 2003; Kennicutt et al., 2009). We also find that the ~ 0.5 dex offset in AGN is consistent with the relation found for Seyfert galaxies (e.g., Rush et al., 1996). We note that the ~ 0.2 dex offset between our fit and the local relations may be due to our sample being limited to GMRT detections only. Upper limits would need to be included in order to minimize the effects of Malmquist bias.

3.4 Calibration of Radio Luminosity and Hα SFR

Empirical relations between the 1.4 GHz luminosity and dust-corrected Hα luminosity have been used to calibrate SFR for radio sources (Bell, 2003; Kennicutt et al., 2009; Boselli et al., 2015; Brown et al., 2017; Gürkan et al., 2018; Duncan et al., 2020). We calculate the 24 μm-corrected Hα luminosity according to the Calzetti et al. (2010) relation:

$$L(H\alpha,\ 24\ \mu m) = L(H\alpha,\ obs) + a \times \nu L_{\nu}(24\ \mu m) \quad (3.3)$$

where $a = 0.02$ for $\nu L_{\nu}(24\ \mu m) < 10^{42}$ erg/s and $a = 0.031$ for $\nu L_{\nu}(24\ \mu m) > 10^{42}$ erg/s. In Figure 3.3, we compare Hα luminosities corrected with the 24 μm correction and Balmer decrement (a). Panels (b) and (c) show the 1.4 GHz luminosity against the Balmer-

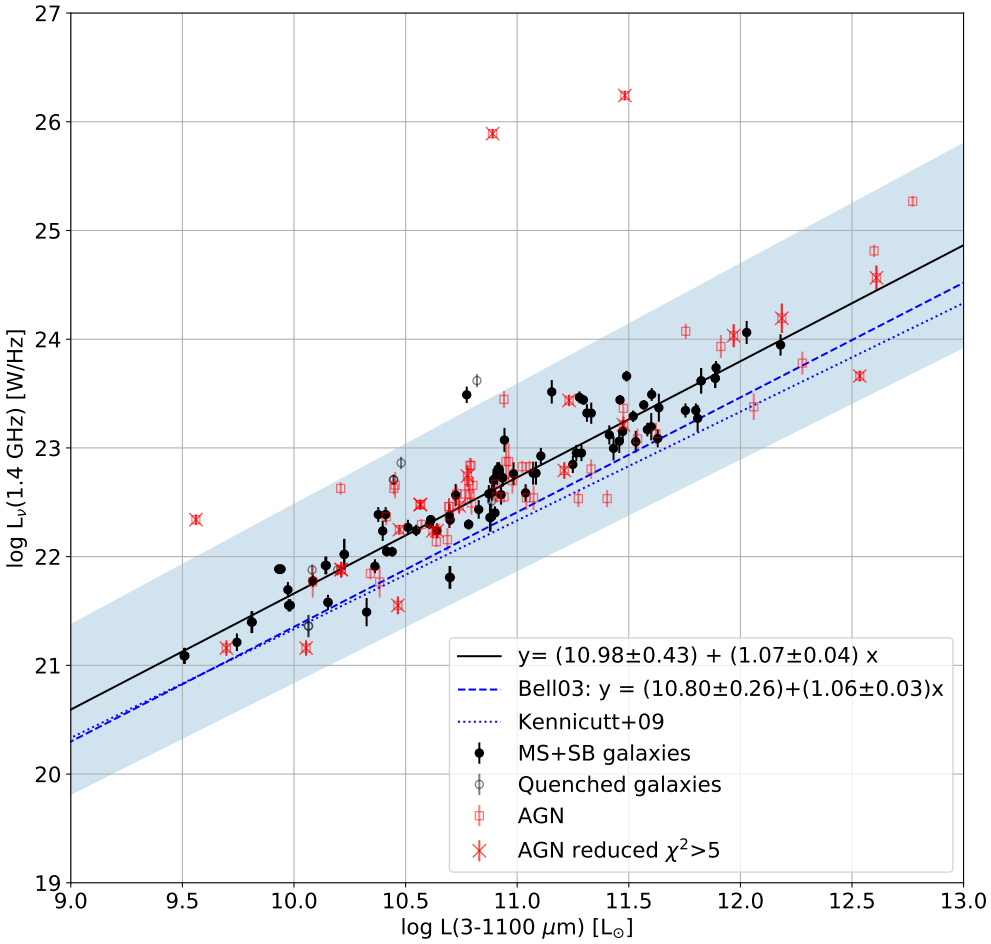

Figure 3.2 Radio-total infrared luminosity correlation for star-forming galaxies with GMRT 610 MHz detections. The solid line shows the linear fit to main-sequence and starburst galaxies.

decrement-corrected Hα luminosity and 24 μm-corrected Hα luminosity, respectively. For galaxies with one to two magnitudes of attenuation in Hα, the dust-corrected Hα luminosities are consistent with the local relation given by Boselli et al. (2015) (dotted line). The 1.4 GHz luminosity correlates more tightly with the 24 μm-corrected Hα luminosity than with the Balmer decrement-corrected Hα luminosity. Boselli et al. (2015) attribute the increased scatter in the Balmer decrement correction to objects with weak Balmer emission and domi-

nant stellar absorption. However, we do not observe increased scatter for objects with weak Balmer emission (i.e., rest-frame Hβ equivalent width < 10 Å).

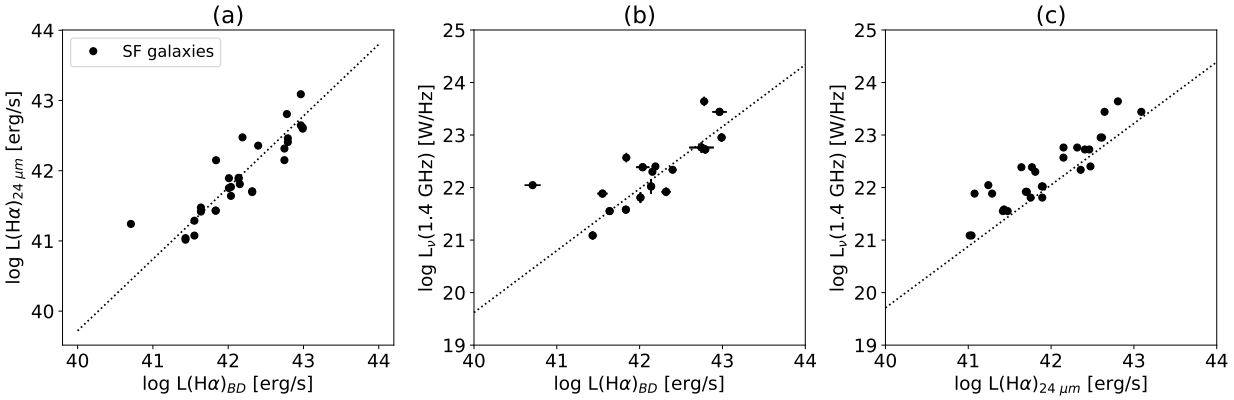

Figure 3.3 Comparisons between 24 μm-corrected Hα luminosity and Balmer decrement-corrected Hα luminosity (a) and radio luminosity vs. dust-corrected Hα luminosity (b) and (c). The dotted line in each panel shows relations given by Boselli et al. (2015).

We calculate SFRs based on the Balmer decrement-corrected Hα luminosity by using the relation given by Hao et al. (2011):

$$SFR(H\alpha)_{BD}\ [M_{\odot}/yr] = 10^{-41.257} L(H\alpha)_{BD}\ [erg/s] \tag{3.4}$$

which assumes a Kroupa (2001) IMF. Figure 3.4 shows the radio luminosity as a function of dust-corrected Hα SFR. Our galaxies included in this figure have a redshift range of $0.051 < z < 0.768$ with median $z = 0.151$. We find that our results are consistent with the SFR-radio relations at $z \sim 0$, with little evolution observed from $z = 0$ to $z \sim 2$.

3.5 Comparison between Radio and PAH SFRs

To compare our radio SFR estimate with our PAH 7.7 μm-derived SFRs, we limit our sample of star-forming galaxies to those with at least four photometric detections in the mid-infrared (7-24 μm), metallicity measurements based on the N2 indicator, and N2<-0.3. The resulting PAH-radio SFR sample consists of 29 objects. We calculate the 1.4 GHz SFR by substituting

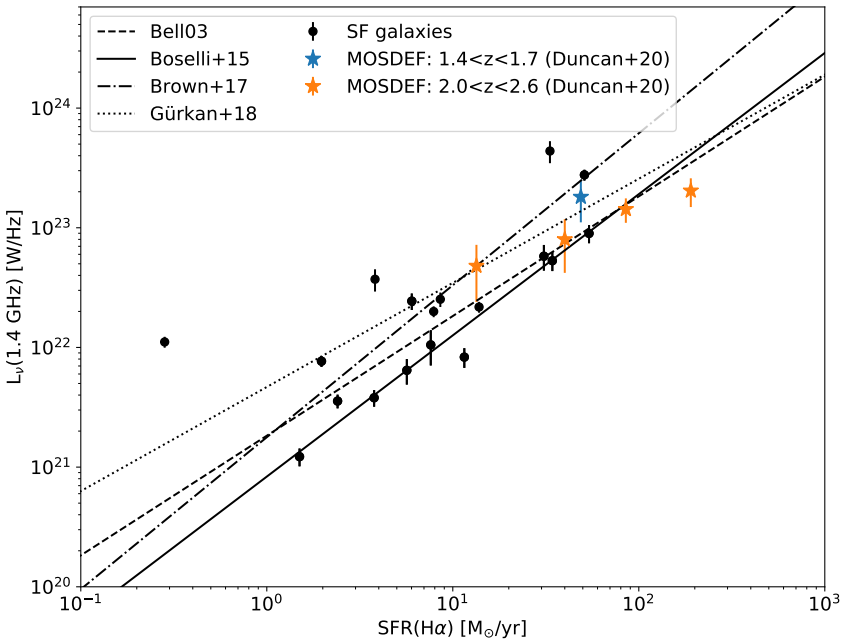

Figure 3.4 SFR-radio correlation for star-forming galaxies (black dot symbols). Star symbols correspond to median stacked radio luminosity densities for bins of dust-corrected Hα SFR from the MOSDEF survey (Duncan et al., 2020).

the Kennicutt (1998) relation (Equation 2.17) into the Boselli et al. (2015) relation given by:

$$\log_{10}\left(\frac{L_\nu(1.4\text{ GHz})}{\text{W/Hz}}\right) = 1.17 \times \log_{10} L(H\alpha)_{24\ \mu m} - 27.09 \tag{3.5}$$

where $L(H\alpha)$ is the 24 μm dust-corrected Hα luminosity. SFR(PAH 7.7 μm) is calculated based on our calibration given by Equation 2.16. Figure 3.5 compares the 1.4 GHz SFR to the PAH 7.7 μm SFR. We find that the 1.4 GHz luminosity overestimates the SFR relative to PAH 7.7 μm emission by a factor of ~ 0.3 dex. This discrepancy may suggest that the radio continuum luminosity is contaminated by non-stellar sources, or that L_ν(1.4 GHz) is overestimated when extrapolated from the 610 MHz luminosity due to Malmquist bias.

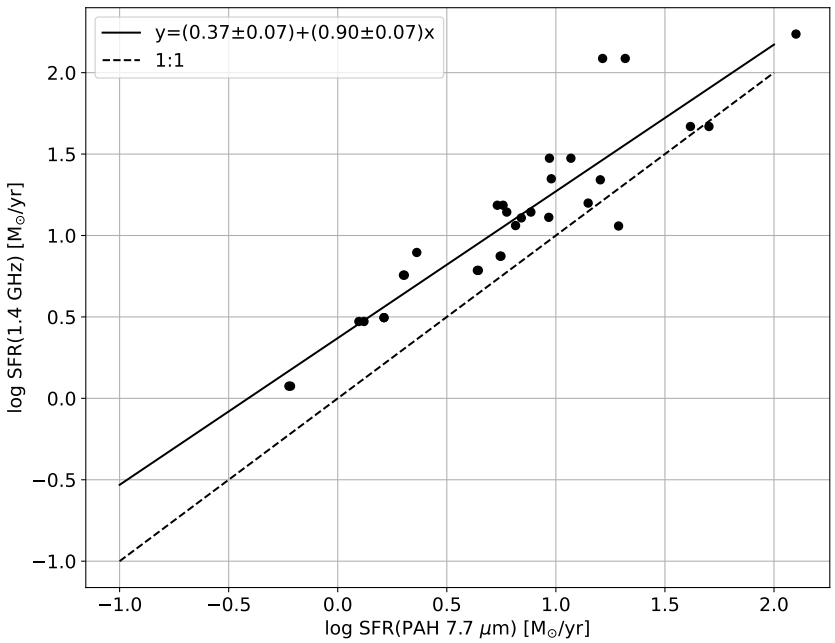

Figure 3.5 Comparison between star formation rates derived from radio luminosity density and PAH 7.7 μm luminosity.

CHAPTER 4

Photometric Search for Silicate Absorption in Dust-Obscured AGN

4.1 Introduction

One of the main science goals for the *AKARI* mission has been to study the co-evolution of dust-obscured AGN and their host galaxies at all wavelengths. For galaxies that host an active galactic nucleus, the energy output in the mid-infrared is dominated by two main processes: warm dust emission heated by stellar radiation and hot dust emission heated by the AGN which produces a quasi-power-law thermal continuum. X-ray observations are efficient for detecting AGN, with more than half of the X-ray sources detected by *Chandra* ultra-deep field imaging in the NEP Deep field identified as *AKARI* mid-infrared counterparts (Krumpe et al., 2015). However, more than a third of the AGN selected using *AKARI*/IRC 7–24 μm photometry are obscured in the X-rays by intervening dust and gas. Stacking analysis of *Chandra* observations for these dust-obscured AGN has revealed a Fe Kα emission line, which confirms that these are Compton-thick AGN (Krumpe et al., 2015; Miyaji et al., 2017).

Dust-obscured, or Type 2, AGN exhibit a silicate absorption feature centered at 9.7 μm due to the Si-O bending modes. Studies of IR-luminous *Spitzer*/IRS galaxies have demonstrated that the strength of this silicate absorption feature, characterized by optical depth $\tau_{9.7}$, is inversely associated with the PAH dust emission equivalent widths at 6.2 – 11.3 μm (García-Bernete et al., 2022). The diagnostic diagram presented in Spoon et al. (2007)

shows an anti-correlation between silicate absorption strength and EW(PAH 6.2 μm) for dust-obscured objects. The presence of weak silicate absorption in PAH-luminous galaxies can lead to uncertainties in equivalent width measurements of the surrounding PAH dust emission at 7.7 μm, 8.6 μm and 11.3 μm, due to difficulties in constraining the mid-IR continuum (Smith et al., 2007). Most of the published studies have used *Spitzer*/IRS spectroscopy to study the effects of silicate absorption on PAH emission. This tends to limit samples to low-redshift objects or ULIRGs at $z \sim 2$ (e.g., Yan et al., 2005). As discussed in Chapter 2, the continuous wavelength coverage from 2–24 μm of *AKARI* provides a unique opportunity to study statistically significant samples of dust-obscured objects. In this chapter, we present our methodology for selecting extremely dust-obscured AGN candidates based on *AKARI* mid-IR photometry.

4.2 Methodology

The 9.7 μm silicate absorption feature is centered within the *AKARI* 11 μm filter (and *WISE* 12 μm filter) at $0.15 \lesssim z \lesssim 0.25$, and within the *AKARI* 15 μm filter at $0.4 \lesssim z \lesssim 0.5$. We searched our catalog of CIGALE best-fit SEDs for silicate absorption candidates in Type 2 AGN, by selecting objects with $frac_{AGN} > 0$, $\tau_{9.7} > 1$, and orientation angle $\psi \sim 0^{\circ}$ within these redshift bins. AGN candidates were drawn from the sample described in Chapter 2 and selected via the BPT-[NII] emission line ratio diagram (Kewley et al., 2013), mid-infrared *AKARI* colors, and *Chandra* X-ray observations (Krumpe et al., 2015). The full set of input SED parameters is described in Table 2 of Chapter 2. In addition, we selected star-forming galaxies with $frac_{AGN} = 0$ for each redshift bin as our comparison sample. We required photometric detections in the *AKARI* S9W, S11, and L15 filters for galaxies at $0.15 \lesssim z \lesssim 0.25$, and detections in the *AKARI* S11, L15, and L18W filters at $0.4 \lesssim z \lesssim 0.5$. This selection resulted in nine AGN and 146 star-forming galaxy candidates for the $z \sim 0.2$ bin, and 25 AGN and 78 star-forming galaxy candidates for the $z \sim 0.45$ bin. Figure 4.1

shows two individual SEDs of Type 2 AGN with moderate to strong silicate absorption as determined by SED fitting. In panel (a), the silicate absorption feature is centered within the *WISE* 12 μm filter ($\tau_{9.7}$=3.2±2.5), and in panel (b), the feature is centered within the *AKARI* 15 μm filter ($\tau_{9.7}$= 6.0±0.2).

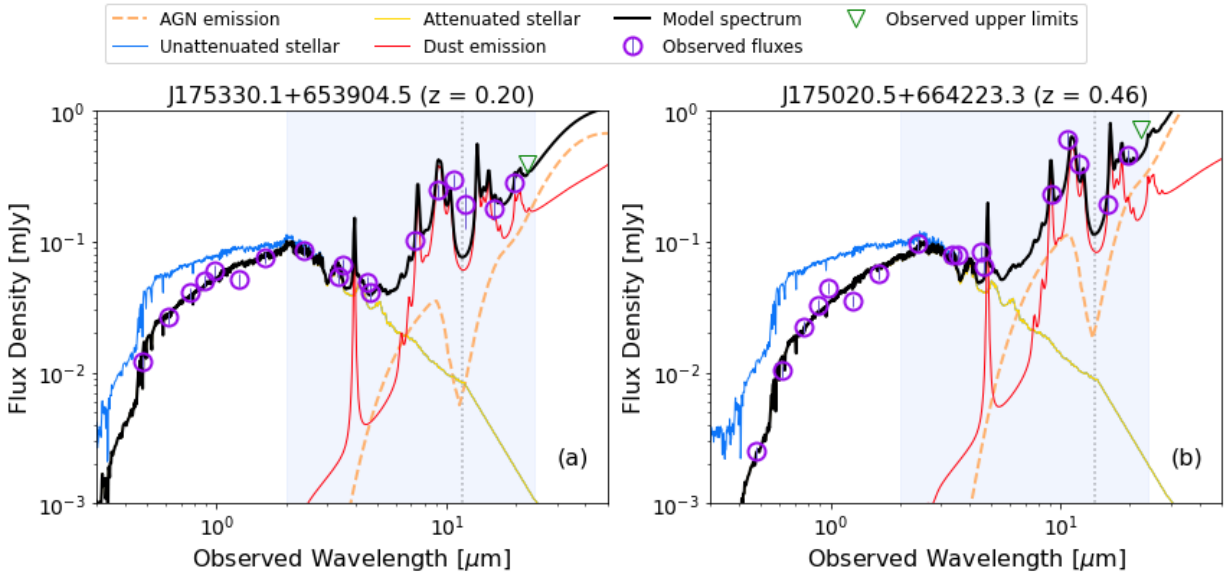

Figure 4.1 Example CIGALE best-fit SEDs for two Type 2 AGN with deep silicate absorption. The light blue region from 2-24 μm highlights the wavelength range covered by *AKARI*/IRC. The faint, vertical dotted line marks the observed wavelength for the silicate absorption feature at rest-frame 9.7 μm. The dashed orange line shows the model for AGN emission, the red line shows the galactic dust emission, and the yellow line shows the starlight. The sum of these 3 components yields the black line fit to the observed data points, shown in purple.

For each redshift bin, we shift the best-fit SEDs to the rest-frame and calculate the average spectrum and observed flux densities in each filter. Figure 4.2 shows the average best-fit spectrum over the silicate absorption candidates (Type 2 AGN, top row) and star-forming galaxies with $frac_{AGN} = 0$ (bottom row). The arithmetic mean of the flux densities are shown as square symbols. For reference, we overplot the filter transmission curves. Considering that the wavelength coverage of the S11 and L15 filters overlaps with the red and blue sides of the neighboring filters, further work would be needed to disentangle the silicate absorption fraction to the mean flux density. However, our preliminary results suggest

that the ratio of the mean flux densities $\overline{f_\nu}(S11)/\overline{f_\nu}(L15)$ and $\overline{f_\nu}(L15)/\overline{f_\nu}(L18W)$ are significantly reduced for the Type 2 AGN sample with silicate absorption relative to those of the star-forming samples. For the AGN sample, $\overline{f_\nu}(S11)/\overline{f_\nu}(L15) = 1.00$ ($z \sim 0.2$) and $\overline{f_\nu}(L15)/\overline{f_\nu}(L18W) = 0.88$ ($z \sim 0.45$). For the star-forming sample, $\overline{f_\nu}(S11)/\overline{f_\nu}(L15) = 1.46$ ($z \sim 0.2$) and $\overline{f_\nu}(L15)/\overline{f_\nu}(L18W) = 1.10$ ($z \sim 0.45$). Given that we additionally identify 28 Type 2 AGN with weak to no silicate absorption predicted by CIGALE, we roughly estimate that 25/53 or 47% of the Type 2 AGN detected at $z \sim 0.45$ have strong enough silicate absorption to be detected in our *AKARI*/IRC mid-IR multi-band photometry.

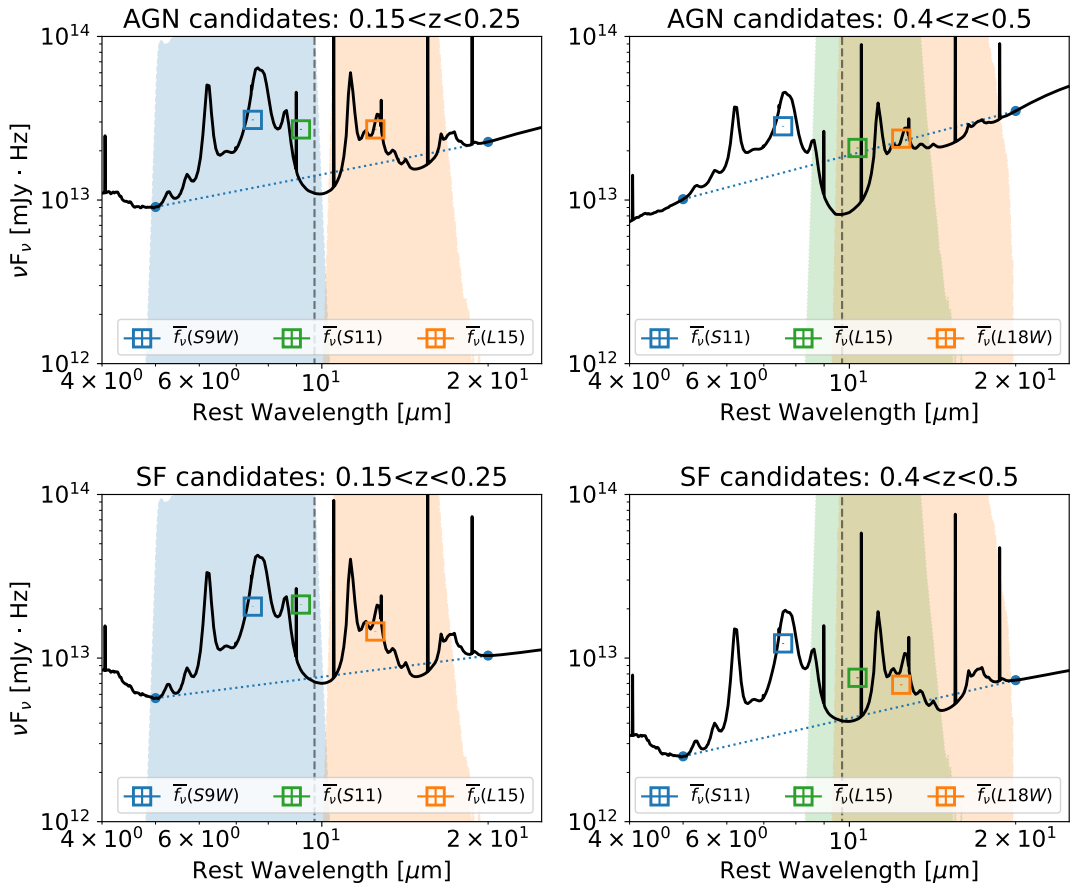

Figure 4.2 Average best-fit CIGALE SEDs for Type 2 AGN candidates with silicate absorption (top row) and star-forming galaxies (bottom row). Shaded regions represent the transmission curves of each filter, colored according to their respective flux densities. The faint, vertical dotted line marks the silicate absorption feature at rest-frame 9.7 μm.

CHAPTER 5

Conclusions and Future Directions

In this thesis, we explore PAH dust emission as an extinction-independent star formation rate indicator, a major scientific goal of the *AKARI* mission. We combine ground-based, optical and near-infrared spectroscopy with *AKARI*/Infrared Camera multi-band photometry to measure the infrared spectra of ∼500 galaxies in the *AKARI* NEP field. We present the first results of PAH 6.2 and 7.7 μm SFR calibrations with corrections for metallicity and starburst intensity. Our calibration sample consists of 443 main-sequence and starburst galaxies from the *AKARI*/IRC NEP survey at $0.05 \leq z \leq 1.03$, with a broad range of stellar masses ($M_* \sim 10^{8.7} - 10^{11.2}\ M_\odot$), total infrared luminosities ($L(TIR) \sim 10^{8.7} - 10^{12}\ L_\odot$), and SFRs ($\sim 0.06 - 500\ M_\odot \mathrm{yr}^{-1}$). These mid-infrared-selected galaxies were observed to have strong emission lines with optical/NIR spectroscopy, including *Keck II*/DEIMOS and *Keck I*/MOSFIRE observations, which we newly presented in this work. A summary of our main conclusions are as follows:

- To measure the PAH luminosity of AKARI/IRC galaxies, we first derive best-fit spectral energy distributions with CIGALE to model the mid-IR dust emission. Then from the best-fit, rest-frame SEDs, we decompose the PAH emission features by using PAHFIT. Our photometrically derived PAH 6.2 and 7.7 μm luminosities are consistent with *AKARI*/IRC slitless spectroscopic measurements to within 20-40%.

- The PAH luminosity per dust-corrected Hα and [O II]$\lambda\lambda$3726, 3729 luminosity increases as a function of metallicity, and decreases as a function of starburst intensity (R_{SB}) and AGN fraction. Starburst galaxies (i.e., galaxies with $R_{SB} > 2$) are systematically

deficient in $L(PAH)$ per dust-corrected $L(H\alpha)$ and $L([O\ II])$ relative to main-sequence galaxies by a factor of 0.34 and 0.3 dex, respectively. Based on multi-linear fits, we derive, for the first time, corrections for metallicity and starburst intensity to the PAH luminosity and SFR. In addition, we find that the PAH SFR calibration is independent of total infrared luminosity and redshift (at least up to $z \sim 1$).

- We apply our PAH SFR calibrations to the extensive dataset of *AKARI* to study the dust-obscured cosmic star formation rate density per comoving volume. We combine our correlations between $L(PAH\ 7.7\ \mu m)$ vs. $\nu L_\nu(8\ \mu m)$ and $\nu L_\nu(12\ \mu m)$ with luminosity functions at 8 and 12 μm to derive the SFRD as a function of PAH luminosity. The SFRD as predicted by our PAH 7.7 μm SFR calibration is a factor of 2 higher at $z \sim 0.15$ and a factor of 6.5 higher at $z \sim 1$ than observed FUV estimates due to dust attenuation, with significant contribution from starburst galaxies at $z \gtrsim 0.6$.

- Future studies that involve PAH luminosity as a SFR indicator, such as those conducted with *JWST*, would need to correct for the effects of metallicity and starburst intensity; otherwise, the PAH SFR would be underestimated in metal-poor or starburst galaxies.

- We extend our study of PAH as a SFR indicator to the radio regime and investigate whether the far infrared-radio correlation evolves with cosmic time by selecting *AKARI* mid-infrared galaxies with GMRT 610 MHz detections. For 91 star-forming galaxies with GMRT 610 MHz detections ($0.05 < z < 1.17$), we extrapolate the 1.4 GHz luminosity from best-fit multiwavelength SEDs by assuming that the radio emission follows a power law ($f_\nu \propto \nu^{-\alpha}$). We find that the correlation between $L_\nu(1.4\ GHz)$ and $L(3-1100\ \mu m)$ of our mid-infrared-selected galaxies is consistent with local relations. In addition, $L_\nu(1.4\ GHz)$ as a function of the Balmer decrement-corrected Hα SFR does not significantly evolve with redshift ($0 \lesssim z \lesssim 2$).

- The 1.4 GHz SFR is $\sim$ 0.3 dex higher than the PAH SFR. However, further work involving GMRT 610 MHz upper limits is needed to determine whether this discrepancy

is due to Malmquist bias or due to a systematic offset between the PAH SFR and the Balmer decrement-corrected Hα SFR.

- Lastly, we present a photometric-based search for 9.7 μm silicate absorption in Type 2 AGN at $z \sim 0.2$ and $z \sim 0.45$, corresponding to the *AKARI*/IRC S11 and L15 filters, respectively. By assuming that star-forming galaxies simply lack silicate absorption in the multiwavelength SED models, we find that the Type 2 AGN candidates have systematically lower $\overline{f_\nu}(S11)/\overline{f_\nu}(L15)$ at $z \sim 0.2$ and $\overline{f_\nu}(L15)/\overline{f_\nu}(L18W)$ at $z \sim 0.45$ relative to the star-forming control sample. Our SED models predict significant silicate absorption at 9.7 μm (i.e., $\tau_{9.7} \gtrsim 3$) in 47% of the Type 2 AGN detected at $z \sim 0.45$. Our procedure for modeling silicate absorption in AGN with *AKARI*/IRC mid-infrared photometry presents a promising method for inferring the orientation angle of AGN.

Bibliography

Asplund, M., Grevesse, N., Sauval, A. J., & Scott, P. 2009, ARA&A, 47, 481

Bakes, E. L. O., Tielens, A. G. G. M., & Bauschlicher, Charles W., J. 2001, ApJ, 556, 501

Bell, E. F. 2003, ApJ, 586, 794

Boquien, M., Burgarella, D., Roehlly, Y., Buat, V., Ciesla, L., Corre, D., Inoue, A. K., & Salas, H. 2019, A&A, 622, A103

Boselli, A., Fossati, M., Gavazzi, G., Ciesla, L., Buat, V., Boissier, S., & Hughes, T. M. 2015, A&A, 579, A102

Brandl, B. R., Bernard-Salas, J., Spoon, H. W. W., Devost, D., Sloan, G. C., Guilles, S., Wu, Y., Houck, J. R., Weedman, D. W., Armus, L., Appleton, P. N., Soifer, B. T., Charmandaris, V., Hao, L., Higdon, J. A., Marshall, S. J., & Herter, T. L. 2006, ApJ, 653, 1129

Brown, M. J. I., Moustakas, J., Kennicutt, R. C., Bonne, N. J., Intema, H. T., de Gasperin, F., Boquien, M., Jarrett, T. H., Cluver, M. E., Smith, J. D. T., da Cunha, E., Imanishi, M., Armus, L., Brandl, B. R., & Peek, J. E. G. 2017, ApJ, 847, 136

Buat, V., Iglesias-Páramo, J., Seibert, M., Burgarella, D., Charlot, S., Martin, D. C., Xu, C. K., Heckman, T. M., Boissier, S., Boselli, A., Barlow, T., Bianchi, L., Byun, Y. I., Donas, J., Forster, K., Friedman, P. G., Jelinski, P., Lee, Y. W., Madore, B. F., Malina, R., Milliard, B., Morissey, P., Neff, S., Rich, M., Schiminovitch, D., Siegmund, O., Small, T., Szalay, A. S., Welsh, B., & Wyder, T. K. 2005, ApJ, 619, L51

Buat, V., Marcillac, D., Burgarella, D., Le Floc'h, E., Takeuchi, T. T., Iglesias-Paràmo, J., & Xu, C. K. 2007, A&A, 469, 19

Burgarella, D., Buat, V., Gruppioni, C., Cucciati, O., Heinis, S., Berta, S., Béthermin, M., Bock, J., Cooray, A., Dunlop, J. S., Farrah, D., Franceschini, A., Le Floc'h, E., Lutz, D., Magnelli, B., Nordon, R., Oliver, S. J., Page, M. J., Popesso, P., Pozzi, F., Riguccini, L., Vaccari, M., & Viero, M. 2013, A&A, 554, A70

Burgarella, D., Buat, V., & Iglesias-Páramo, J. 2005, MNRAS, 360, 1413

Burgarella, D., Mazyed, F., Oi, N., Goto, T., Buat, V., Malkan, M., Lee, H. M., Matsuhara, H., Pearson, C., Serjeant, S., White, G. J., & Barrufet de Soto, L. 2019, PASJ, 71, 12

Calzetti, D. in , Secular Evolution of Galaxies, ed. J. Falcón-BarrosoJ. H. Knapen, 419

Calzetti, D., Armus, L., Bohlin, R. C., Kinney, A. L., Koornneef, J., & Storchi-Bergmann, T. 2000, ApJ, 533, 682

Calzetti, D., Wu, S. Y., Hong, S., Kennicutt, R. C., Lee, J. C., Dale, D. A., Engelbracht, C. W., van Zee, L., Draine, B. T., Hao, C. N., Gordon, K. D., Moustakas, J., Murphy, E. J., Regan, M., Begum, A., Block, M., Dalcanton, J., Funes, J., Gil de Paz, A., Johnson, B., Sakai, S., Skillman, E., Walter, F., Weisz, D., Williams, B., & Wu, Y. 2010, ApJ, 714, 1256

Chabrier, G. 2003, PASP, 115, 763

Cooper, M. C., Newman, J. A., Davis, M., Finkbeiner, D. P., & Gerke, B. F. 2012, spec2d: DEEP2 DEIMOS Spectral Pipeline, Astrophysics Source Code Library, record ascl:1203.003

Cutri, R. M., Wright, E. L., Conrow, T., Fowler, J. W., Eisenhardt, P. R. M., Grillmair, C., Kirkpatrick, J. D., Masci, F., McCallon, H. L., Wheelock, S. L., Fajardo-Acosta, S., Yan, L., Benford, D., Harbut, M., Jarrett, T., Lake, S., Leisawitz, D., Ressler, M. E., Stanford, S. A., Tsai, C. W., Liu, F., Helou, G., Mainzer, A., Gettngs, D., Gonzalez, A., Hoffman,

D., Marsh, K. A., Padgett, D., Skrutskie, M. F., Beck, R., Papin, M., & Wittman, M. 2021, VizieR Online Data Catalog, II/328

Desai, V., Armus, L., Spoon, H. W. W., Charmandaris, V., Bernard-Salas, J., Brandl, B. R., Farrah, D., Soifer, B. T., Teplitz, H. I., Ogle, P. M., Devost, D., Higdon, S. J. U., Marshall, J. A., & Houck, J. R. 2007, ApJ, 669, 810

Draine, B. T., Aniano, G., Krause, O., Groves, B., Sandstrom, K., Braun, R., Leroy, A., Klaas, U., Linz, H., Rix, H.-W., Schinnerer, E., Schmiedeke, A., & Walter, F. 2014, ApJ, 780, 172

Draine, B. T., Dale, D. A., Bendo, G., Gordon, K. D., Smith, J. D. T., Armus, L., Engelbracht, C. W., Helou, G., Kennicutt, R. C., J., Li, A., Roussel, H., Walter, F., Calzetti, D., Moustakas, J., Murphy, E. J., Rieke, G. H., Bot, C., Hollenbach, D. J., Sheth, K., & Teplitz, H. I. 2007, ApJ, 663, 866

Draine, B. T. & Li, A. 2007, ApJ, 657, 810

Duncan, K. J., Shivaei, I., Shapley, A. E., Reddy, N. A., Mobasher, B., Coil, A. L., Kriek, M., & Siana, B. 2020, MNRAS, 498, 3648

Elbaz, D., Dickinson, M., Hwang, H. S., Díaz-Santos, T., Magdis, G., Magnelli, B., Le Borgne, D., Galliano, F., Pannella, M., Chanial, P., Armus, L., Charmandaris, V., Daddi, E., Aussel, H., Popesso, P., Kartaltepe, J., Altieri, B., Valtchanov, I., Coia, D., Dannerbauer, H., Dasyra, K., Leiton, R., Mazzarella, J., Alexander, D. M., Buat, V., Burgarella, D., Chary, R. R., Gilli, R., Ivison, R. J., Juneau, S., Le Floc'h, E., Lutz, D., Morrison, G. E., Mullaney, J. R., Murphy, E., Pope, A., Scott, D., Brodwin, M., Calzetti, D., Cesarsky, C., Charlot, S., Dole, H., Eisenhardt, P., Ferguson, H. C., Förster Schreiber, N., Frayer, D., Giavalisco, M., Huynh, M., Koekemoer, A. M., Papovich, C., Reddy, N., Surace, C., Teplitz, H., Yun, M. S., & Wilson, G. 2011, A&A, 533, A119

Engelbracht, C. W., Gordon, K. D., Rieke, G. H., Werner, M. W., Dale, D. A., & Latter, W. B. 2005, ApJ, 628, L29

Faber, S. M., Phillips, A. C., Kibrick, R. I., Alcott, B., Allen, S. L., Burrous, J., Cantrall, T., Clarke, D., Coil, A. L., Cowley, D. J., Davis, M., Deich, W. T. S., Dietsch, K., Gilmore, D. K., Harper, C. A., Hilyard, D. F., Lewis, J. P., McVeigh, M., Newman, J., Osborne, J., Schiavon, R., Stover, R. J., Tucker, D., Wallace, V., Wei, M., Wirth, G., & Wright, C. A. in , Society of Photo-Optical Instrumentation Engineers (SPIE) Conference Series, Vol. 4841, Instrument Design and Performance for Optical/Infrared Ground-based Telescopes, ed. M. IyeA. F. M. Moorwood, 1657–1669

Fritz, J., Franceschini, A., & Hatziminaoglou, E. 2006, MNRAS, 366, 767

García-Bernete, I., Rigopoulou, D., Aalto, S., Spoon, H. W. W., Hernán-Caballero, A., Efstathiou, A., Roche, P. F., & König, S. 2022, A&A, 663, A46

Goto, T., Takagi, T., Matsuhara, H., Takeuchi, T. T., Pearson, C., Wada, T., Nakagawa, T., Ilbert, O., Le Floc'h, E., Oyabu, S., Ohyama, Y., Malkan, M., Lee, H. M., Lee, M. G., Inami, H., Hwang, N., Hanami, H., Im, M., Imai, K., Ishigaki, T., Serjeant, S., & Shim, H. 2010, A&A, 514, A6

Gürkan, G., Hardcastle, M. J., Smith, D. J. B., Best, P. N., Bourne, N., Calistro-Rivera, G., Heald, G., Jarvis, M. J., Prandoni, I., Röttgering, H. J. A., Sabater, J., Shimwell, T., Tasse, C., & Williams, W. L. 2018, MNRAS, 475, 3010

Hao, C.-N., Kennicutt, R. C., Johnson, B. D., Calzetti, D., Dale, D. A., & Moustakas, J. 2011, ApJ, 741, 124

Helou, G. & Bicay, M. D. 1993, ApJ, 415, 93

Helou, G., Soifer, B. T., & Rowan-Robinson, M. 1985, ApJ, 298, L7

Houck, J. R., Weedman, D. W., Le Floc'h, E., & Hao, L. 2007, ApJ, 671, 323

Huang, J. S., Ashby, M. L. N., Barmby, P., Brodwin, M., Brown, M. J. I., Caldwell, N., Cool, R. J., Eisenhardt, P., Eisenstein, D., Fazio, G. G., Le Floc'h, E., Green, P., Kochanek, C. S., Lu, N., Pahre, M. A., Rigopoulou, D., Rosenberg, J. L., Smith, H. A., Wang, Z., Willmer, C. N. A., & Willner, S. P. 2007, ApJ, 664, 840

Hwang, N., Lee, M. G., Lee, H. M., Im, M., Kim, T., Matsuhara, H., Wada, T., Oyabu, S., Pak, S., Chun, M.-Y., Watarai, H., Nakagawa, T., Pearson, C., Takagi, T., Hanami, H., & White, G. J. 2007, ApJS, 172, 583

Imai, K., Matsuhara, H., Oyabu, S., Wada, T., Takagi, T., Fujishiro, N., Hanami, H., & Pearson, C. P. 2007, , 133, 2418

Imanishi, M., Dudley, C. C., Maiolino, R., Maloney, P. R., Nakagawa, T., & Risaliti, G. 2007, ApJS, 171, 72

Ivison, R. J., Magnelli, B., Ibar, E., Andreani, P., Elbaz, D., Altieri, B., Amblard, A., Arumugam, V., Auld, R., Aussel, H., Babbedge, T., Berta, S., Blain, A., Bock, J., Bongiovanni, A., Boselli, A., Buat, V., Burgarella, D., Castro-Rodríguez, N., Cava, A., Cepa, J., Chanial, P., Cimatti, A., Cirasuolo, M., Clements, D. L., Conley, A., Conversi, L., Cooray, A., Daddi, E., Dominguez, H., Dowell, C. D., Dwek, E., Eales, S., Farrah, D., Förster Schreiber, N., Fox, M., Franceschini, A., Gear, W., Genzel, R., Glenn, J., Griffin, M., Gruppioni, C., Halpern, M., Hatziminaoglou, E., Isaak, K., Lagache, G., Levenson, L., Lu, N., Lutz, D., Madden, S., Maffei, B., Magdis, G., Mainetti, G., Maiolino, R., Marchetti, L., Morrison, G. E., Mortier, A. M. J., Nguyen, H. T., Nordon, R., O'Halloran, B., Oliver, S. J., Omont, A., Owen, F. N., Page, M. J., Panuzzo, P., Papageorgiou, A., Pearson, C. P., Pérez-Fournon, I., Pérez García, A. M., Poglitsch, A., Pohlen, M., Popesso, P., Pozzi, F., Rawlings, J. I., Raymond, G., Rigopoulou, D., Riguccini, L., Rizzo, D., Rodighiero, G., Roseboom, I. G., Rowan-Robinson, M., Saintonge, A., Sanchez Portal, M., Santini, P., Schulz, B., Scott, D., Seymour, N., Shao, L., Shupe, D. L., Smith, A. J., Stevens, J. A., Sturm, E., Symeonidis, M., Tacconi, L., Trichas, M., Tugwell, K. E.,

Vaccari, M., Valtchanov, I., Vieira, J., Vigroux, L., Wang, L., Ward, R., Wright, G., Xu, C. K., & Zemcov, M. 2010, A&A, 518, L31

Jarrett, T. H., Cohen, M., Masci, F., Wright, E., Stern, D., Benford, D., Blain, A., Carey, S., Cutri, R. M., Eisenhardt, P., Lonsdale, C., Mainzer, A., Marsh, K., Padgett, D., Petty, S., Ressler, M., Skrutskie, M., Stanford, S., Surace, J., Tsai, C. W., Wheelock, S., & Yan, D. L. 2011, ApJ, 735, 112

Jeon, Y., Im, M., Kang, E., Lee, H. M., & Matsuhara, H. 2014, ApJS, 214, 20

Jones, T., Martin, C., & Cooper, M. C. 2015, ApJ, 813, 126

Kennicutt, R. C., J. 1983, ApJ, 272, 54

Kennicutt, Robert C., J. 1998, ARA&A, 36, 189

Kennicutt, Robert C., J., Hao, C.-N., Calzetti, D., Moustakas, J., Dale, D. A., Bendo, G., Engelbracht, C. W., Johnson, B. D., & Lee, J. C. 2009, ApJ, 703, 1672

Kennicutt, R. C. & Evans, N. J. 2012, ARA&A, 50, 531

Kewley, L. J., Geller, M. J., & Jansen, R. A. 2004, AJ, 127, 2002

Kewley, L. J., Maier, C., Yabe, K., Ohta, K., Akiyama, M., Dopita, M. A., & Yuan, T. 2013, ApJ, 774, L10

Kim, S. J., Lee, H. M., Matsuhara, H., Wada, T., Oyabu, S., Im, M., Jeon, Y., Kang, E., Ko, J., Lee, M. G., Takagi, T., Pearson, C., White, G. J., Jeong, W. S., Serjeant, S., Nakagawa, T., Ohyama, Y., Goto, T., Takeuchi, T. T., Pollo, A., Solarz, A., & Pępiak, A. 2012, A&A, 548, A29

Kobayashi, M. A. R., Inoue, Y., & Inoue, A. K. 2013, ApJ, 763, 3

Kroupa, P. 2001, MNRAS, 322, 231

Krumpe, M., Miyaji, T., Brunner, H., Hanami, H., Ishigaki, T., Takagi, T., Markowitz, A. G., Goto, T., Malkan, M. A., Matsuhara, H., Pearson, C., Ueda, Y., & Wada, T. 2015, MNRAS, 446, 911

Lagache, G. & Dole, H. 2006, in The Fabulous Destiny of Galaxies: Bridging Past and Present, 189

Le Floc'h, E., Papovich, C., Dole, H., Bell, E. F., Lagache, G., Rieke, G. H., Egami, E., Pérez-González, P. G., Alonso-Herrero, A., Rieke, M. J., Blaylock, M., Engelbracht, C. W., Gordon, K. D., Hines, D. C., Misselt, K. A., Morrison, J. E., & Mould, J. 2005, ApJ, 632, 169

Lee, H. M., Im, M., Wada, T., Shim, H., Kim, S. J., Lee, M. G., Hwang, N., Matsuhara, H., Nakagawa, T., Oyabu, S., Pearson, C. P., Takagi, T., Onaka, T., Fujishiro, N., Hanami, H., Ishihara, D., Ita, Y., Kataza, H., Kim, W., Matusmoto, T., Murakami, H., Ohyama, Y., Sakon, I., Tanabé, T., Uemizu, K., Ueno, M., Usui, F., & Watarai, H. 2007, PASJ, 59, S529

Masters, D. & Capak, P. 2011, PASP, 123, 638

Matsuhara, H., Wada, T., Matsuura, S., Nakagawa, T., Kawada, M., Ohyama, Y., Pearson, C. P., Oyabu, S., Takagi, T., Serjeant, S., White, G. J., Hanami, H., Watarai, H., Takeuchi, T. T., Kodama, T., Arimoto, N., Okamura, S., Lee, H. M., Pak, S., Im, M. S., Lee, M. G., Kim, W., Jeong, W.-S., Imai, K., Fujishiro, N., Shirahata, M., Suzuki, T., Ihara, C., & Sakon, I. 2006, PASJ, 58, 673

Matsuhara, H., Wada, T., Oi, N., Takagi, T., Nakagawa, T., Murata, K., Goto, T., Oyabu, S., Takeuchi, T. T., Malek, K., Solarz, A., Ohyama, Y., Miyaji, T., Krumpe, M., Lee, H. M., Im, M., Serjeant, S., Pearson, C. P., White, G. J., Malkan, M. A., Hanami, H., Ishigaki, T., Burgarella, D., Buat, V., & Pollo, A. 2017, Publication of Korean Astronomical Society, 32, 213

McLean, I. S., Steidel, C. C., Epps, H. W., Konidaris, N., Matthews, K. Y., Adkins, S., Aliado, T., Brims, G., Canfield, J. M., Cromer, J. L., Fucik, J., Kulas, K., Mace, G., Magnone, K., Rodriguez, H., Rudie, G., Trainor, R., Wang, E., Weber, B., & Weiss, J. Society of Photo-Optical Instrumentation Engineers (SPIE) Conference Series, Vol. 8446, , Ground-based and Airborne Instrumentation for Astronomy IV, ed. I. S. McLeanS. K. Ramsay & H. Takami, 84460J

Miyaji, T., Krumpe, M., Brunner, H., Ishigaki, T., Hanami, H., Markowitz, A., Takagi, T., Goto, T., Malkan, M. A., Matsuhara, H., Pearson, C., Ueda, Y., & Wada, T. 2017, Publication of Korean Astronomical Society, 32, 235

Murata, K., Matsuhara, H., Wada, T., Arimatsu, K., Oi, N., Takagi, T., Oyabu, S., Goto, T., Ohyama, Y., Malkan, M., Pearson, C., Małek, K., & Solarz, A. 2013, A&A, 559, A132

Nayyeri, H., Ghotbi, N., Cooray, A., Bock, J., Clements, D. L., Im, M., Kim, M. G., Korngut, P., Lanz, A., Lee, H. M., Lee, D. H., Malkan, M., Matsuhara, H., Matsumoto, T., Matsuura, S., Nam, U. W., Pearson, C., Serjeant, S., Smidt, J., Tsumura, K., Wada, T., & Zemcov, M. 2018, ApJS, 234, 38

Ohyama, Y., Wada, T., Matsuhara, H., Takagi, T., Malkan, M., Goto, T., Egami, E., Lee, H. M., Im, M., Kim, J. H., Pearson, C., Inami, H., Oyabu, S., Usui, F., Burgarella, D., Mazyed, F., Imanishi, M., Jeong, W. S., Miyaji, T., Díaz Tello, J., Nakagawa, T., Serjeant, S., Takeuchi, T. T., Toba, Y., White, G. J., Hanami, H., & Ishigaki, T. 2018, A&A, 618, A101

Oi, N., Goto, T., Malkan, M., Pearson, C., & Matsuhara, H. 2017, PASJ, 69, 70

Oi, N., Goto, T., Matsuhara, H., Utsumi, Y., Momose, R., Toba, Y., Malkan, M., Takagi, T., Huang, T.-C., Kim, S. J., & Ohyama, Y. 2021, MNRAS, 500, 5024

Oi, N., Matsuhara, H., Murata, K., Goto, T., Wada, T., Takagi, T., Ohyama, Y., Malkan, M., Im, M., Shim, H., Serjeant, S., & Pearson, C. 2014, A&A, 566, A60

Osterbrock, D. E. 1989, Astrophysics of gaseous nebulae and active galactic nuclei

Pearson, C., Barrufet, L., Campos Varillas, M. d. C., Serjeant, S., Clements, D. L., Goto, T., Im, M., Jeong, W.-S., Kim, S. J., Matsuhara, H., Sedgwick, C., & Valtchanov, I. 2019, PASJ, 71, 13

Pearson, C., Cheale, R., Serjeant, S., Matsuhara, H., White, G. J., Burgarella, D., Valtchanov, I., Altieri, B., Clements, D. L., & Hopwood, R. 2017, Publication of Korean Astronomical Society, 32, 219

Peeters, E., Spoon, H. W. W., & Tielens, A. G. G. M. 2004, ApJ, 613, 986

Pettini, M. & Pagel, B. E. J. 2004, MNRAS, 348, L59

Rush, B., Malkan, M. A., & Edelson, R. A. 1996, ApJ, 473, 130

Salim, S., Rich, R. M., Charlot, S., Brinchmann, J., Johnson, B. D., Schiminovich, D., Seibert, M., Mallery, R., Heckman, T. M., Forster, K., Friedman, P. G., Martin, D. C., Morrissey, P., Neff, S. G., Small, T., Wyder, T. K., Bianchi, L., Donas, J., Lee, Y.-W., Madore, B. F., Milliard, B., Szalay, A. S., Welsh, B. Y., & Yi, S. K. 2007, ApJS, 173, 267

Shim, H., Im, M., Ko, J., Jeon, Y., Karouzos, M., Kim, S. J., Lee, H. M., Papovich, C., Willmer, C., & Weiner, B. J. 2013, ApJS, 207, 37

Shipley, H. V., Papovich, C., Rieke, G. H., Brown, M. J. I., & Moustakas, J. 2016, ApJ, 818, 60

Shipley, H. V., Papovich, C., Rieke, G. H., Dey, A., Jannuzi, B. T., Moustakas, J., & Weiner, B. 2013, ApJ, 769, 75

Shivaei, I., Reddy, N. A., Shapley, A. E., Siana, B., Kriek, M., Mobasher, B., Coil, A. L., Freeman, W. R., Sanders, R. L., Price, S. H., Azadi, M., & Zick, T. 2017, ApJ, 837, 157

Shogaki, A., Matsuura, S., Oi, N., Goto, T., Matsuhara, H., Murata, K., Takagi, T., Otsuka, T., Malkan, M., & Churei, S. T. Ootsubo, I. YamamuraK. Murata & T. Onaka, 367–370

Smith, J. D. & Draine, B. 2012, PAHFIT: Properties of PAH Emission, Astrophysics Source Code Library, record ascl:1210.009

Smith, J. D. T., Draine, B. T., Dale, D. A., Moustakas, J., Kennicutt, R. C., J., Helou, G., Armus, L., Roussel, H., Sheth, K., Bendo, G. J., Buckalew, B. A., Calzetti, D., Engelbracht, C. W., Gordon, K. D., Hollenbach, D. J., Li, A., Malhotra, S., Murphy, E. J., & Walter, F. 2007, ApJ, 656, 770

Spoon, H. W. W., Marshall, J. A., Houck, J. R., Elitzur, M., Hao, L., Armus, L., Brandl, B. R., & Charmandaris, V. 2007, ApJ, 654, L49

Stecker, F. W., Scully, S. T., & Malkan, M. A. 2016, ApJ, 827, 6

Takagi, T., Arimoto, N., & Hanami, H. 2003, MNRAS, 340, 813

Takagi, T., Ohyama, Y., Goto, T., Matsuhara, H., Oyabu, S., Wada, T., Pearson, C. P., Lee, H. M., Im, M., Lee, M. G., Shim, H., Hanami, H., Ishigaki, T., Imai, K., White, G. J., Serjeant, S., & Malkan, M. 2010, A&A, 514, A5

Takeuchi, T. T., Buat, V., & Burgarella, D. Deepest Astronomical Surveys, ed. , J. AfonsoH. C. FergusonB. Mobasher & R. Norris, 559

Wada, T., Matsuhara, H., Oyabu, S., Takagi, T., Lee, H. M., Im, M., Ohyama, Y., Goto, T., Pearson, C. P., White, G. J., Serjeant, S., Wada, K., & Hanami, H. 2008, , 60, S517

Wright, E. L., Eisenhardt, P. R. M., Mainzer, A. K., Ressler, M. E., Cutri, R. M., Jarrett, T., Kirkpatrick, J. D., Padgett, D., McMillan, R. S., Skrutskie, M., Stanford, S. A., Cohen, M., Walker, R. G., Mather, J. C., Leisawitz, D., Gautier, Thomas N., I., McLean, I., Benford, D., Lonsdale, C. J., Blain, A., Mendez, B., Irace, W. R., Duval, V., Liu, F., Royer, D., Heinrichsen, I., Howard, J., Shannon, M., Kendall, M., Walsh, A. L., Larsen,

M., Cardon, J. G., Schick, S., Schwalm, M., Abid, M., Fabinsky, B., Naes, L., & Tsai, C.-W. 2010, AJ, 140, 1868

Yan, L., Chary, R., Armus, L., Teplitz, H., Helou, G., Frayer, D., Fadda, D., Surace, J., & Choi, P. 2005, ApJ, 628, 604